January 2019

Colloidal Dynamics Within Polymer Solutions And Complex Fluids

Namita Shokeen
Wayne State University

COLLOIDAL DYNAMICS WITHIN POLYMER SOLUTIONS AND COMPLEX FLUIDS

by

NAMITA SHOKEEN

DISSERTATION

Submitted to the Graduate School

of Wayne State University,

Detroit, Michigan

in partial fulfillment of the requirements

for the degree of

DOCTOR OF PHILOSOPHY

2019

MAJOR: PHYSICS

Approved By:

_____

Advisor Date

_____

_____

_____

_____

DEDICATION

This thesis is dedicated to my respected parents (Mahavir Shokeen and Prem Lata), loving husband (Mohit Kumar), elder brother (Lalit Shokeen) and younger sister (Ekta Shokeen) for their love and support always.

ACKNOWLEDGEMENTS

I would like to take this opportunity to thank my PhD advisor Dr. Ashis Mukhopadhyay, who has guided me throughout my doctoral research. He has been very kind, helpful, encouraging and supportive always. He has always been there to provide guidance related to experimental challenges and/or theoretical concepts needed to improve my research skills and performance. I am extremely thankful for his valuable and endless advice and help in the preparation of the manuscripts and dissertation. I sincerely appreciate him for his time investment in not only my research but also in improving my candidacy and skills needed for my future career goals. I am so grateful to him for providing me the opportunity to work with him. I am extremely thankful to my candidacy committee Dr. Takeshi Sakamoto, Dr. Zhixian Zhou and Dr. Federico A. Rabuffetti for their time and continual support in completion of my dissertation research.

I wish to thank Zoe and Dr. Christopher Kelly (Physics Department, Wayne State University); Dr. Elaine Zhu and Ben (Chemical engineering Department, Wayne State University) and Prof. Michael Solomons (Chemical engineering department, University of Michigan) for providing access to their optical microscopy set ups. I would like to extend my sincere thanks to my senior lab colleague Sharmine Alam for initially training me on the research instruments and other fellow lab mates: Kavindya Senanayake and Christopher Issa for their assistance and interactions during my doctoral research.

I acknowledge the support from the department of Physics and Astronomy, Wayne State University for offering me graduate assistantships and Frank Endowed Knoller fellowship

during my PhD. I am also thankful to Richard Barber Interdisciplinary Research program for funding my research in the summer of 2019.

TABLE OF CONTENTS

LIST OF FIGURES

LIST OF TABLES

CHAPTER 1

INTRODUCTION

1.1 SOFT MATTER

Soft matter is a sub-field of condensed matter and covers a broad range of classical systems which are neither perfectly crystalline nor simple liquids. Soft matter is present almost everywhere around us. For example, soaps, rubber, paints, glues, and even many food items contain soft materials such as proteins, polysaccharides, nucleic acids etc. Soft matter is a very broad, interdisciplinary, and highly active research area for physicists, biologists, chemists, engineers, mathematicians and material scientists. It is a progressive field with main research focus on study of colloids, polymers, liquid crystals, foams, emulsions, membranes, vesicles, droplets, self-assembly, surfaces and interfaces, packing, geometry and topology, fractures and failures, active and driven matter, dynamics of structured and complex fluids, soft biological systems, etc. Such materials exhibit distinct macroscopic and physical appearances with unique

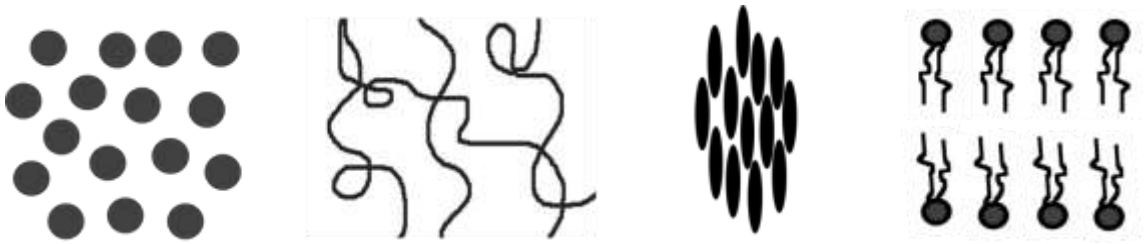

FIGURE 1.1.1 Soft materials: colloids (10 nm- 10 μm), polymers (10 nm- 10 μm), liquid crystals and amphiphiles/surfactants

properties. The length scales of soft materials are mesoscopic i.e. lies between atomic (> 0.1 nm) and macroscopic (< 10 μm) scales. This makes soft materials susceptible to large fluctuations caused by Brownian motion. Soft matter in aqueous media is bombarded by the molecules of

solvent and is constantly turning and wriggling due to thermal fluctuations. Such random motion of soft materials leads to their unique properties.

Soft materials show striking rheological properties. Most of the soft materials show viscoelastic behavior, which is a time-dependent response to the applied stress. They are both viscous and elastic at different time scales. Solids and liquids show distinct mechanical response to the applied shear stress. When a shear is applied, solids resist deformations whereas fluids tend to flow. Silly Putty is a good example that exhibits both kinds of mechanical responses. The characteristic viscoelastic time scales are material dependent. A fluid can be classified into Newtonian or non-Newtonian depending on its strain rate response with applied stress. The

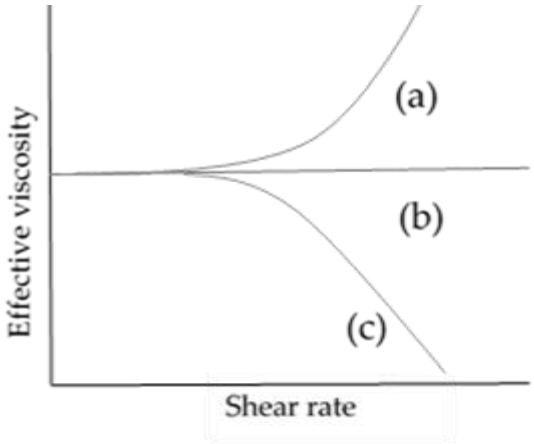

strain rate is constant in the Newtonian fluids when a constant stress is applied. So, the relation between the shear stress and shear rate is linear and we can find the constant of proportionality, which is defined as the viscosity. However, in non-Newtonian fluids, the viscosity is dependent on the shear rate, which is not constant and can be time-dependent too. Shear thinning or shear thickening[1] is visible in many non-Newtonian polymer solutions. In shear thinning, the fluid flow increases with the increase in the shear rate but this is opposite in the case of shear thickening fluids as shown in the figure 1.1.2 above.

FIGURE 1.1.2 Schematic representation of non-linear response of viscosity to an applied strain rate. (a) shear thickening, (b) Newtonian fluid and (c) shear thinning

Among many other amazing properties of soft materials, their ability to self-assemble is unique. Minimization of free energy is the driving force behind self-assembly. Systems including surfactants, block copolymers, amphiphiles, proteins, actin filaments, microtubules, cells, and dense solutions of aqueous nanoparticles tend to naturally form highly ordered structures when immersed in aqueous media. My research is mainly focused on colloidal dynamics within polymer solutions and complex fluids. A few topics related to this field will be briefly discussed further.

1.2 COLLOIDAL DISPERSIONS

Colloidal dispersions are formed when colloids (mainly solid-like particles in nanometer to micrometer size range (~1 nm- 10 um) are evenly dispersed inside a continuous media. The dispersing media as well as particles can be in solid, liquid or gaseous form.

The stability of a colloidal dispersion is very important to provide correct information about their physical properties and motion. A stable colloidal dispersion is marked by evenly dispersing colloidal particles inside a surrounding fluid as shown in figure 1.2.1 (a). There are many problems that arise in colloidal solutions i.e. polydispersity, aggregation/agglomeration, sedimentation etc. Dispersed colloids experience electrostatic van der Waals attraction and repulsion due to screening of charges. Gravitational force leads to sedimentation in colloidal dispersions while electrostatic forces can be accounted for other problems. Sedimentation can be mostly hindered by using density matching approach in a narrow range of materials. In this

method, the mass density of dispersed particles is matched with that of the dispersing media.

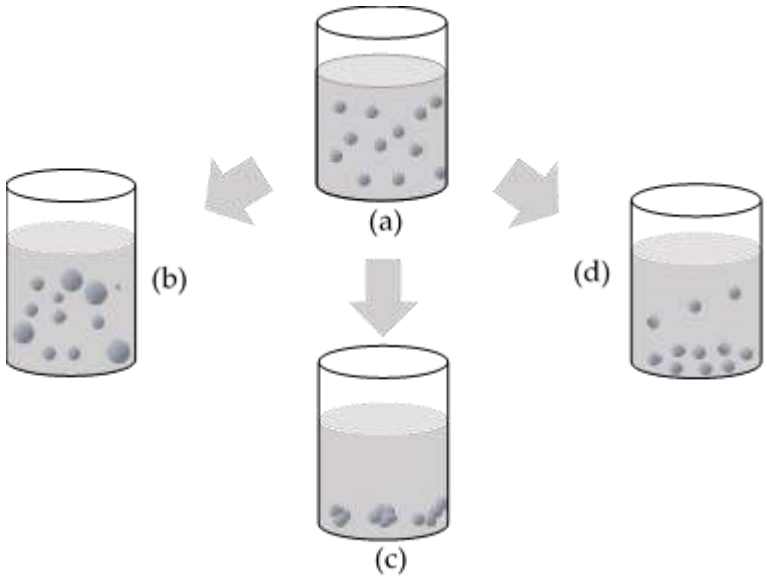

FIGURE 1.2.1 Colloidal dispersions with associated problems within a colloidal dispersion: (a) stable colloidal dispersion (b) polydispersity, (c) aggregation/agglomeration and (d)sedimentation

Aggregation of the particles inside the colloidal dispersion is one of the main factors that affects stability of colloids. It can be seen in figure 1.2.1(b), the particles can come close to each other and stick together to form aggregates inside a colloidal dispersion. To avoid this problem, we can use

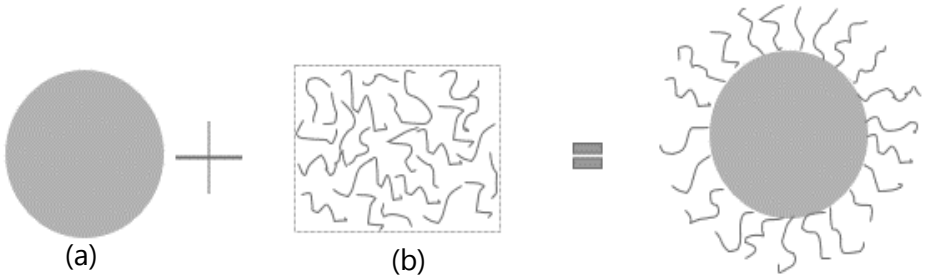

FIGURE 1.2.2 Stabilization of particles (a) using polymer (b) coating on their surface

methods that can keep these particles away from each other to a large extent. The most common way to tackle this problem is to generate a repulsive force between the particles. This can be done by exploiting the usual electrostatic force, either by a method known as charge stabilization or by

coating the particles with some polymers known as steric stabilization[1]. In the latter method, the particles are stabilized using polymer chain coatings on the surface of particles (figure 1.2.2) so that when the two particles come closer, they will feel the repulsive force created by the osmotic pressure as a resulting effect of increased polymer concentration inside the gap. Many ordered and disordered structures can also be formed inside colloidal suspensions as a consequence of interparticle interactions[2] and thermal motion.

1.3 POLYMERS AND POLYMER SOLUTIONS

Polymers are very large chain-like molecules, which are made up of many repeated units (also called monomers) of one kind (homopolymers), different (copolymers as shown in figure 1.3.1)

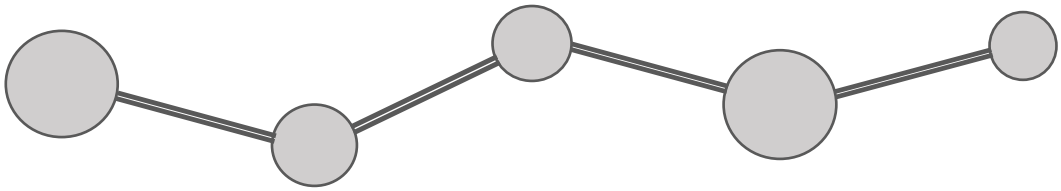

FIGURE 1.3.1: Representation of a chain polymer with different kind of monomers

or random (random polymers). They can be natural as well as synthetic, such as polyethylene, polystyrene, and nylon. They can be found in various physical states like liquids, crystalline (solid/liquid), and glasses. Polymers are also available in a large variety of molecular weights. Polymer chains can be linear or branched. The length of the polymer chains depends on the degree of polymerization, N, i.e., the number of repeated units. The degree of polymerization is directly proportional to the relative molecular mass, M of the chain as shown in the equation below:

$$M = N M_{mono} \qquad 1.1$$

where, M_{mono} is the molar mass of the monomer/ repeated unit.

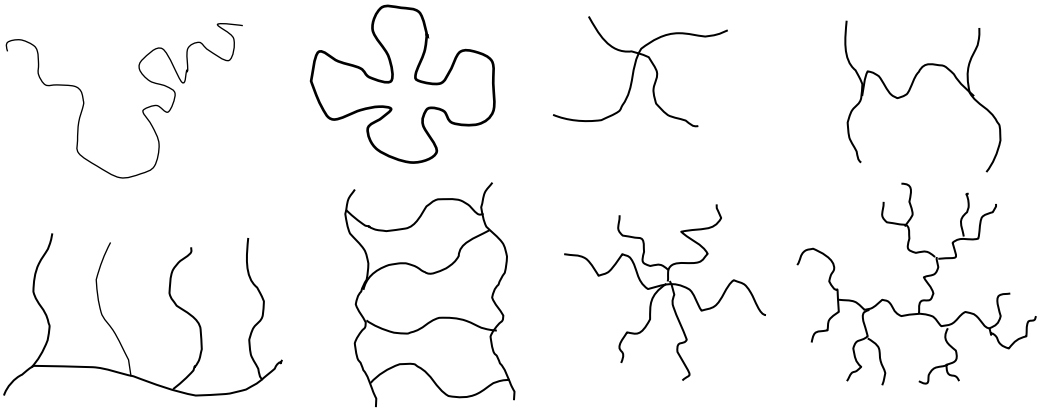

FIGURE 1.3.2: Different architectures of polymers: linear, ring, star-branched, H-branched, comb, ladder, dendrimer, and randomly-branched.

The monomers inside polymer chains are attached by covalent bonding. The strength of the bonding between monomers should be larger than the value of thermal energy K_bT to stay connected to each other. The ways in which monomers organize themselves inside a polymer chain plays a very important role in their chemical and physical properties. Different kinds of polymer architecture are possible depending upon the shapes of polymer chains as shown in figure 1.3.2. Polymer microstructures can be broadly classified into homopolymers and heteropolymers depending on having one kind of monomers or different in their chains, respectively. Heteropolymers can be further classified into different sub classes i.e. random copolymers, alternating copolymers, block copolymers, and graft copolymers depending on the different arrangements of monomers in the polymer chains as shown in the figure 1.3.3. An important length scale in determining the size of polymers is radius of gyration R_g that can be defined as the mean squared distance of every point on an object from the center of gravity of the object.

FIGURE 1.3.3: Different kinds of copolymers: (a) alternating copolymer, (b) random copolymer, (c) block copolymer and (d) graft copolymer

Polymer solutions are formed by dissolving polymers in the solvents and they can be divided into three categories, i.e., dilute, semi-dilute, and concentrated depending on the polymer concentration inside the solution. Polymer concentration is usually defined in terms of volume fraction ϕ, which is defined as the volume of polymer to the volume of the total solution. The polymer concentration at which polymer chains begin to overlap[3] due to their increased

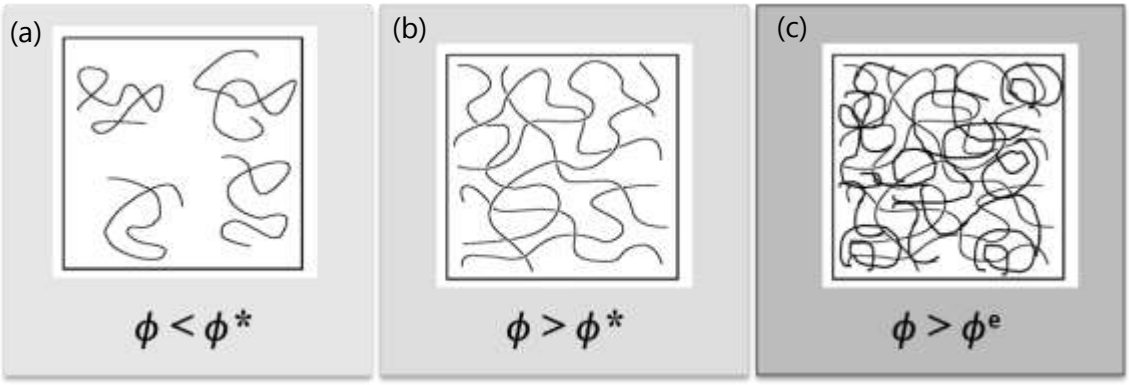

FIGURE 1.3.4: Different concentration regimes for polymer solutions: (a) dilute, (b) semi-dilute, (c) concentrated and (d) polymer melt.

concentration is called as the overlap volume fraction ϕ^*. Thus, ϕ^* is used as a measure to distinguish between the dilute and semi-dilute solutions as shown in the figure 1.3.4. If polymer concentration is lower than the overlap volume fraction, the solution is called dilute[4] where the

polymer chains do not interact as they are significantly far from each other. If the polymer

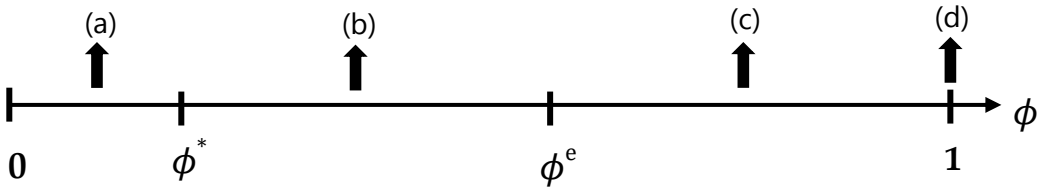

FIGURE 1.3.5: Pictorial representation of polymer chains in different polymeric solutions: (a) dilute, (b) semi-dilute and (c) concentrated.

concentration is increased to reach above the overlap volume fraction, the solution is said to be in semi-dilute regime where the polymer chains begin to interact with each other via overlapping. Below polymer melt concentration i.e. 1, entanglement volume fraction ϕ^e marks the polymer concentration where most of the polymer chains are overlapped and entangled with each other as shown in the above figure 1.3.4 and 1.3.5. Polymer solutions with polymer concentration higher than ϕ^e are called as concentrated solutions. One of my research's main focuses is the study of motion of colloids inside polymer matrices and the following discussion provides a brief introduction for the same.

1.4 DYNAMICS OF COLLOIDAL PARTICLES WITHIN POLYMER SOLUTIONS

To observe and quantify the dynamics of nano and micron sized particles inside polymer solutions, there are certain time scales that are important to study at which the polymers change their behavior. Figure 1.4.1 shows a cartoon of a spherical colloids dispersed within a polymer solution. Relaxation time τ, is a measure of the time scale at which molecules inside a polymer rearrange themselves, resulting in the separation of solid and liquid-like behavior. It is the crossover time scale before which the viscoelastic polymer behaves like a solid when stress is applied, whereas in the opposite limit, polymers behave like a liquid at longer time scales.

The diffusive motion of colloids inside various solutions can be quantified in terms of their diffusion coefficients. Fick's second law, derived from the continuity equation of mass, provides the simplest description of diffusion through a fundamental relation between the rate of change of particle concentration and the spatial second derivative of particle concentration that

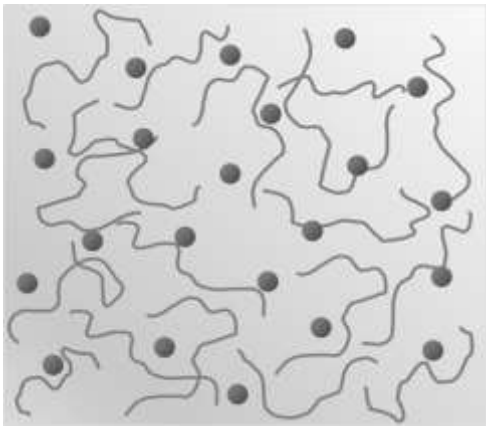

FIGURE 1.4.1: Colloids dispersed in aqueous polymer solutions.

eventually makes it simpler to quantify the connection between the time and square of the distance over which the Brownian diffusion occurs in terms of the particles' self-diffusion coefficient D. Diffusion law can be written as:

$$\frac{\partial c(x,t)}{\partial t} = D\frac{\partial^2 c(x,t)}{\partial x^2} \qquad 1.2$$

Given an initial condition, $c(x, t = 0)$, we can solve this diffusion equation and get $c(x, t)$ at all times. If started with a delta function, using Green's function, the solution is gaussian:

$$c(x,t) = \frac{N}{\sqrt{4\pi Dt}} \mathrm{e}^{-\frac{x^2}{4Dt}} \qquad 1.3$$

where, $\int_{-\infty}^{\infty} c(x,t)dx = N$

A probability density function $P(x, t)$ for normal Brownian diffusion can be defined as

$$P(x,t) = c(x,t)/N \tag{1.4}$$

$$P(x,t) = \frac{1}{\sqrt{4\pi Dt}} \mathrm{e}^{-\frac{x^2}{4Dt}} \tag{1.5}$$

Generally, Gaussian diffusion approximation is not valid in complex fluids[5]. Einstein suggested that the mean square displacements $< x^2 >$ of macromolecules moving in a d-dimensional Brownian motion over time Δt are suitably measurable and relatable to their diffusion coefficients D in the following manner:

$$< x^2 > = 2dD\Delta t \tag{1.6}$$

In simple fluids, continuum fluid model is highly accurate on the length scales that are much larger than the inter-atomic distances. Stokes-Einstein (SE) relation is used to determine the diffusion of particles that are much larger than the size of solvent molecules. It relates the translational diffusion coefficient D_T of spherical particles with hydrodynamic radii R diffusing in a solvent of viscosity η in the following way:

$$D_T = \frac{k_B T}{6\pi\eta R} \tag{1.7}$$

where, k_B is the Boltzmann constant and T is the absolute temperature. The relation that gives the rotational diffusion coefficient D_R of a spherical particle is Einstein–Smouchowski relation given by:

$$D_R = \frac{k_B T}{8\pi\eta R^3} \tag{1.8}$$

where, $(8\pi\eta R^3)$ gives the value of frictional drag coefficient for a sphere in bulk.

SE equation works very well for dilute systems with a constant solvent's viscosity. But in highly crowded polymer solutions, new complexities are added in terms of viscosity experienced

by the probe particles. Among other possible complexities, viscosity of the solvent can be shear dependent (figure 1.4.2) resulting in colloidal particles experiencing a much smaller viscosity

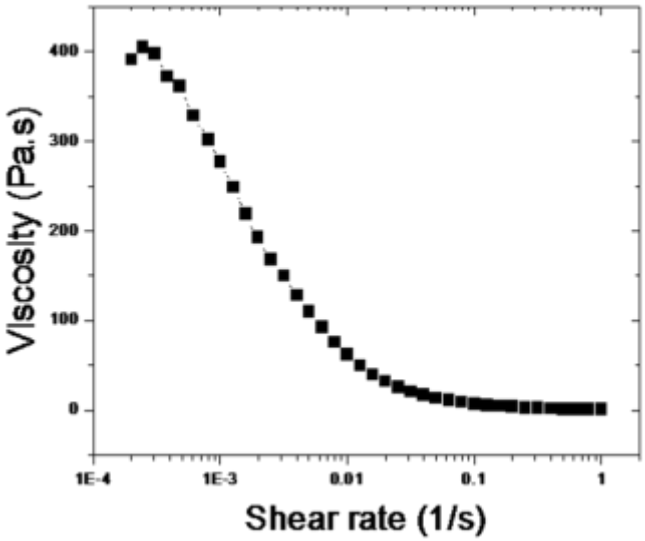

FIGURE 1.4.2: Shear thinning behavior for Poly Acrylic Acid at a polymer concentration of 0.125% extracted from rheology measurements.

called as nanoviscosity than the bulk viscosity. The validity of Stokes-Einstein equation completely breaks down in equivalent complex solutions[6]. It is difficult to determine the exact nanoviscosity. Here, another branch of physics i.e. rheology comes into picture that involves the flow studies of materials under stress[7] provides a range of shear viscosities corresponding to different strain rates . Microrheology[8] is a modern way of doing rheology by using a micron sized particle as a tracer probe for measuring viscosity.

In reciprocal space, it is possible to extract the dynamical information of a system at a wide range of length scales corresponding to the scattering wave vectors q. The relaxation time $\tau(q)$ scales as q^{-2} in dilute systems consisting of freely diffusing particles. On the other hand, for crowded particles, few characteristic peaks appear in relaxation time vs. wave vector curves. These peaks indicate long relaxation times meaning that the dynamics gets slower because of an

obstructed motion at certain length scales. This slowing down of colloidal dynamics can be readily explained with a physical phenomenon explained by de Gennes called as de Gennes narrowing[9]. A schematic representation of the underlying physics of de Gennes narrowing[10] (DGN) in a hard sphere system consisting of two spheres separated by a distance r is given by

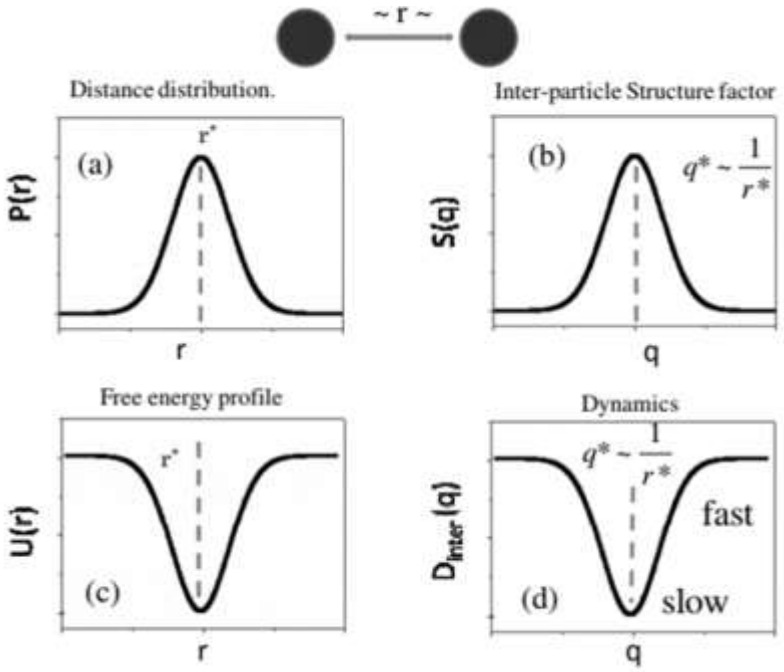

FIGURE 1.4.3: Structure and dynamics of a two hard sphere system (Reprinted with permission from Physical review letters 112(15), 158102. Copyright (2014)).

Hong and co-authors[10] (figure 1.4.3). When the spheres move relative to each other, then a distance distribution $P(r)$ has a peak at some distance r^* and the corresponding free energy curve has a minimum value at the same distance. In the reciprocal space, inter-particle structure factor distribution $S(q)$ can be defined that has a peak at $q^* \sim \frac{1}{r^*}$ and $D_{inter}(q)$ that provides the dynamical information in terms of interparticle fluctuation rate at real distances $r \sim \frac{1}{q}$ with a minimum at $q^* \sim \frac{1}{r^*}$ matching with $S(q)$. This inverse dependence on $S(q)$ indicates the slowing

down of system dynamics at a specific length scale as a consequence of slowly moving domains in a few favored arrangements in space.

1.5 COLLOIDAL STRUCTURES ON A CURVED SURFACE

In contrast to flat surfaces, packing of colloids on a curve is more complicated. There are simple ways to pack colloids on a flat surface, for example, hexagons can be packed in a honey-comb structure without any geometrical defect on a plane whereas it is not possible in the case of packing on curved spaces due to frustrations caused by curved geometry. The best example of this would be the packing of panels on a soccer ball that requires twelve pentagons in addition to

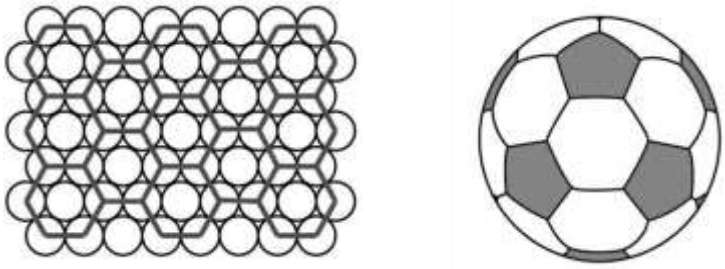

FIGURE 1.5.1: Left: Spherical colloids assembled on a flat surface in a perfect hexagonal pattern. Right: Panels on a soccer ball representing packing on a curved surface (adapted: Wikipedia)

twenty hexagons. These pentagons can be called as the defects. Such packing in its simplest form can be experimentally realized by colloidal assembly on the droplets formed on water-oil interface[11]. In a perfect hexagonal crystalline packing, every particle has exactly six nearest neighboring particles inside the colloidal assembly (figure 1.5.1:left). This is impossible to fabricate on curved surfaces. Usually the crystal structures are with five-fold, or seven-fold defects depending on the number of nearest neighbor particles per particle inside the whole structure (figure 1.5.1:right). Topology requires the crystals to have minimum number of lattice defects inside a crystal formed on a curved surface[12]. Due to the stress imposed by the curvature,

crystal structures have a natural tendency to spontaneously develop more defects[13-17]. Therefore, the mechanism of crystallization on a curve is a still unclear.

1.6 PHASE TRANSITIONS IN COLLOIDAL ASSEMBLIES

When a substance or a system undergoes phase change from a solid, liquid or a gaseous phase to a different phase at a specific temperature and pressure, it is said to be phase transitioned. Phase transitions can be classified into first order and second order as predicted by Ehrenfest. First derivatives of free energy are discontinuous at the phase transition of first order but continuous at second. Inside a solid crystallic phase, there are ordered structures with repetitive patterns. When the phase is changed from solid to liquid, loss of repetitive patterns and ordering takes place in the molecules of a substance. This phase has a higher energy and entropy than the solid phase. Consequently, in gaseous phase, the molecules move freely by spreading over in space with a much higher entropy and any patterning or ordering among each other completely disappears. The ordering can be short or long ranged and a few order parameters can be defined to quantify the local or global translational and orientational distribution. An order parameter is usually defined in such a way that it will have its maximum value in solid phase and zero in liquid phase.

One of our main research interests lies in the understanding of phase transitions of ordered structures formed on top of curved spaces which is very hard to realize experimentally at atomic scales because of the limitations imposed by currently available optics. Therefore, we use colloidal systems that are presently the most suitable systems to carry out such experimental investigations. During phase transitions in colloidal systems, different phases can be identified

based on the ordering and packing of particles. First order phase transitions are easier to be experimentally identified from direct visualization using optical microscopy and analyzed by determining certain structural correlations functions/orientational order parameters. Melting of a crystal is a classic example of first order transition. When the temperature is changed, the phase of a crystal changes. There is an enormous amount of experimental research going on to observe the two dimensional phase transitions of colloidal assemblies on both flat as well as curved surfaces[13,18-27]. In present, among all phase transitional studies, 2D freezing is the best understood so far. There have been significant advances in methods in which colloidal assemblies within a solution can be controlled. This has increased the scope of synthesizing complex yet intereseting new configurations of highly controlled soft materials. Defects are very common in natural assembling of micron sized colloids and as a result, generally low quality crystals are formed. Therefore, it becomes necessary to direct the assemblies[28] using an external force via an electric field, magnetic traps or temperature gradients. The quality of crystals can be increased by minimizing the crystal defects in a few ways including annealing them near their melting points or by using optical tweezers.

1.7 INSIGHT TO RESEARCH WITH SIGNIFICANCE

This thesis can be broadly divided into three main investigations under colloidal dynamics. The motivation behind these research projects will be discussed along with a brief introduction to them one by one.

In the first part of the thesis, we study nanoparticle dynamics within crowded media which is very important since a cell is mainly composed of macromolecules making itself a very crowded media. We determined the ensemble averaged diffusion coefficients of fluorescent

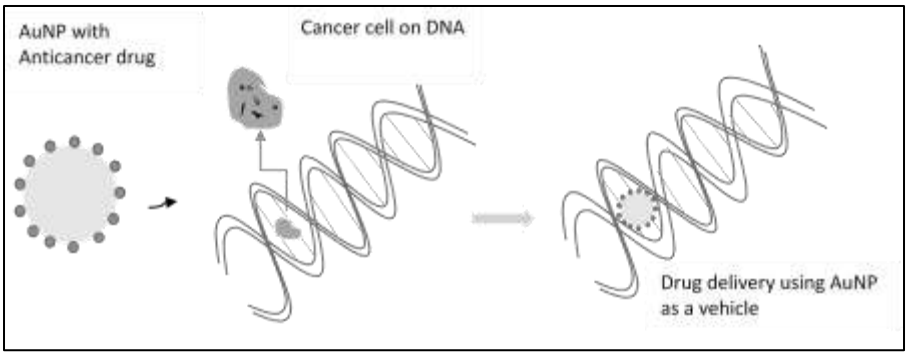

FIGURE 1.7.1: Drug delivery using AuNP inside the DNA to treat cancer (adapted: Wikipedia)

nanoparticles within concentrated polymer solutions of polyethylene oxide (PEO) and compared using two different experimental methods as discussed in chapter 4. As nanoparticles can be used as drug delivery carriers (figure 1.7.1), their motion inside a crowded environment like inside a cell becomes very useful to investigate. We mimic a similar media for nanoparticles with the use

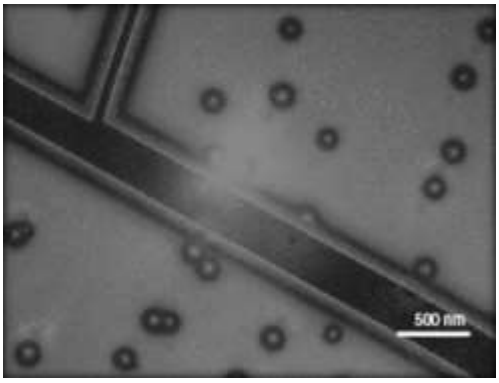

FIGURE 1.7.2: Self-healing property of nanoparticles inside materials' cracks. (Reprinted with permission from Nature Materials 5(3), 1476-4660. Copyright (2004)).

of highly concentrated polymer solutions of high molecular weights. Studies of nanoparticle dynamics is also useful in solving current existing problems in the synthesis of high performing polymeric nanomaterials[29,30] and chromatography[31]. Nanoparticles also possess a unique ability

to enhance the lifetime of materials by migrating towards the cracks[32] as shown in the figure 1.7.2. This striking property of nanoparticles including many other makes this research field very interesting to explore.

Second part of the thesis in chapter 5 contains the studies of dynamics and melting of two-dimensional self-assembled structures formed by microdiscoids dispersed in a complex fluid (critical solution of a binary mixture composed of 2,6 lutidine and water). 2D melting of the

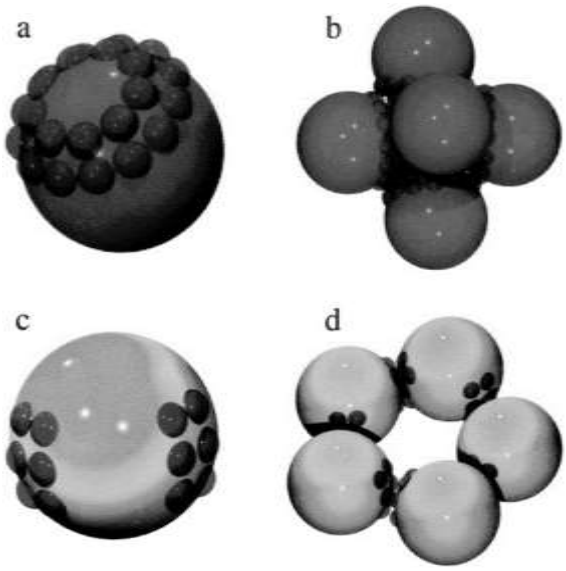

FIGURE 1.7.3: Self assemblies of anisotropic particles predicted by computer simulations: (a) spherical particles with two rings of sticky "patches", (b) square pyramid structure, (c) spherical particle with sticky "patches" that interact attractively with like patches on other particles and (d) ring assembly on cooling from five particles. (Reprinted with permission from AIChE 50(12), 2978-2985. Copyright (2004)).

colloidal ordered structures formed on top of the different sized water-lutidine droplets is also observed. We also calculated a few structural correlation functions and orientational order parameter to analyze the structural arrangements during the phase transition. The results are compared with one of the present theories of melting in 2D. Study of the dynamics of assemblies formed by colloids is very useful for new materials. Colloidal assembly can also be used for creating soft acoustic material arrays[33]. Many nanostructured materials are formed using colloids

crystals as templates[34] for use as advanced catalysts and in photonic crystals, etc. Various physical, chemical, mechanical and structural functionalities can be incorporated in colloidal surfaces and/or volumes to form desirable inexpensive materials, electronics[35] and ordered porous structures[34]. These studies are also applicable to the areas that sought materials' time-dependent response e.g. in transduction[36] and sensing applications[37]. Molecular systems in which certain desired structures (figure 1.7.3) can be regulated by generating a dynamic control over assembled material arrays are known as reconfigurable colloidal assemblies[38-40]. Recently, reconfigurable colloidal assembly has gained a huge interest as a field useful for many fields including synthesis of metamaterials and biosensors[38,41-45]. The dynamics of colloids is much slower than atoms or small molecules because of their larger sizes. Slow kinetics and low number of ordered structures with multi-fold defects in colloidal assemblies presently are a few among the current and future challenges in this field. For minimizing such research problems, it is very important to understand the underlying physics at each stage of the transitional process.

Finally, we focused on the diffusion of anisotropic colloids as anisotropy in biological systems like DNA and virus is very common. We have studied translational and rotational diffusion of microellipsoids using a quick and efficient experimental method in chapter 6. Most of the macromolecules are anisotropic in shape and their translational and rotational diffusion have a dependence on their shapes and they have various applications in technological and manufacturing fields inside high performance polymer composites[46,47] and devices.. Therefore, it advantageous to study the dynamics of Therefore, it advantageous to study the dynamics of anisotropic colloids (discoids and ellipsoids) in various media.

An overview of the dissertation is as follows. Relevant background information to the scope of our research is provided in chapter 2. Chapter 3 describes the two main methods i.e. fluorescence correlation spectrocopy and differential dynamic microscopy used for experimental investigations and data analysis. As outlined above, chapters 4 to 6 include the main projects of my research. Overall conclusions and future work will be followed. There are a few additioned projects that I've worked on are briefly presented with the preliminary results in appendixes A-C. They include synthesis of gold nanoparticles, effect of external flow on rotational diffusion of gold nanorods and colloidal dynamics within polyvinyl alcohol and xanthan solutions.

CHAPTER 2

BACKGROUND

2.1 DIFFUSION OF NANOPARTICLES WITHIN HIGHLY CONCENTRATED POLYMER SOLUTIONS

Experimental investigations of nanoparticle diffusion within complex media such as concentrated polymer solutions and polymer melts provide a better foundation and understanding of various interdisciplinary fields including soft matter physics and nanotechnology for microrheology[48] for designing and developing nanocomposites[49]. There are various scaling theories[50-52] available today for predicting the dynamics of probe particles inside polymer, biopolymer and other complex solutions. Several research groups have been working to validate these underlying theories of diffusion in different complex situations[53-56]. Various theoretical, experimental and computational studies relevant to our research are discussed in the following sections 2.1.1-2.1.3. Further discussion related with this section along with results and conclusions will be made in chapter 4.

2.1.1 PREVIOUS THEORETICAL WORK

For spherical probe particles probe diffusion can be classified into two groups[57]. Hydrodynamic theories[58] form the first group that takes the interactions between particles and polymers into account while the other group are scaling theories that accounts for motilities of particles by considering the polymers as a porous media[50,59,60] based on an effect called as "obstruction effect".

According to hydrodynamic theory, the relaxation of polymers is not taken in account and the diffusion coefficient of probes (particles) inside polymer matrix is considered to be following a stretched exponential relation with polymer concentrations. In the dilute concentration regime of polymer solutions, the polymer chains behave like hard spheres with size equal to their hydrodynamic radii. Here, the size of diffusing probes $2R_0$ is greater than the effective polymer chain size $2R_g$ (R_g: radius of gyration) and they experience hydrodynamic interactions as resulted by polymer chains. Whereas in the semi dilute polymer solutions, the diffusing probes i.e. nanoparticles experience screened hydrodynamic drag at a scale of correlation length[58] ξ as polymer chains are modeled as the fixed frictional centers of monomers. In contrast, the diffusion coefficient of probe particles have a linear relationship with relatively larger pores formed by polymers chains. The effective pore size can be obtained from a distribution of distances randomly chosen point to nearest polymer chains and they can possess different sizes based upon their random and flexible coiled conformations. The probes can not usually move inside such pores in concentrated polymer solutions and thus they feel caged or obstructed in their motion. But if the probes are larger than the obstacle sizes characterized by ξ, the motion is not completely obstructed.

According to Brochard and de Gennes's scaling theory[61], concentrated polymer solutions are considered as a short-lived polymer mesh with network size equal to the correlation length. According to their hypothesis, the viscosity experienced by probe particles within the mesh formed by polymer chains follows a scaling relation. Depending on the correlation length as compared to the probe size, the viscosity experienced by the particles differ. If $2R_0$ is much greater than ξ, the probes should experience a net full solution viscosity or macroviscosity while in the

contrasting limit, the probes should only feel solvent's viscosity. We have a few more scaling theories of particles' motility in different polymer solutions depending on their size and concentration regimes[52,58,61,62].

Phillies *et. al.* proposed a scaling model for the dynamics of rigid probes that relates the diffusion coefficient, D of probe particles to polymer concentrations as given by stretched exponential equation below[52]:

$$\frac{D}{D_0} = e^{-\beta\phi^{\gamma}} \qquad 2.1$$

where , D_0 is the diffusion coefficient of pure solvent with β and γ as scaling parameters. Phillies generalized this scaling for a whole range of polymers with different molecular weights as well. This stretched exponential seemed to worked very well experimentally meaning that there is no significant difference in diffusion when concentration is changed from dilute to semi-dilute as opposed to the expectation from scaling models for self diffusion of polymers.

Cai *et. al.* further extended the scaling theory given by Wyart and de Gennes for particle motion inside polymer melts[57]. Their theory predicted that the particles' motility within such highly concentrated polymer liquids depends on two important length scales i.e. correlation length ξ and the tube diameter a. Correlation length has the following dependence on polymer concentration:

$$\xi(\phi) = \mathrm{b}\phi^{-\nu/(3\nu-1)} \qquad 2.2$$

where, b is Kuhn's monomer length and ν is called as Flory exponent whose value varies on the solvent's type. For athermal solvent where polymer chains may be swollen, correlation length varies as

$$\xi \sim \phi^{-0.76} \tag{2.3}$$

with ν = 0.588 while in the case of a theta solvent where polymer coils act as ideal chains with exact random walks.

$$\xi \sim \phi^{-1} \tag{2.4}$$

with ν = 0.5.

Also, the tube diameter $a(\phi)$ for a good solvent in the concentrated entangled polymer solutions is given by:

$$a(\phi) \approx a(1)\phi^{-\frac{\nu}{3\nu-1}} \sim \phi^{-0.76} \sim \xi \tag{2.5}$$

where a(1) is the tube diameter in the polymer melt with a value ~ 5 nm. And in the case of a theta solvent,

$$a(\phi) \approx a(1)\phi^{-2/3} \tag{2.6}$$

The particles can be divided into three size ranges depending on the values of correlation length and tube diameter i.e. small ($2R_0 < \xi$) , intermediate ($\xi < 2R_0 < a$) and large ($2R_0 > a$). The particles' motility and diffusive nature is different for these three size ranges as explained below:

(a) For small particle size range ($2R_0 < \xi$): The motion of particles doesn't seem to get much affected by the polymer dynamics. It seems similar as the motion of particles inside a pure solvent of viscosity η_s. Hence, the diffusion of such particles is given by:

$$D \sim \frac{k_B T}{2R_0 \eta_s} \quad (2.7)$$

$$D \alpha \frac{1}{\eta_s} \quad (2.8)$$

where, k_B and T are the Boltzmann's constant and temperature.

(b) For intermediate particle size range ($\xi < 2R_0 < a$): The particles' motion in such size range doesn't remain as inside a pure solvent but it is rather affected by the segmental dynamics of polymer chains[63]. There are three different kinds of motions are seen at three different time scales characterized by two crossover time scales i.e. relaxation time τ_ξ, of correlation blob of size ξ and relaxation time τ_{2R_0}, of a polymer blob of size comparable to the size of the particles. At short time scales when $t < \tau_\xi$, the particles feel local viscosity of the solution and follow diffusive motion where

$$\tau_\xi \approx \frac{\eta_s \xi^3}{k_B T} \quad (2.9)$$

During intermediate times $\tau_\xi < t < \tau_d$,the particles' motion is subdiffusive and the viscosity experienced by particles is time dependent and the effective diffusion coefficient is given by:

$$D_{eff} \sim \frac{k_B T}{2R_0 \eta_{eff}(t)} \quad (2.10)$$

$$D_{eff} \, \alpha \frac{1}{\eta_{eff}(t)} \quad (2.11)$$

where $\eta_{eff}(t)$ is the effective viscosity experienced by the particles inside a solution:

$$\eta_{eff}(t) \approx \eta_s \left(\frac{t}{\tau_\xi}\right)^{\frac{1}{2}} \quad 2.12$$

At longer time scales $t > \tau_d$, the motion of particles is again diffusive and the effective viscosity η_{eff} experienced by the particles is directly proportional to the number of correlated blobs of size of the particles size is given by:

$$\eta_{eff} \approx \eta_s \left(\frac{2R_0}{\tau_\xi}\right)^2 \quad 2.13$$

And the effective terminal diffusion coefficient is:

$$D_t \approx \frac{k_B T}{2R_0 \eta_{eff}(\tau_d)} \approx \frac{k_B T \xi^2}{\eta_s (2R_0)^3} \quad 2.14$$

$$D_t \, \alpha \, (2R_0)^{-3} \quad 2.15$$

(c) For large particle size range ($2R_0 = d > a$): When the particles are in size range larger than tube diameter/ entanglement length a, the motion of particles is characterized by a crossover time i.e. relaxation time τ_e , of an entanglement strand where the particle's motion is obstructed. At short time scales $t < \tau_e$, the particles' motility is similar as that of intermediate particle size range but at time scales $t > \tau_e$, the particles motion is halted by the obstruction caused by entanglement strands of polymers. The particles can escape such motional traps during the relaxation time of polymer liquid characterized by a time scale called as reptation time τ_{rep}. The effective diffusion coefficient due to reptation can be written as:

$$D_{rep} \approx \frac{k_B T}{\eta d} \quad 2.16$$

$$D_{rep} \, \alpha \, \frac{1}{d} \quad 2.17$$

Cai *et. al.* divided polymer solutions based on two crossover concentrations[57] ϕ^{ξ} and ϕ^{a}. If the polymer concentration is less than ϕ^{ξ}, then the diffusion coefficient of particles is not dependent on polymer concentration. The diffusion can be simply be characterized by solvent's viscosity η_s. At intermediate concentrations i.e. ($\phi^{\xi} < \phi < \phi^{a}$): the particles' diffusion is affected by the segmental dynamics of polymer chains. For athermal solvent as shown in figure 2.1.1.1, the diffusion coefficient of particles is expected to scale as:

$$D \sim \phi^{-1.52} \qquad 2.18$$

And for large particles in the polymer concentrations above ϕ^{a}, the diffusion coefficient scales with volume fraction as below

$$D \sim \phi^{-3.93} \qquad 2.19$$

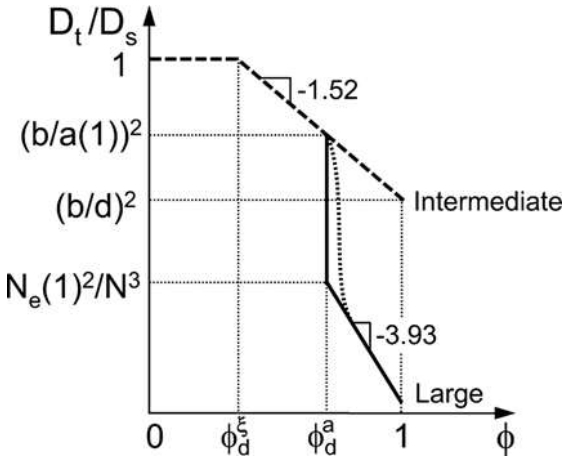

FIGURE 2.1.1.1: Dependence of terminal diffusion coefficient D_t of particles in entangled polymer solutions normalized by their diffusion coefficient D_s in pure solvent. Dashed line is for intermediate size particles (($b < d < a(1)$), (b= ξ in text) and solid line is for large size particles ($d > a(1)$). ϕ_{ξ}^{d} and ϕ_{a}^{d} are the crossover concentrations (ϕ^{ξ} and ϕ^{a} in text), at which the correlation length ξ and the tube diameter a are on the order of particle size d. (Reprinted with permission from Macromolecules 44(19), 7853-7863. Copyright (2011)).

2.1.2 PREVIOUS COMPUTATIONAL STUDIES:

Liu *et. al.* used molecular dynamics (MD) simulations to study the nanoparticle diffusion in polymer melts[64]. Their simulation results indicated that polymers' radius of gyration R_g is the length scale of interest for the validity of Stokes Einstein (SE) equation for the diffusion of nanoparticles inside aqueous polymer solutions. They also studied the dependence of particles' diffusion within polymer melts on particles' size, polymer concentrations, polymer-particle interactions, mass of particles, chain length of polymers. For the cases when R_g is smaller than the size of the probe particles R_0, SE diffusion results are accurate. When $R_g$of the polymer is larger than the size of nanoparticles, nanoparticle diffusion is polymers' molecular weight independent but depends on the mass of particles and SE law doesn't provide correct diffusion results as the viscosity experienced by nanoparticles is nanoviscosity instead of microviscosity. They observed macroviscosity to nanoviscosity transition in the viscosity experienced by nanoparticles with increase in polymer chain's length.

Ganesan *et. al.* investigated the mobility of nanoparticles within unentangled polymer melts[65] analytically and through computational simulations. They proposed a modified continuum model for long-time diffusion of particles inside polymer melts. It was suggested that R_g is the length scale that controls the transition from nano to microviscosity in the cases where $\xi < R_0 \leqslant R_g$. They claimed that for the observation of viscosity reduction, entanglement is not necessary in polymer solutions. However, a much stronger effect was seen on reduction of viscosity in the entangled regimes. Their studies also rationalized a few previous experimental results of dynamics of nanoparticles inside polymer melts.

2.1.3 PREVIOUS EXPERIMENTAL WORK

Optical microscopy had several advancements in their imaging methods being able to visualize and quantify the dynamical information for micro to nanoscales. High-resolution microscopic methods such as stimulated emission-depletion (STED)[66] microscopy, photoactivated localization microscopy (PALM)[67] and parameter extraction from reconstructing images (PERI)[68] broke the classical diffraction limit and enabled us to study colloidal and biological structures at much smaller scales with higher precision than any previous ways. But the barrier imposed by slow time resolution of image acquisition in such methods has limited the analysis to mostly structural. To overcome this limit, there are a few other emerging techniques that do not rely on serial scanning. Digital cameras with ultrafast acquisition speeds are being used to bring improvements in colloidal dynamical studies.

Holyst and co-authors[51] investigated the viscosity scaling of aqueous solutions of polyethylene glycol PEO with different molecular weights ranging from 6000-20000 g/mol with dye/protein molecules as nanoprobes in the size range of 1.7-114 nm. They used fluorescence correlation spectroscopy (FCS) and capillary electrophoresis for the experimental investigations. They found that the polymers' radius of gyration R_g is the crossover length scale of viscosity instead of the polymers' blob correlation length ξ as suggested by MD simulations but in contrast to the theory. As per their results, particles with radii R_0 greater than R_g, the particles experience macroviscosity η_{macro} but in the opposite size limit, particles experience nanoviscosity η_{nano} as shown below:

$$\frac{\eta_{nano}}{\eta_0} = e^{[b\left(\frac{R}{\xi}\right)^a]} \quad 2.20$$

$$\frac{\eta_{macro}}{\eta_0} = e^{[b\left(\frac{R_g}{\xi}\right)^a]} \quad 2.21$$

where, η_0 denotes the viscosity of water with a and b are constants with values close to 1.

Positive deviations from SE equation were also reported by Ye and co-authors for particles with length scales equal or smaller than polymers' correlation length as a result of reduction in local viscosity[69]. They carried out the motion and adsorption experiments by using methods of dynamic light scattering and sedimentation[70].

Kohli *et. al.* studied the effect of length scales on the diffusion of gold nanoparticles (AuNPs) within aqueous solutions of poly ethylene glycol (PEO) in semidilute concentrations[71]. They used two-photon FCS method to experimentally determine the translational diffusion coefficients of nanoparticles. They indicated a crossover length scale i.e. radius of gyration R_g of polymer chains above which the nanoparticles do not experience the bulk viscosity η; but a much lower viscosity called as nanoviscosity. For particles with radii R_0 greater than R_g; the obtained diffusion coefficients D are in good agreement with Stokes Einstein (SE) predictions $D_{SE} = \frac{k_B T}{6\pi\eta R_0}$ whereas for particles sizes smaller or equal to R_g, Stokes Einstein dependence breaks down and the ratio $\frac{D}{D_{SE}}$ increases with increase in polymer concentrations.

2.2 DYNAMICS AND MELTING OF COLLOIDAL STRUCTURES FORMED ON TOP OF CURVED SURFACES

Dynamics and phase change processes in self-assembled anisotropic colloids on a curve still needs to be clearly understood. Among all phase transition studies in colloidal systems, crystallization i.e. transition from liquid phase to crystal phase is the most intensively studied process. In contrast to 3D crystallization and melting, 2D investigations are limited. Freezing and melting processes in 2D share the same equilibrium phases but different kinetics. Defects are significantly important in melting process but not in freezing. There is a lack[28] of fundamental theory that can explain the first order phase transitions.

Hard sphere system is the extensively studied model in phase transition of colloidal

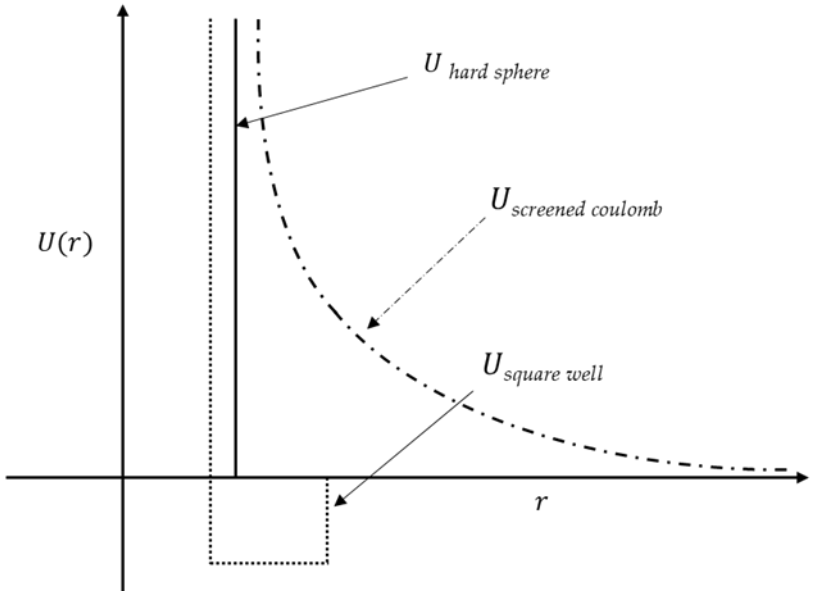

FIGURE 2.2.1: Different kinds of interparticle potentials i.e. hard sphere, screened coulomb and square well potential.

systems[72-79]. According to that, in a two-particle system, the pair interaction potential has a zero value everywhere else other than where the surfaces of both particles come into contact. As a result, particles feel a repulsive force at contact that prevents overlapping. Therefore, it can be said that the geometry and entropy is the determining factor of any phase in hard sphere system.

Particle volume fraction ϕ plays a similar crucial role in a hard sphere system as the inverse temperature plays in a condensed phase formed by attractive[80] molecular system. In a dilute concentration of particles, a normal Brownian diffusion is observed with no phase change. But a first order phase transition from a disordered to ordered state takes place in the crowded media formed by increasing particle volume fraction in a hard sphere system. This phase transition that takes place through a co-existence regime[81] occurs as a consequence of net increase in entropy from the disordered liquid-like phase to solid-like phase. In a crystal phase, the entropy loss due to ordered configuration in solid state is less that the gain in entropy due to the increase in space per particle for unobstructed motion when the particles arrange themselves into ordered structures. Such colloidal disorder-order transitions[82],[83] [84] begin to occur roughly at ϕ ~= 0.494 where crystal phases are in equilibrium with liquid phases. The radial distribution function $g(r)$ for a pair of particles separated by a distance r with no internal structure is given by:

$$g(r) = \exp[-U(r)/k_B T] \qquad 2.22$$

where, $U(r)$ is the potential of mean-force that can be expanded in higher order terms for many-body contributions as below:

$$U(r) = \sum_{i,j} w_{ij}(r) + \sum_{i,j,k} w_{ijk}(r) + \cdots \qquad 2.23$$

And the radial distribution function $g(r)$ tends to value 1 at large distances and 0 at very short distances. Basically, the inter-particle potentials can be of three kinds i.e. hard sphere, square well and screened coulomb potential as shown in figure 2.2.1. The famous Ornstein-Zernike equation[85] can describe inter-particle interactions in case of non-dilute hard sphere system by relating the

direct correlation function $c(\vec{r})$ and the total correlation function $h(\vec{r})$ for direct and indirect interparticle interactions (figure 2.2.2),

$$h(\vec{r}) = c(\vec{r}) + \bar{N} \int d\vec{r}' \; c(\vec{r} - \vec{r}')h(\vec{r}') \qquad 2.24$$

where, particle number density is denoted by $\bar{N} = N/V$ with N as number of particles in volume V and $h(r) = g(r) - 1$.

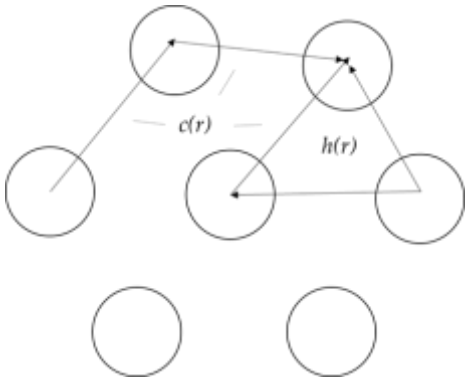

FIGURE 2.2.2: Direct and indirect interparticle interactions denoted by $c(\vec{r})$ and $h(\vec{r})$ respectively.

In the reciprocal space, Ornstein-Zernike integral equation can be written as:

$$H(q) = C(q) + \bar{N}\, C(q)H(q) \qquad 2.25$$

The so-called structure factor $S_I(q)$ for particulate systems[86] is defined as:

$$S_I(q) = 1 + \bar{N}\, H(q) = \frac{1}{(1 - \bar{N}C(q))} \qquad 2.26$$

The numerical solution of above Ornstein-Zernike equation yields scattering structure factors in real microscopic systems composed of hard spheres. This equation contains two unknown variables i.e. direct correlation function and the total correlation function and therefore can be best solved by using the Percus-Yevick approximation[87] that uses a closure relation. The Percus-Yevick closure relation uses hard sphere inter-particle potential (figure 2.2.1) and provides a

single analytical solution to the Ornstein-Zernike integration. According to Percus-Yevick approximation, the direct correlation function $c(\vec{r})$ can be written as:

$$c(r) = g(r)[1 - \exp(-\frac{w(r)}{k_B T})] \quad 2.27$$

With the following assumptions for hard sphere potential for spherical particles of effective diameter d:

$$\begin{cases} w(r) = 0 \ ; \ r > d \\ w(r) = \infty \ ; \ r < d \end{cases} \quad 2.28$$

Which yields the analytical solution to Ornstein-Zernike equation:

$$\begin{cases} c(r) = 0 \quad ; \ r > d \\ c(r) = -\lambda_1 - 6\phi\lambda_2 \frac{r}{d} - \frac{\phi}{2}\lambda_1 \frac{r^3}{d^3} = \infty \ ; \ r < d \end{cases} \quad 2.29$$

With λ_1 and λ_2 are defined as:

$$\lambda_1 = \frac{(1 + 2\phi)^2}{(1 - \phi)^4} \quad 2.30$$

$$\lambda_2 = -\frac{(1 + \phi/2)^2}{(1 - \phi)^4} \quad 2.31$$

And volume fraction ϕ of scattering particles

$$\phi = \pi \bar{N} d^3/6 \quad 2.32$$

The structure factor $S_I(Q)$ for a colloidal solution can now be found by calculating the Fourier transform of direct correlation function $c(\vec{r})$ given by $\bar{N}C(q)$ below:

$$S_I(Q) = \frac{1}{(1 - \bar{N}C(q))} \quad 2.33$$

where,

$$\bar{N}C(q) \qquad 2.34$$

$$= -24\phi\left\{\lambda_1\left[\frac{\sin(qd)-(qd)\cos(qd)}{(QD)^3}\right]\right\} - 6\phi\lambda_2\left[\frac{(qd)^2\cos(qd)-2(qd)\sin(qd)-2\cos(qd)+2}{(qd)^4}\right]$$

$$-\frac{\phi\lambda_1}{2}\left[\frac{(qd)^4\cos(qd)-4(qd)^3\sin(qd)-12(qd)^2\cos(qd)+24(qd)\sin(qd)+24\cos(qd)-24}{(qd)^6}\right]$$

2.2.1 PREVIOUS THEORETICAL WORK

In 1970s, the predominant microscopic melting theory called as Kosterlitz Thouless Halperin Nelson Young (KTHNY) theory was developed[88,89]. KTNHY theory predicts that inside two-dimensional colloidal crystals, the melting takes place in two continuous phase transitions. According to this theory, the melting is driven by the appearance of thermally activated topological defects (dislocations and disinclinations) in the crystallic state that has long range translational and long range bond orientational order. According to Kosterlitz, Thouless and Young's predictions during the decade of 1970, the dislocation defects of crystallic sites dissociate and as a result, number of free dislocation defects increases at the melting temperature T_m. It was predicted that this intermediate disordered phase called as hexatic still contains short-range translational and sixfold quasi long-range orientational order. At some higher temperature, another continuous transition takes place giving rise to even more defects including the unbinding of dislocations into disclinations giving rise to a highly disordered isotropic liquid state. The translational and orientational orders can be expressed by calculating correlation functions i.e. radial distribution/pair correlation function $g(r)$, the bond orientational correlation functions $g_6(r)$ and six-fold bond-orientational order parameter ψ_6 defined by:

$$g(r) = \frac{V}{N}\langle \sum_{i,j\neq I} \delta(\vec{r} - \overrightarrow{r_{ij}})\rangle \quad 2.35$$

$$g_6(r) = < \psi_6^*(0)\, \psi_6(\vec{r}) > \quad 2.36$$

$$\psi_6(r_i) = \frac{1}{n}\sum_{j=1}^{n} \exp[i6\Theta(r_{ij})] \quad 2.37$$

where, n = number of nearest neighbors, V is volume, N: total number of particles and $\Theta(r_{ij})$: angle betweeen the vector connecting the central particle, i , with neighboring particles, j, and a fixed reference axis. The bond-orientational order parameter ψ_6 is calculated by finding the average of the absolute value of $\psi_6(r_i)$ and its value should be 1 for a perfect hexagonally packed crystal and any value less than 1 is considered as a phase with lost local hexagonal order.

There are other several contrasting theories that suggests that the phase transitions are of first order instead. Few theoretical approaches predicted that the melting phenomenon is driven by grain boundaries[90,91]. First-order behavior of melting was suggested from the condensation of defects[92]. The effect of topological vs. geometrical defects[93] in 2D melting was also studied.

Few simulation methods numerically indicated that the hexatic phase in 2D melting is metastable[94,95] or a first order phase transition[96] that was initially believed to depend on the effects produced by finite-size[97] in hard sphere interactions where fluctuations were considered extremely important. Contrastingly, the fluctuations were supposed to be insignificant in the systems with long-range pair potentials.

2.2.2 PREVIOUS COMPUTATIONAL WORK

Engel and group investigated and reported the hard-disk's equation of state using large-scale event-driven molecular dynamic (EDMD) simulations[98]. The phase transition of hard-disk's system at high densities was studied using Monte Carlo algorithms. Their analysis and results confirmed the existence of the hexatic phase and 2D liquid-hexatic transition to be of first order.

Qi *et. al.* performed large scale EDMD simulations[99] to study the melting phenomenon in a quasi-two-dimensional system of hard disks confined between two parallel hard walls. Basically, they focused on how excluded-volume interactions i.e. out of plane fluctuations effect the phase transitions. Surprisingly, they found that the two-stage melting stills persists in the same way as it would in the case of hard disks. There is no effect of out of plane fluctuations (as high as half the particle diameter) on the hexatic phase's sustainability. Also, it was strogly indicated from their results that hexatic to liquid phase seems to be driven by the formation of grain boundary scars (clusters fromed by string-like defects) is a first order phase transition (contradictory to KTNHY theory) as shown by Mayer-wood loops in the equation of state.

2.2.3 PREVIOUS EXPERIMENTAL WORK

Presently, there are several real-space experimental techniques available to study the structure and dynamics of colloidal assembly such as optical microscopy, electron microscopy and scattering techniques such as light scattering[100], neutron scattering[101] and x-ray scattering[102]. But so far, optical microscopic methods are the most useful and direct for providing mechanisms, structure and dynamics of assembly and their phase changes. First order phase transitions are easy to be experimentally observed and identified through a few ways, such as, from the coexistence curve of both phases at equilibrium and jumps in certain translational correlations

functions/orientational order parameters. Experimentally, the kinetics of 2D melting which is beyond the scope of 2D melting theories has been poorly understood[103] in a few aspects.

Phase transitions in critical binary solvents was extensively studied during 1970s using light microscopy and scattering methods. Kim *et. al.* gave the experimental evidence for the influence of hydrodynamics in a binary mixture[104]. They used microscopy and light scattering to study the phase behavior of a critical mixture of water and 2,6-lutidine. They observed an unexpected increase in the nucleation growth rate and the temporal fluctuations at small angles gave rise to strong non-Lorentzian power spectra.

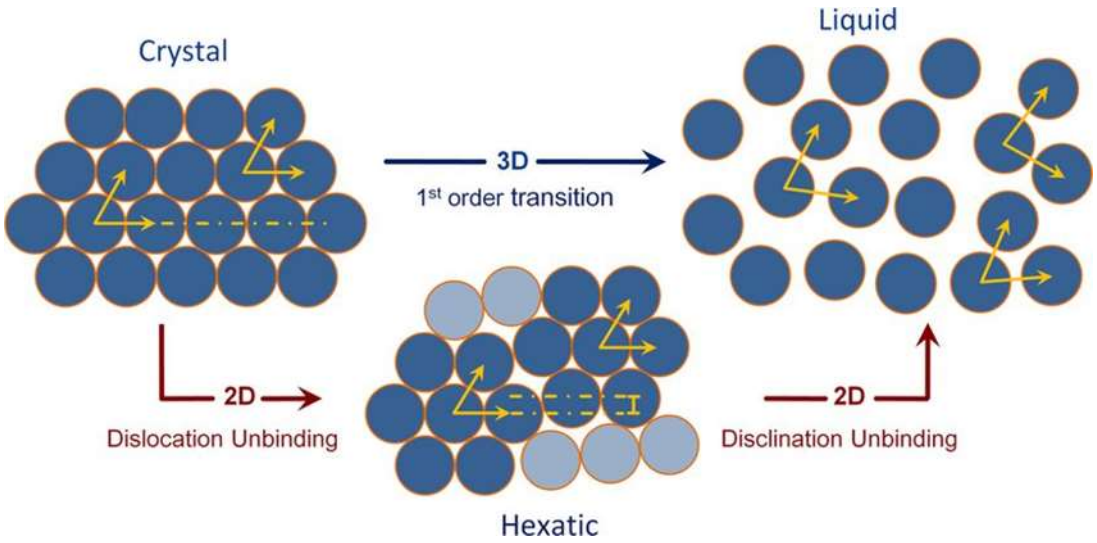

FIGURE 2.2.3.1: 2D melting shown as a two-step melting process in contrast to one step 3D melting. The intermediate hexatic phase in between crystal and liquid phase as predicted by the KTHNY theory is shown in the middle. (Reprinted with permission from Scientific reports vol. 6, 2045-2322 Copyright (2016)).

Rodrigo *et. al.* recently showed how the freezing proceeds on the surface of a sphere through the formation of a crystal like "continent" that forces defects into 12 isolated "seas" with same symmetry as viruses[27]. They constructed a new parameter that can explain the long-range orientational order present in the crystal lattice[27].

Pal *et. al.* observed the hexatic phase in between the nematic and hexagonal phases in self-assembled amphiphilic molecules using small-angle x-ray scattering (SAXS) method[105]. This is the first experimental validation of existence of a thermodynamically stable hexatic phase (figure 2.2.3.1) as predicted KTHNY theory in a 3D system composed of self-assembled micellar polymers.

Ruben *et. al.* has experimentally investigated and linked the slow dynamics of dense suspensions consisting of charged colloids to their microscopy connectivity using 3D confocal microscopy technique[106]. They studied the system dynamics from the particle's trajectories over time and the dynamic structure was determined from the real-space van Hove correlation functions. Although they observed no significant change in the local structure but a drastic change observed in the dynamics with change in particles' concentrations (volume fractions). They mainly quantified the slowing down of relaxations in a liquid in terms of two distinct decays called as α and β relaxations as determined from fitting intermediate scattering functions to a doube stretched exponential.

Brodin *et. al.* investigated the melting of two-dimensional colloidal structures formed by glycerol droplets trapped at the interface of nematic liquid crystal (NLC) and air[107]. Their experiments supported the predictions of KTHNY theory which confirmed the existence of hexatic phase using video microscopy.

Lin *et. al.* presented a simple but robust method for investigation of self-assembly and transport of nanoparticles at liquid-liquid interfaces[108] formed by water and toulene. Using confocal microscopy, they found that the nanoparticle self assemby is dependent on the particle's

size. Also, a photoinduced transport mechanism of nanoparticles is also observed through which the nanoparticles changed their solubility from toulene to water and got transported from toulene to water via a toulene-water interface and finally got dispersed in water. Later, they also investigated the structure and dynamics of cadium selenide (CdSe) nanoparticles[109] at fluid interfaces using three experimental methods i.e. electron microscopy, x-ray scattering and atomic force microscopy (AFM). Flourescence photobleaching was used to quantify the two dimensional dynamics of nanoparticles and liquid-like behavior was observed. These results have implications on the synthesis of self assembled nanostructures. Lin *et. al.* performed computer simulations and found that the 2D melting with dipole-dipole interactions is of second order[110].

Recently, Ortileb and co-authors investigated statistics of colloidal suspensions of the green algae[111] *Chlamydomonas reinhardtii.* According to their analysis, the measured probability distribution functions of experimental trajectories of algae suspensions are non-Gaussian for intermediate time scales. Similar to this study, Wu *et. al.* found that the micron sized beads freely suspended in a bacterial soap bath show superdiffusive behavior at short times while normal diffusion at longer time scales[112]. Leptos *et. al.* also performed experimental diffusion investigations of micron sized spheres in algae[113] *Chlamydomonas reinhardtii (CR).*

Chou and co-authors used light scattering and direct microscopy to study dynamics of phase separation in a critical binary mixtures of isobutyric acid-water and 2, 6- lutidine-water[114]. They confirmed that the growth of droplets speeds up with fluid flow caused by the curvature of surfaces that are irregular in shape and interpenetrates the nucleating fluid.

Jayalakshmi and Kaler studied the phase behavior of colloids (negatively charged silica particles) in a binary fluid mixture formed by 2-butoxyethanol and 2,6 methyl pyridine (lutidine) using light scattering[115]. Their phase studies show an observation of a second phase separation in the solvent phase that coexists at a lower temperature. With continuous heating, the mixture came to an equilibrium state but the phase boundary of the binary liquid is not seen. Phase behavior at different temperatures is studied at different solvent concentrations.

2.3 TRANSLATIONAL AND ROTATIONAL DIFFUSION OF ANISOTROPIC COLLOIDS

2.3.1 PREVIOUS WORK

In the case of anisotropic colloids, for example, rods, give rise to translation and rotation diffusion both. Depending on the shape anisotropy, there are three theoretical models that can be used to find the translational and rotational diffusion coefficients. They are called as hydrodynamic stick (HS) theory[116], Tirado and Garcia de la Torre's (TT) theory[117-119]and Broersma relations[120,121]. The predictions of these theories are further stated in this section. TT and HS theories are applicable to rods of all aspect ratios, but Broersma relations are only suitable for rods with aspect ratio greater than 3.5. According to stick hydrodynamic theory, for prolate spheroids ($a > b$), where $2a = L$ is the length of major axis and $2b = d$ is the length of minor axis, the predictions say: $D_a = k_B T/\gamma_a$ and $D_b = k_B T/\gamma_b$

$$\gamma_a = \frac{(a^2 - b^2)16\pi\eta}{(2a^2 - b^2)s - 2a} \qquad 2.39$$

$$\gamma_b = \frac{(a^2 - b^2)32\pi\eta}{(2a^2 - 3b^2)s + 2a} \qquad 2.40$$

and

$$s = \frac{2}{\sqrt{a^2 - b^2}} \log \frac{a + \sqrt{a^2 - b^2}}{b} \quad 2.41$$

where γ_a and γ_b are translational viscous friction coefficients in directions parallel and perpendicular to major axis of ellipsoids**.** In bulk;

$$D_T = (D_a + 2D_b)/3 \quad 2.42$$

$$D_a = \frac{k_B T[\ln(2r) - 0.5]}{4\pi\eta a} \quad 2.43$$

$$D_b = \frac{k_B T[\ln(2r) + 0.5]}{8\pi\eta a} \quad 2.44$$

$$D_R = \frac{3k_B T[\ln(2r) - 0.5]}{8\pi\eta a^3} \quad 2.45$$

$$r = \frac{a}{b} \quad 2.46$$

For rotational diffusion:

$D_{Ra} = k_B T/\gamma_a^r$ and $D_{Rb} = k_B T/\gamma_b^r$

where,

$$\gamma_a^r = \frac{32\pi\eta(a^4 - b^4)}{3(2a^2 - b^2)s - 2a} \quad 2.47$$

$$\gamma_a^r = \frac{32\pi\eta(a^2 - b^2)b^2}{3(2a - b^2 s)} \quad 2.48$$

γ_a^r and γ_b^r are the rotational friction coefficients around and perpendicular to the prolate axis.

Translational diffusion coefficient as given by TT theory:

$$D_T = \frac{k_B T}{3\pi\eta L}[\ln\left(\frac{\mathrm{L}}{\mathrm{d}}\right) + \nu \quad 2.49$$

where, $\nu = 0.312 + 0.565\frac{d}{L} - 0.1\frac{d^2}{L^2}$

And rotational diffusion coefficient

$$D_R = \frac{3k_BT}{\pi\eta L^3}(\ln\left(\frac{\mathrm{L}}{\mathrm{d}}\right) + \sigma) \quad 2.50$$

where, $\sigma = -0.662 + 0.917\frac{d}{L} - 0.05\frac{d^2}{L^2}$

According to Broersma's relations for diffusion, the translational coefficient is given by:

$$D_T = \frac{k_BT}{3\pi\eta L}[\ln(\delta) - 0.5(\gamma_a + \gamma_b)] \quad 2.51$$

Where, $\delta = \ln(\frac{2L}{d})$, $\gamma_a = 0.807 + \left(\frac{0.15}{\delta}\right) + \left(\frac{13.5}{\delta^2}\right) - \left(\frac{37}{\delta^3}\right) + \left(\frac{22}{\delta^4}\right)$

And $\gamma_b = -0.193 + \left(\frac{0.15}{\delta}\right) + \left(\frac{8.1}{\delta^2}\right) - \left(\frac{18}{\delta^3}\right) + \left(\frac{9}{\delta^4}\right)$

$$D_R = \frac{3k_BT}{\pi\eta L^3}(\delta - \xi) \quad 2.52$$

Where, $\delta = \ln(\frac{2L}{d})$ and $\boldsymbol{\xi} = 1.14 + \left(\frac{0.2}{\delta}\right) + \left(\frac{16}{\delta^2}\right) - \left(\frac{63}{\delta^3}\right) + \left(\frac{62}{\delta^4}\right)$

Han *et. al.* measured the rotational Brownian motions of single ellipsoids in a quasi two dimensional confinements[122]. They measured short-time anisotropic and long-time isotropic rotational diffusion along the long and short axes of ellipsoids using video microscopy. They found that confinement in 2D alters the diffusion anisotropy (diffusion along the long and short axes) and the diffusion along the short axis much slower than the bulk diffusion in 3D.

Vasanthi *et. al.* performed molecular dynamics (MD) simulations of translation and rotation of both oblates and prolate spherioids of different aspect ratios[116]. They found anisotropic diffusion in the direction parallel and perpendicular to the major axis in short times whereas

isotropic in long times. They also determined the scaling of diffusive motion to the aspect ratios of rods. Recently, Heyes used MD simulations to study the translational and rotational diffusion of rod shaped molecules.

Cush *et. al.* used depolarized dynamic light scattering to determine the translational as well as rotational diffusion of tobacco mosaic virus (TMV) within aqueous polymer solutions of flexible carbohydrate dextran (M_W ~ 505,000)[123]. They observed a decrease in rotational and translational diffusion with increase in polymer concentrations. They also found a cross over concentration of about 6.5 % above which the Stokes-Einstein relation fails. Later, they measured the translational and rotational diffusion of TMV in extended and globular polymer solutions[124] using the same experimental method and found that the shape of TMV can be considered as an effective probe in microrheology.

Alam *et. al.* investigated translational and rotational diffusion of gold nanorods within various entangled solutions of polyethylene glycol (PEG) solutions with different molecular weights[125]. They used multi-photon fluctuation correlation spectroscopy (FCS) to calculate the nanoviscosity experienced by nanorods within different PEG concentrations. The resulted translational and rotational diffusion coefficients were compared to different theories. They alsoo studied the effects of nonhydrodynamic friction and polymer dynamics in the transport of nanorods.

FCS was also used for studying nanorods'(NRs) diffusion and their dependence on aspect ratios by Tsay and group[126]. Rotational diffusion was found to be more sensitive to change in rods' sizes and occuring at faster time scales than the translational diffusion. They studied non

specific binding of peptide-coated NRs with bovine serum albumin (BSA) by titrating and reported that rotational diffusion coefficient can be used an aid for studying binding and dynamics of conformations in biology.

CHAPTER 3

EXPERIMENTAL METHODS

Microscopic methods provide useful information about microscopic systems such as their shape and surface topography. Scattering techniques are very useful to study the correlations among positions and motions of the nanoparticles inside polymeric solutions. Traditionally, many light-scattering instruments and imaging techniques are used to gather useful information about the dynamics of a wide range of processes, for example, Brownian motion of colloidal - particles, diffusion of nanoparticles inside proteins and polymer solutions, fluctuations in density of gases and liquids, intensity correlations of nanoparticles in polymer and electrolyte solutions, anisotropic diffusion of nanorods, change in dynamics of nanoparticles in gel-like polymer solutions with aging of the sample, etc[127]. There are many techniques available for determining the diffusion of micro and nanoparticles inside polymer solutions. The experimental techniques that I used in my research projects are as follows:

3.1 FLUORESCENCE CORRELATION SPECTROSCOPY (FCS)

3.1.1 INTRODUCTION TO FCS

Fluorescence correlation spectroscopy (FCS), first developed by Madge, Elson and Webb[128] in 1972, is a fluctuation correlation spectroscopy technique, which detects spontaneous microscopic fluctuations in number density and positions of molecules in dynamical processes. It is useful for measuring both the translational and rotational diffusion. FCS was further developed in 1993[129], when a confocal illumination scheme was introduced. Since then FCS got

improved further and further in its sensitivity and productivity. FCS is applicable to many commercial, analytical, chemical and biological fields[130]. It was used to study the fluid dynamics of organic materials due to its high sensitivity[131]. It is also beneficial in studying the dynamics within living cells and enzymes[132].

FCS involves fluorescence, a process that involves a spontaneous de-excitation of electrons, which results in the emission of electrons at a certain wavelength. FCS requires very low concentration (picomolar to nanomolar) of samples to work properly as it is highly sensitive. The excitation can be one-photon or multiphoton. A two-photon excitation in shown in the figure

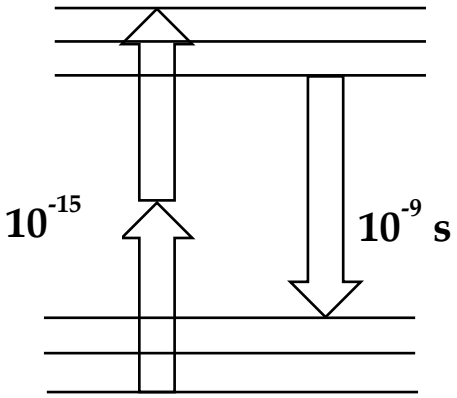

FIGURE 3.1.1.1: Two photon excitation used for FCS experiments involves absorption of two photons with effectively half the energy (λ= 800 nm) required for the excitation to take place and emission of single photon of about double their energy.

3.1.1.1. Sometimes, the sample under observation fails to show fluorescence, in that case the sample needs to be labeled with a fluorescent dye. It is possible for the dye to get photobleached, which means that it will permanently become unable to fluoresce because of the photo-induced chemical alterations. That is why there is a need to select a dye which has low photobleaching and high fluorescent yield. Some examples of dyes which are suitable for labeling are rhodamine derivatives i.e. tetramethylrhodamine (TMR) and carboxyrhodamine (Rh6G)[133]. FCS is able to measure tiny fluctuations inside the sample which can be a result of Brownian motion, chemical

reactions, etc[133]. FCS can be used in various situations e.g. in two-dimensional, three-dimensional diffusion and as well in the presence of flow in any direction as shown in figure 3.1.1.2. The

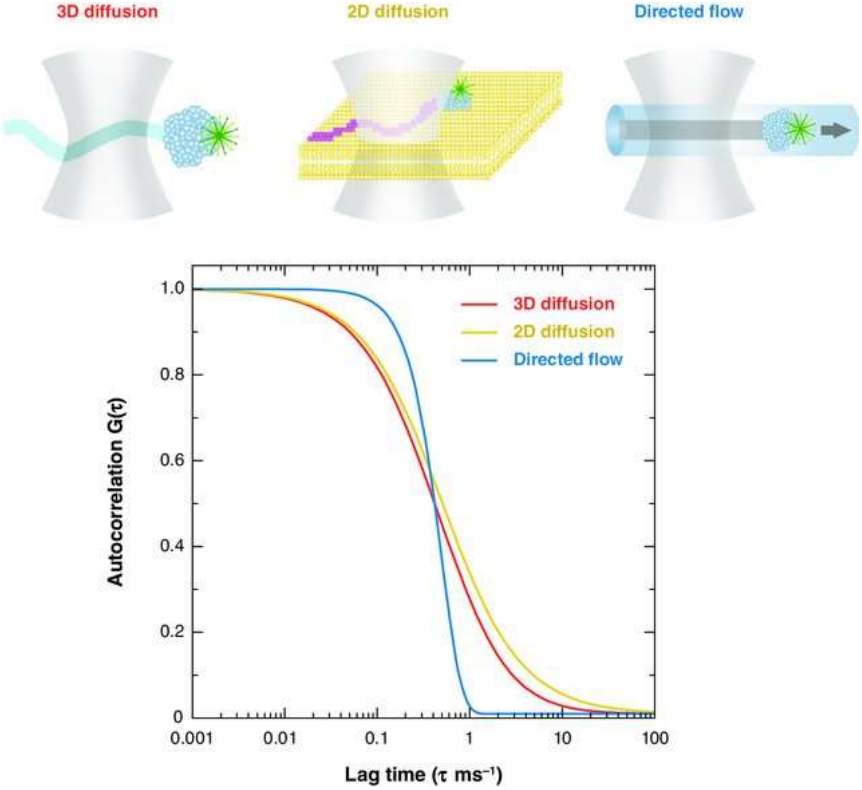

FIGURE 3.1.1.2: Different kinds of diffusion within the laser focus in FCS (Reprinted with permission from Annu. Rev. Biophys. Biomole. Struct. vol. 36, 151-169. Copyright (2007)).

fluctuations in fluorescence as a result of these dynamical processes can be quantified by a quantity known as an autocorrelation function (ACF), which measures the similarity with itself over a time lag τ (figure 3.1.1.3). It is defined by :

$$G(\tau) = \frac{< \delta F(t).\, \delta F(t+\tau) >}{< F(t) >^2} \qquad 3.1$$

where, $< F(t) >$ is the time average of fluctuation intensity and $\delta F(t)$ and $\delta F(t+\tau)$ are the fluctuations around the mean value of fluctuation intensity at time t and $t+\tau$, repectively.

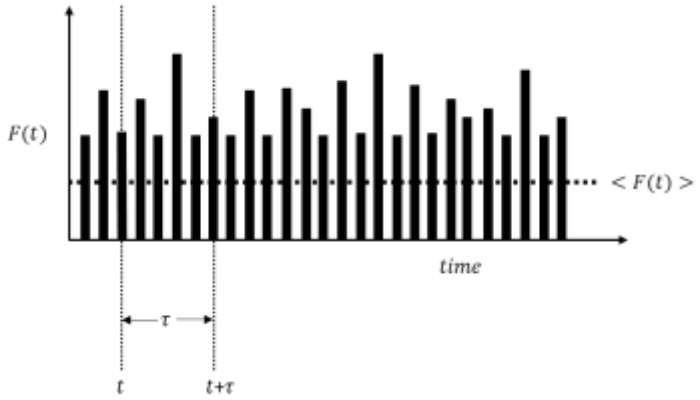

FIGURE 3.1.1.3: Fluorescence fluctuations $F(t)$ as detected by one photomultiplier tube with $< F(t) >$ as their mean value.

Instead of auto-correlation, we use cross-correlation function (CCF) in analysis of few experiments (figure 3.1.1.3). Having two channels is beneficial to obtain the common fluctuating fluorescence signals given by:

$$G_{ij}(\tau) = \frac{< \delta F_i(t).\delta F_j(t+\tau) >}{< F_i(t).F_j(t) >^2} \qquad 3.2$$

The obtained autocorrelation or crosscorrelation curves need to be fitted with a suitable

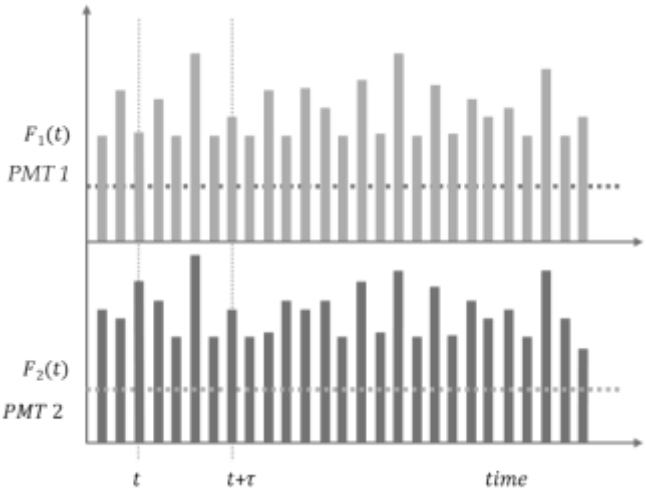

FIGURE 3.1.1.4: Fluorescence fluctuations $F_1(t)$ and $F_2(t)$ as detected by two photomultiplier tubes (PMT 1 and PMT 2) respectively with $< F(t) >$ as their mean value.

physical model in order to extract meaningful information[134]. There are different laser focus profiles are available for FCS fittings including 2D/3D Gaussian and Gaussian-Lorentzian. We can choose a suitable fitting model depending on the excitation type and dimensionality of

experimental system. Figure 3.1 shows the 2D and 3D diffusion, and directed flow with the laser focus profiles[135]

The laser source can be continuous i.e. one-photon excitation or pulsed i.e. two-photon excitation. Multi-photon excitations have several advantages to single-photon excitations. A two-photon transition involves absorption of two photons with double the wavelengths as required for the actual transition to happen and emission of one photon. For such three-particle events, an extremely high photon flux is required which can be provided through pulsed lasers. The probability of two-photon absorption is directly proportional to the square of excitation energy. And the intensity of light decreases quadratically as the distance from focal plane increases; therefore, a very tiny focal volume is excited in two-photon excitations as contrast to one-photon excitations. In contrast to one-photon excitations, there is no need of a pinhole making two-photon excitation better for highly photosensitive biological samples in order to prevent damaging due to light[136].

3.1.2 EXPERIMENTAL SET UP FOR FCS

The optics in FCS is inspired by the two-photon confocal microscopy invented by Denk, *et. al.* in 1990[133]. The set up can vary as per the needs of the experiments. The set up being used in our experiments is shown in the figure 3.1.2.1. The excitation used in our FCS is two-photon, where nanoparticles present inside the excitation volume absorbs two photons within a few femtoseconds[137]. As central to any FCS set up, there is a laser source, in our case, a high power (0.9 watts) femtosecond Ti:sapphire laser pulsing at high frequency (80MHz) that provides the required energy for a photon pair with wavelengths 800 nm for the excitation to take place. The laser light after coming out of the laser source is attenuated using a neutral density filter (NDF),

which is then directed towards the beam expander present inside a dark closed space after reflecting off a few mirrors. After the beam is expanded to a value to completely fill the objective's

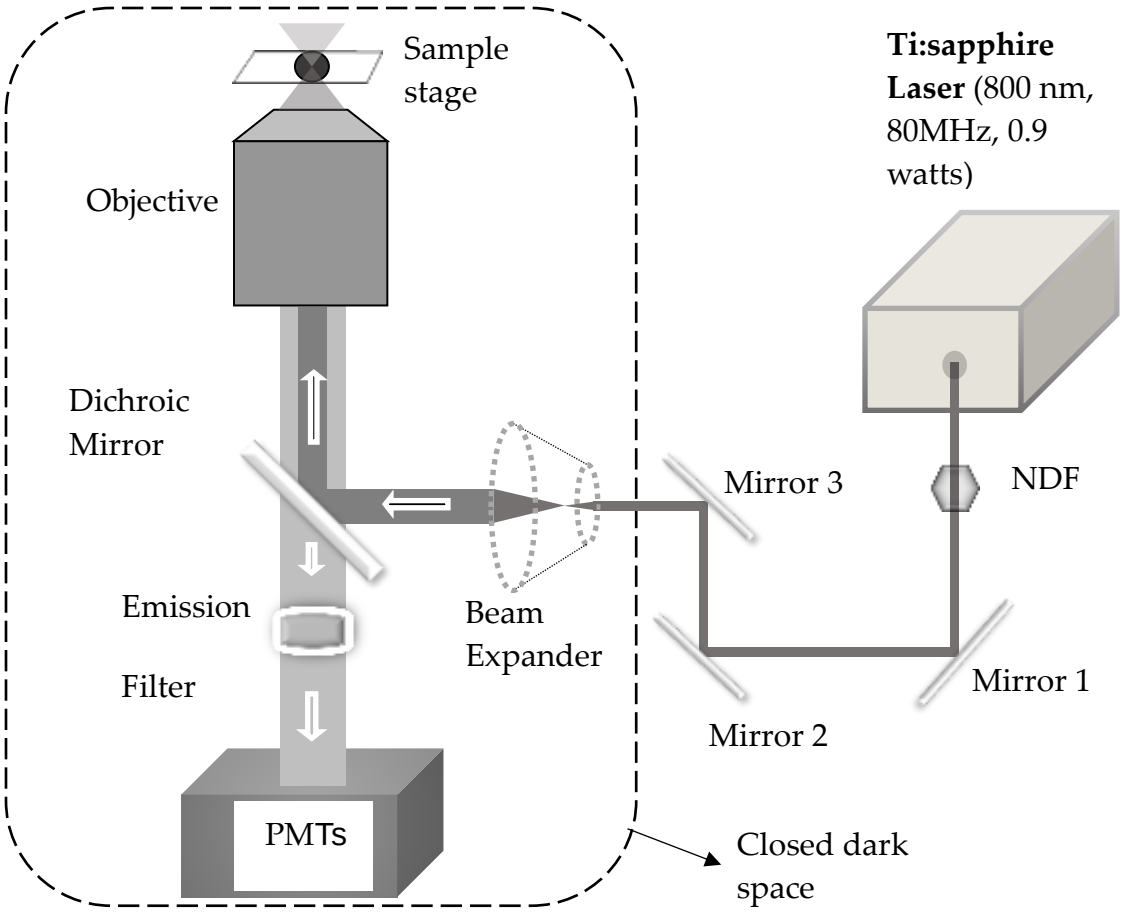

FIGURE 3.1.2.1: Experimental set up for FCS consisting of a laser source, mirrors, beam expander lenses, objective lens of high numerical aperture, a dichroic mirror, an emission filter and two photomultiplier tubes (PMTs) for fluorescence detection.

aperture, the laser beam gets reflected from a dichroic mirror, which reflects the wavelengths of 800 nm and transmits all below this value. Now the laser light is focused into the sample with the help of the objective of the microscope and a small volume is being excited in the sample. A nanoparticle then absorbs two photons and emits one photon. These fluorescence wavelengths of about 500 nm- 600 nm are then collected by the same objective and transmitted through the dichroic mirror and gets collected by two photomultiplier tubes (PMTs) after passing through an

emission filter to filter out any backscattered signals. We get photon counts with respect to time using the ISS software. By analyzing the data and correlation curves, we can get the desired properties of nanoparticles i.e. translational and rotational diffusion coefficients. If the viscosity of the medium is known, we can use Stokes-Einstein relation to determine the particle size. Conversely, for known particle size we can determine the medium's viscosity that the nanoparticles experience. This viscosity, also called as nanoviscosity can be substantially different from the bulk viscosity, which is measured in a rheometer.

3.1.3 FCS THEORY

FCS detects the fluctuations in emitted fluorescence light intensity. Such fluctuations in fluorescence at molecular levels arise due to many reasons including diffusion, external flows and chemical reactions occurring in the samples under investigation and can be quantified in

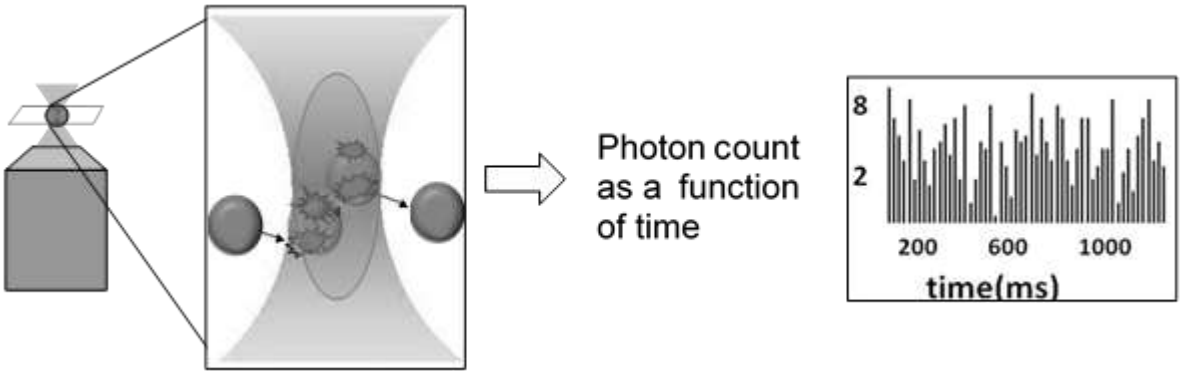

FIGURE 3.1.3.1: Profile of femtolitre laser focus as obtained by the objective lens. When the fluorescence molecules enter the laser focus, they emit photons and we record photon counts over time to get the autocorrelation function of fluorescence intensity.

terms of number of photons emitted when the fluorescent molecules pass through a small laser focus (figure 3.1.3.1). The fluorescence fluctuation intensity $\delta F(t)$ can be written as:

$$\delta F(t) \equiv F(t) - < F(t) > \qquad 3.3$$

where, $F(t)$ is fluorescence signal at any time t and $< F(t) >$ is the average fluorescence intensity signal.

In terms of spatial profile for a fluorescent dye concentration $C(r,t)$ at any location r at time t and the excitation light signal $E(r)$, $F(t)$ can be defined as:

$$F(t) = kQ \int E(r)C(r,t)dr \tag{3.4}$$

where, Q is a product of absorptivity and quantum efficiency of the optical system and k is a constant.

Also, fluorescence fluctuation intensity $\delta F(t)$ can now be written as:

$$\delta F(t) \equiv kQ \int E(r)\delta C(r,t)dr \tag{3.5}$$

with $\delta C(r,t)$ as the particle concentration change at any location r at time t given by:

$$\delta C(r,t) = C(r,t) - < C > \tag{3.6}$$

Thus, the autocorrelation function $G(\tau)$ over a time lag τ given by:

$$G(\tau) = \frac{< \delta F(t).\delta(F+\tau) >}{< F(t) >^2} \tag{3.7}$$

which reduces to

$$G(\tau) = \frac{\iint E(r)E(r') < \delta C(r,t).\delta C(r',t+\tau) > drdr'}{(< C > \int E(r)dr)^2} \tag{3.8}$$

For a 3D Gaussian laser beam profile with beam's half-width ω_0 and half-height z_0 for a two-photon excitation, $E(r)$ is given by:

$$E(r) = E(x,y,z) = E_0 \exp(-\frac{4(x^2+y^2)}{\omega_0^2} - \frac{4z^2}{z_0^2}) \quad 3.9$$

Fick's second law relates the change in fluorescence particle concentration $\partial\delta C(r,t)$ with diffusion coefficient D of particles moving in a Brownian motion as follows:

$$\frac{\partial\delta C(r,t)}{\partial t} = D\nabla^2\delta C(r,t) \quad 3.10$$

with a solution in the form of

$$\delta C(r,t) = \frac{< C >}{\sqrt{4\pi Dt}} \exp(-\frac{r^2}{4Dt}) \quad 3.11$$

We can find the diffusion coefficients by autocorrelating the change in particles' concentration over time as shown in the equation below:

$$G(\tau) = \left(\frac{2\sqrt{2}}{\pi\sqrt{\pi}\omega_0^2 z_0 < C >}\right) \frac{1}{(1+\frac{8D\tau}{\omega_0^2})\sqrt{1+\frac{8D\tau}{z_0^2}}} = \frac{G(0)}{(1+\frac{8D\tau}{\omega_0^2})\sqrt{1+\frac{8D\tau}{z_0^2}}} \quad 3.12$$

Fluorescent particles' mean density $< C >$ with excitation volume V is given by:

$$< C > = \frac{1}{2\sqrt{2}VG(0)} = \frac{2\sqrt{2}}{\pi\sqrt{\pi}\omega_0^2 z_0 G(0)} \quad 3.13$$

$$V = \frac{\pi\sqrt{\pi}\omega_0^2 z_0}{2^3} \quad 3.14$$

The average number of excited molecules can be found by

$$< N > = V < C > = \frac{1}{2\sqrt{2}G(0)} \quad 3.15$$

In presence of flow along with their diffusion, the ACF $G(\tau)$ changes to:

$$G(\tau) = \frac{G(0)}{(1+\frac{8D\tau}{\omega_0^2})\sqrt{1+\frac{8D\tau}{z_0^2}}} \exp\left(\frac{-(V_{flow}(\tau))^3}{\omega_0^2 z_0 (1+\frac{8D\tau}{\omega_0^2})\sqrt{1+\frac{8D\tau}{z_0^2}}}\right) \quad 3.16$$

3.2 DIFFERENTIAL DYNAMIC MICROSCOPY (DDM)

3.2.1 INTRODUCTION TO DDM

There has been always a problem of possible diffraction associated with optical systems, which limits resolving the particles smaller than the wavelength of light in simple microscopes. This technique, which was first developed by Cerbino and Trappe[138] in 2008, comes under near field scattering techniques and is very useful tool for studying biological and soft matter systems. This is basically based on analyzing the motion of particles in Fourier space that extracts useful information about their intensity fluctuation correlations. Here pixilated sensor (CCD camera) is used instead of the usual single sensor (photomultiplier tube), which makes the measurements of intensity variations at many different values of wave vectors simultaneously at a given time and at different time steps at a given wave vector[139]. In comparison to the laser light, a relatively large-diameter beam of light passes through the sample holder and then falls onto the camera, which measures the intensity fluctuations caused by the interference of beam and the scattered light[139]. Light scattered at certain angles results in providing the useful information at different wave vectors. Also, we do not need to track single particles individually, which is difficult if there is a lot of background noise.

The intensity correlation functions are analogous to the ones obtained by other spectroscopy techniques like dynamic light scattering, and x-ray photon correlation spectroscopy[22]. DDM can be performed using different microscopic methods such as bright field imaging, fluorescence,

confocal, and dark-field imaging. It is a very useful technique as it combines the advantages of other imaging and scattering techniques and it can overcome many shortcomings and limitations associated with them. Some of the advantages of DDM over other techniques are as follows[23]:

- It requires a very small volume of a sample.
- It works for the dilute to concentrated systems which can be heterogeneous spatially or dynamically, such as gels, glasses, etc.
- It can be applied to the samples, which give low signal or are dense optically.
- It is cost-effective as we can work with just a simple microscope, camera, and computer with some imaging software installed on it.
- DDM is an automatic statistical ensemble average method that does not require to track and analyze particles individually.

DDM is capable of generating a measurable signal from subdiffraction objects[139], for example, if we look at raw images of a colloidal suspension for 100 nm polystyrene particles, we can barely see any signal produced by the particles. But we can see a significant signal after subtracting two images taken at different times. Also as the time difference between two images increases, the signal in the difference image strengthens up[139]. We can observe this behavior by calculating the variance of the difference image at all time delays until the variance saturates.

Due to Brownian motion, the particles undergo rearrangement in space, which is the reason of the increased variance for the difference image but it saturates after long time intervals because the subtracted images become uncorrelated[139].

3.2.2 EXPERIMENTAL VARIATIONS FOR DDM

3.2.2.1 BRIGHTFIELD DDM

It is simple microscopic technique[140] that requires a normal setup (figure 3.2.2.1.1) consists of an illumination light source, halogen lamp in our case, fitted at the microscope stand, a condenser lens to focus the light onto the sample, objective lens to collect and magnify the light rays from the sample and a camera to view the sample's images.

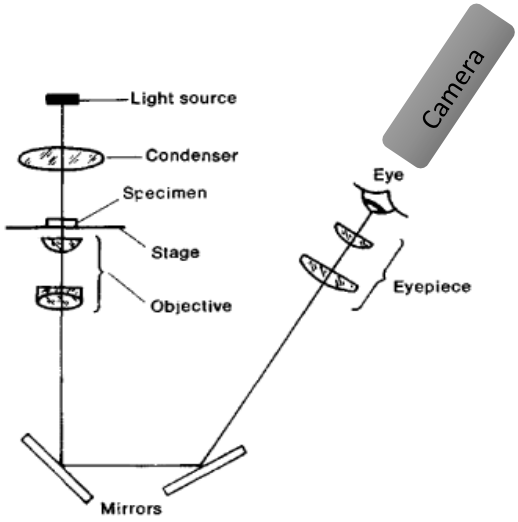

FIGURE 3.2.2.1.1: Ray diagram of bright field microscopy (source: Wikipedia)

3.2.2.2 FLUORESCENCE DDM

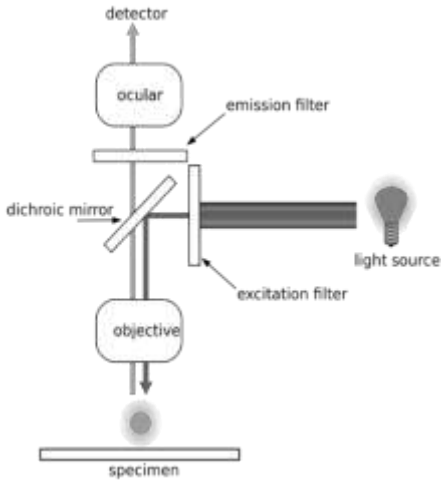

FIGURE 3.2.2.2.1: Set up for fluorescence microscopy (source: Wikipedia)

In this technique, a fluorescence microscope is used which uses fluorescence to generate an image of the sample under investigation. The sample is illuminated with a light source of a specific wavelength, which is absorbed by the fluorescent particles. As a result, light of longer wavelengths gets emitted[24]. The components of this setup (figure 3.2.2.2.1) include laser light, the excitation filter, a dichroic mirror, and the emission filter. Halogen lamps can't be used here because they can't provide intense and nearly-monochromatic light illumination[24].

3.2.2.3 CONFOCAL DDM

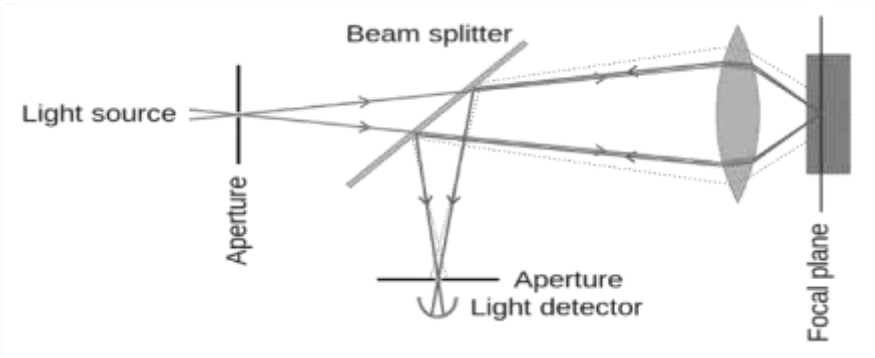

FIGURE 3.2.2.3.1: Principle of confocal microscopy (source: Wikipedia)

Confocal microscopy is also an optical imaging technique, which provides improved optical resolution and contrast of the image taken. It is done by placing a spatial pinhole at the confocal plane of the lens, which eliminates the light rays that are not in focus[24]. The path of light is shown in the figure 3.2.2.3.1. A confocal microscope can only see images at one depth at a time and able to acquire sets of images at different depths inside a thick sample.

3.2.3 DIFFERENTIAL DYNAMIC ALGORITHM (DDA)

A step by step description of DDA is given in figure 3.2.3.1. To start with, each image in this stack represents an intensity distribution which is denoted by I(x,y,t) at some time t. A

difference image signal $\Delta I(x,y,\Delta t)$ is calculated by subtracting one image from another for each image pair present in the stack. Then a fast Fourier transform $\Delta I(q_x,q_y,\Delta t)$ of each difference signal $\Delta I(x, y,\Delta t)$ is calculated, which gives us a Fourier distribution of intensity fluctuations. Now $\Delta I(q_x,q_y,\Delta t)$ is averaged over all image pairs giving us a 2-D ensemble average distribution $<\Delta I(q_x,q_y,\Delta t)>$. At the end, we find the image structure function $D(q_x,q_y,\Delta t)$, which can be calculated by finding the power spectrum of 2D Fourier distribution given by $<|\Delta I(q_x,q_y,\Delta t)|^2>$. Therefore, the radially averaged image structure $D(q,\Delta t)$ function[141] is given by:

$$D(q,\Delta t) = < |\Delta I(q,\Delta t)|^2 > \tag{3.17}$$

and the wave vector q is calculated by:

$$q = \sqrt{q_x^2 + q_y^2} \tag{3.18}$$

This whole process is repeated for all possible time steps in the image stack. This can be used for isotropic images. But it breaks down if there is directionality, such as flow.

Image structure function $D(q,\Delta t)$ for processes involving single relaxation with characteristic relaxation time[141] τ is fitted to the following equation:

$$D(q,\Delta t) = A(q)\left[1 - exp\left(\frac{-\Delta t}{\tau(q)}\right)\right] + B(q) \tag{3.19}$$

where, $A(q)$ and $B(q)$ are related to the imaging optics and imaging noise, respectively.

Finally, the diffusion coefficient D of particles can be found by fitting image structure function with different physical models. For example, for normal diffusion, τ vs. q can be best fitted with equation of straight line of slope *-2* as shown in the equation below[137]:

$$\tau(q) = \frac{1}{Dq^2} \qquad 3.20$$

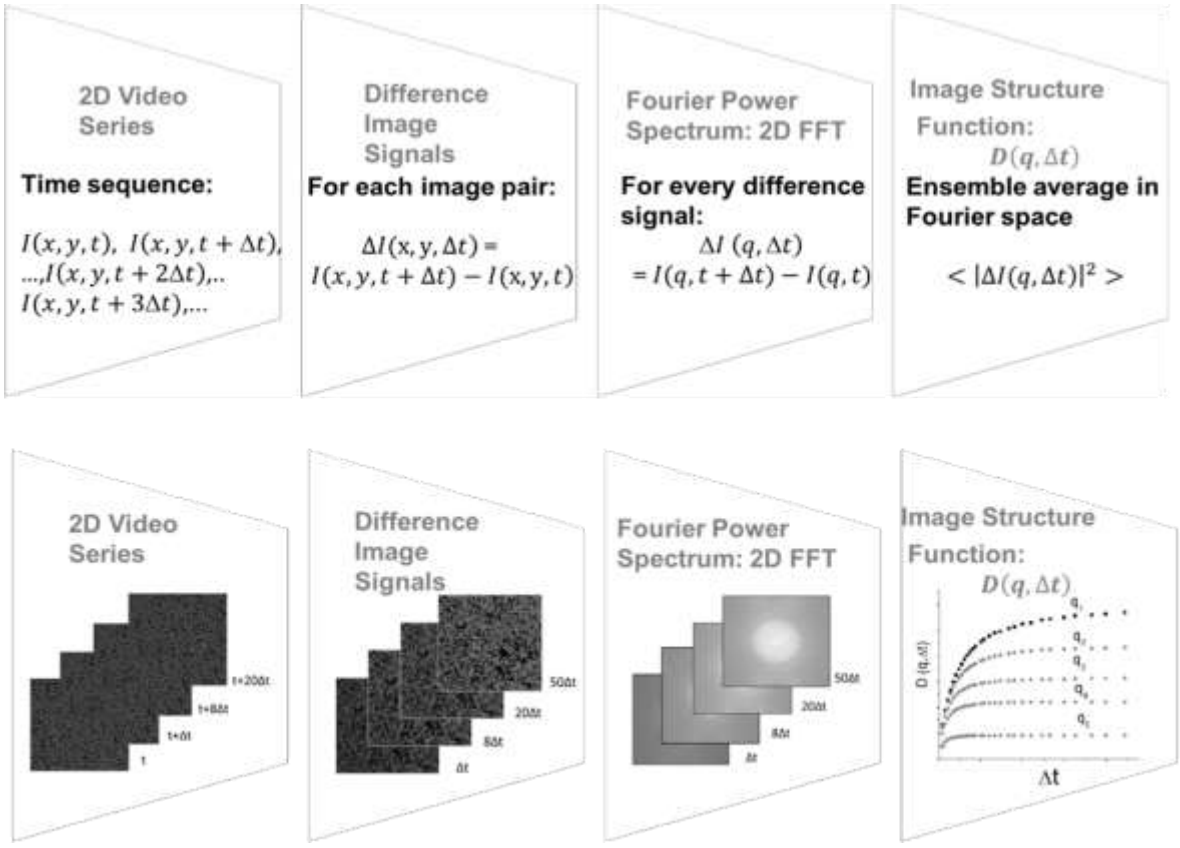

FIGURE 3.2.3.1: Steps involved in the analysis of DDM: Differential Dynamic Algorithm (DDA)

3.3 FALLING BALL VISCOMETER

A falling ball viscometer is a device to measure the viscosity of a fluid whose properties doesn't vary with time or flow conditions. This device's set up is shown in the figure 3.3.1 below: It is based on the Stokes' law which tells that a small spherical particle of radius r experiences a frictional force F while passing through in a viscous fluid of viscosity η with a velocity v which is given by:

$$F = 6\pi r\eta v \qquad 3.21$$

The fluid is kept stationary inside a cylindrical glass tube which is fixed at an angle of 80° to the ground. There is a water jacket surrounding the cylindrical tube, which is provided to keep a control on the temperature of the working sample. Firstly, the tube is filled with the polymer solution. Then one of the six available balls came with this device is chosen (looking at the test

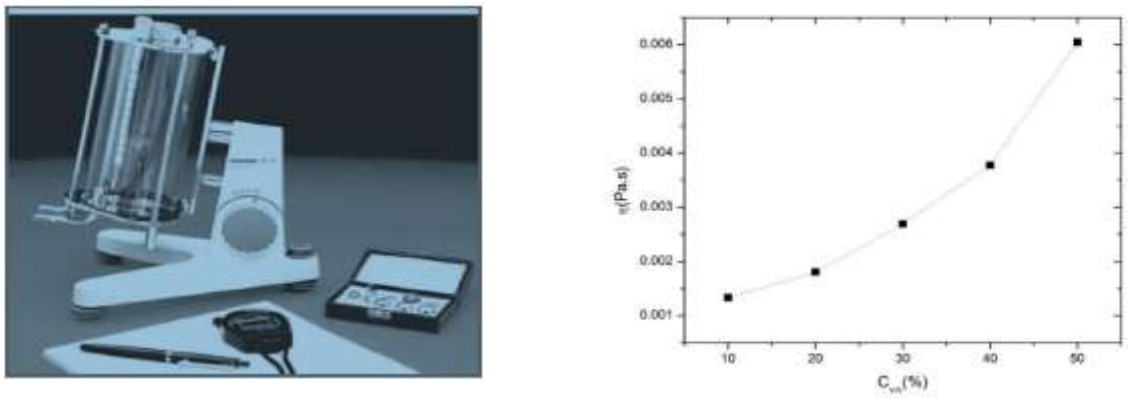

FIGURE 3.3.1: Left: falling ball viscometer, right: variation of viscosity with concentration of glycerol-water mixtures measured from falling ball viscometer.

certificate) and is released into the tube from the top. The six balls are with different diameters and densities which make this device capable of measuring a large range of viscosities (0.5 - 70000 mPa.s) of fluids. We need to keep an eye on the tube and motion of the falling ball and note the time it takes to travel the distance between the upper and the lower ring mark in the tube. This time of fall t of the ball is needed to calculate the viscosity of the fluid η, as shown as in the equation written below:

$$\eta = t(\rho_1 - \rho_2)B \qquad 3.22$$

where, ρ_1 and ρ_2 are the densities of the ball (according to the test certificate) and sample fluid respectively. B is the value of ball constant of the ball used, as given in the test certificate. All the measurements were taken at 20 ^{0}C for our experiments.

CHAPTER 4

DIFFUSION OF NANOPARTICLES WITHIN HIGHLY CONCENTRATED POLYMER SOLUTIONS

4.1 COMPARISON OF NANOPARTICLE DIFFUSION USING FLUORESCENCE CORRELATION SPECTROSCOPY AND DIFFERENTIAL DYNAMIC MICROSCOPY WITHIN CONCENTRATED POLYMER SOLUTIONS

The following material was originally published in Applied Physics Letters (2017)[142]

4.1.1 INTRODUCTION

The study of dynamics of nanoparticles (NPs) in polymer and biopolymer solutions is of great importance in many disciplines ranging from soft matter physics to drug delivery. For examples, the measurement of random Brownian motion of particles with different sizes in complex fluids can give information about the length-scale dependent viscoelastic properties. In the field of biophysics and drug delivery, the passive and active transport of macromolecules and nanoparticles can be understood by studying their motion in crowded heterogeneous environment full of obstacles. Fluorescence correlation spectroscopy (FCS) has been established as a useful method to study the Brownian motion of polymers[143,144], proteins[145], quantum dots[146], and nanoparticles[147] inside condensed matter systems. FCS uses a high numerical aperture (N.A.) objective to create a diffraction limited laser focus. The fluorescent molecules entering and leaving the open focal volume generate bursts of photons. Their concentration needs to be small, so that the number fluctuation is large according to Poisson statistics. This fluctuation in count is

correlated to obtain a curve, which after fitting with suitable model can give both the number of particles within the focal volume and diffusion coefficient (D) of the fluorescent molecules or particles. The translational diffusion coefficient[144,148], the rate of flow or chemical reactions[145,149], rotational diffusion for anisotropic particles[125,150], and internal motion of large macromolecules[151] can be studied with FCS. The fitting model of FCS assumes that particles are like a point source of light, i.e., their size is much smaller than the size of the laser focus (≈0.3 μm). Otherwise, one has to take into account the finite size effect in the fitting model, which necessarily complicates the analysis of the correlation functions. Therefore, majority of FCS experiments was done with particle size of less than 50 nm. Microscopy and scattering techniques are two other powerful methods. If the signal-to-noise ratio is large enough and if the assumption that particle is a spherical source of light holds, one can fit the intensity distribution with a Gaussian function and locate the position of the particles within 10-15 nm accuracy. The problem arises in systems with large background noise, such as in many polymer and biopolymer solutions, where particle tracking to determine the mean-square-displacement (MSD) may become prohibitively difficult. Scattering is a complementary method, which gives relaxation times (τ) of the system as a function of wave-vectors (q). The inverse of the wave-vector sets up a length-scale and the relaxation time corresponds to the dynamics at that length-scale. For standard dynamic light scattering (DLS) experiments, the length-scale is varied from a few tens to a few hundreds of nm by selection of different scattering angle. The problem with DLS is that unlike FCS, the method is not specific. So, in a mixture of particles and polymers, both contribute to the scattering and if they have dynamics occurring at similar time-scales, their separation at the intensity correlation

curve is not possible. The scattering techniques also require a different kind of set-up compared to FCS and microscopy methods[152].

Recently, Cerbino *et. al*. had developed a microscope based scattering technique[138,153], called differential dynamic microscopy (DDM), which can give wave-vector dependent relaxation times from real space images[153,154]. It is an automatic ensemble average method that does not require to track and analyze particles individually[152,153,155,156]. An advantage of DDM compared to some of its earlier variations of near-field scattering techniques[157] is that analysis is differential. As a result, background noise cancels out. Using brightfield, confocal, fluorescence, and dark-field microscopy[158], DDM had been used to study active motion of particles inside cell[159], fluctuations in non-equilibrium systems[160], and diffusion of nanoparticles[161,162]. A majority of DDM experiments used particles with diameter about 100 nm or higher.

We extend DDM to 50 nm length-scale, which is closer to the upper limit of particle size as used in FCS experiments. We used confocal microscopy[163] to collect movies of green fluorescent particles within a polymer solution. The particles were not clearly distinguishable from the noise in the images. With the same sample, we performed two-photon FCS experiments and compare the two measurements, which showed excellent agreement. Much celebrated Stokes-Einstein (SE) relation connects particle diffusivity to solution viscosity and particle size. But several recent studies-both experimental and theoretical-had shown that diffusion of nanoparticles in entangled polymer solutions or melts can be much faster compared to the expectation based upon bulk viscosity. Therefore, the traditional rheology measurements to predict the diffusion coefficient of NPs would fail in these systems. The results reported in this letter bridge the gap for FCS and

DDM experiments and extend DDM to study the rheological properties of complex fluids at few nanometer length-scales.

4.1.2 EXPERIMENTAL SECTION

Polyethylene oxide (PEO) of molecular weight, M_w = 600 kg/mol in the form of powder was purchased from Polymer Sources, Inc. and fluoresbrite carboxylate microspheres of 25 nm in radius were purchased from Polysciences, Inc. PEO was dissolved in deionized water to prepare two different volume fractions ϕ = 0.0069 and 0.02, nanoparticles were added in the solution, which was then heated and stirred at 30^{0}C. Two-photon FCS experiments were performed with a Ti:sapphire laser with wavelength of 800 nm and repetition frequency of 80 MHz. An oil objective (N.A. = 1.25, 100x) was used to focus the laser beam and the photon counts were recorded by two photomultiplier tubes after a 50-50 beam splitter. The autocorrelation functions (ACF) from these counts were obtained by using the ISS software (Urbana, IL). In figure 4.1.3.4, we showed ACFs of 25 nm particles diffusing in PEO-water solutions for two different volume fractions. The data fitting was performed by using the equation:

$$G(\tau) = \frac{G(0)}{1 + (\frac{8D\tau}{\omega_0^2}) \sqrt{1 + (\frac{8D\tau}{z_0^2})}} \qquad 4.1$$

where, D is the diffusion coefficient of the particles, $G(0)$ is the value of ACF at short time which is inversely proportional to the number of particles within the laser focus, ω_0 is the half-width, and z_0 is the half-height of the laser focus. For oil objective, the calibration using a well-known dye rhodamine 6G in water gave $\omega_0 \approx 0.39$ μm and $z_0 \approx 2$ μm.

For DDM experiments, first we validated our image acquisition and analysis by collecting brightfield movies of polybead polystyrene latex microspheres (Polysciences, Inc.) of diameters 100 nm, 200 nm, and 1 μm (Polysciences, Inc.) diffusing in neat water. The samples were loaded on 3″ × 1″ × 1.0 mm sized plain beveled edge microscope slides, which were covered with a cover glass on top with a double-sided scotch tape that acts as a spacer. The assembly was sealed at the edges to prevent evaporation. Brownian motion of the particles was captured using an air objective (N. A.=0.75, 60x) and a fast ccd camera (Jai corporation) with pixel size of of 0.15 μm. Video analysis was performed with a home-built Matlab based program. Briefly, difference image signal ΔI (x,y,Δt) was calculated by subtracting one image intensity distribution, I (x,y,t) from another I (x,y,t+Δt) for each image-pair present in the video. Assuming isotropy, the radially image structure function, $D(q,\Delta t) = < |\Delta I(q,\Delta t)|^2 >$ was obtained, where $|\Delta I(q,\Delta t)|$ is the Fourier transform of the difference signal. The image structure function[138] was fitted to the equation:

$$D(q,\Delta t) = A(q)[1 - g(q,\Delta t)] + B(q \qquad 4.2$$

where, $g(q,\Delta t) = exp\left(\frac{-\Delta t}{\tau(q)}\right)$ for processes involving single relaxation, $A(q)$ is the convolution of the particles scattering properties with the optical transfer function of the imaging optics, $B(q)$ is related to the imaging noise and incoherent scattering, and τ(q) is the wave-vector dependent relaxation time. For Brownian particles[138], the diffusion coefficient D can be found by fitting τ vs. q in log-log plot with an equation of straight line with slope -2:

$$\tau(q) = \frac{1}{Dq^2} \qquad 4.3$$

We expect such large particles diffusing in Newtonian fluids to have diffusion coefficient as predicted by Stokes-Einstein's equation:

$$D_{SE} = \frac{k_B T}{3\pi\eta d} \qquad 4.4$$

where, k_B is the Boltzmann constant, η is the solvent's viscosity, T is the absolute temperature and d is the hydrodynamic diameter of the particles.

4.1.3 RESULTS AND DISCUSSION

In figure 4.1.3.1, we plotted D as a function of inverse size of the particles. From the slope of the graph, we obtained the viscosity, η = 0.96 mPa.s, which matches very well with the viscosity of water at 23 ^{0}C (0.93 mPa.s). After verifying the method, we used DDM to study diffusion of relatively smaller nanoparticles, 25 nm in radius, within an aqueous viscoelastic polymer solution. About 500 video frames were recorded by using a confocal microscope (Nikon A1Rsi)

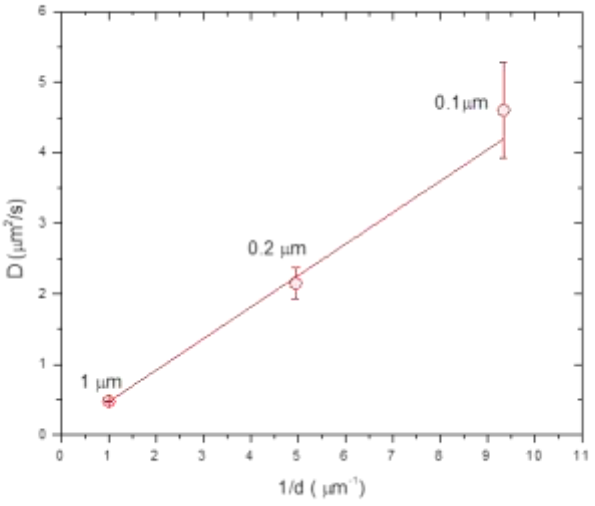

FIGURE 4.1.3.1: Diffusion coefficients as obtained through DDM are plotted as a function of inverse particle size (d). We obtained D for particles of diameter 100 nm, 200 nm and 1 μm within de-ionized water to be 4.60 ± 0.68 μm²/s, 2.15 ± 0.21 μm²/s, and 0.472 ± 0.001 μm²/s, respectively. The data showed D α 1/d.

equipped with an oil objective (N. A. =1.4, 100x) and a resonant scanner operating at 12 kHz. In figure 4.1.3.2, we showed the series of image structure functions for two different polymer

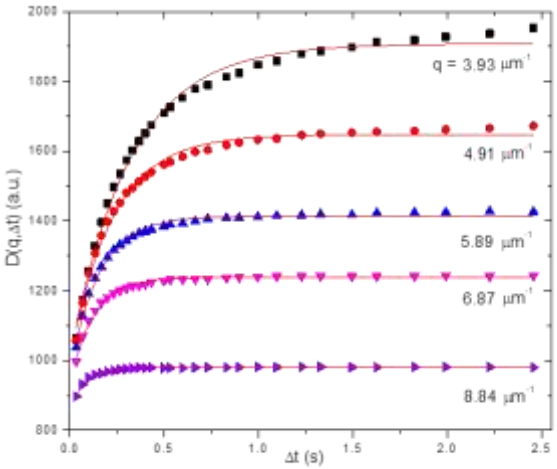

FIGURE 4.1.3.2: Image structure functions vs. time interval at six different values of wave-vectors for the nanoparticles within PEO solutions at volume fraction, ϕ = 0.0069. The solid lines correspond to the fittings of image structure function with Eq. 4.2 assuming a single exponential relaxation. The corresponding q-values were shown. The images were collected by a confocal microscope.

volume fractions in water. The curves are well fitted with a single relaxation time. The q-dependence of the relaxation time as determined by DDM is shown in figure 4.1.3.3 and as the fittings showed that the relaxation times decay as q^{-2} as predicted for normal Brownian motion.

For normal diffusion, mean-square-displacement (MSD) scales with time. The corresponding length-scale associated with the wave-vector ranges from 0.6 μm to 1.5 μm. This is similar to the length-scale probed in FCS expeiments, $2\omega_0 \approx 0.8$ μm. From the slopes of the graphs we determined diffusion coefficient, D of the particles in PEO samples with volume fractions, ϕ = 0.0069 and 0.02 to be 0.19 ± 0.047 μm²/s and 0.029 ± 0.001 μm²/s, respectively. These match very well with FCS results. We calculated some of the important length-scales of the system[71] (table 4.1.3.1). Water is a good solvent for PEO and it assumes a swollen random walk conformation. The radius of gyration, R_g is related to the molecular weight (M_w) according to:

$R_g=0.02(M_w)^{058}$ nm. The radius of gyration R_g for 600K PEO in water is found to be ≈ 45 nm. This is for dilute solution. As the polymer concentration increases, R_g decreases as $\phi^{-1/8}$, where ϕ is the

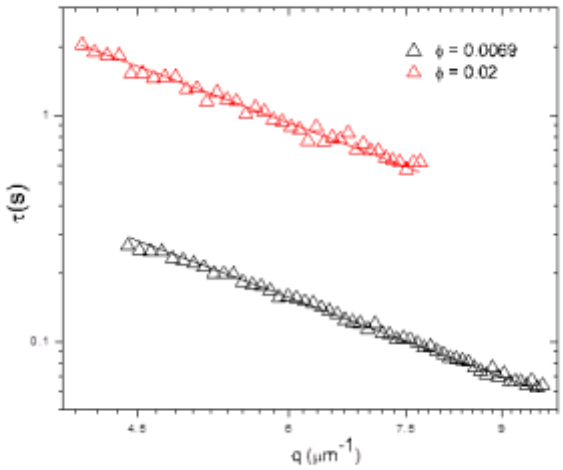

FIGURE 4.1.3.3: The decay times (τ) as obtained from fittings in Figure 4.3.2 are plotted against the wave-vectors (q) for both samples of PEO. Circles: ϕ=0.0069, Squares: ϕ=0.02. The solid line is the fit assuming a normal Brownian diffusion according to Eq. 4.3. D obtained from DDM matched within 1% of the values obtained from FCS. (Inset) Diffusion coefficient (in $\mu m^2/s$) is plotted as a function of PEO volume fraction in log-log plot. The straight line has a slope of -1.52 as expected from theory for particles with size greater than the correlation length but smaller compared to tube diameter.

polymer volume fraction. The overlap concentration denotes the transition from dilute to semidilute regime, where the chains begin to interact. It is given by a well-known relation: $\phi^* = M_w/(4/3*\rho*\pi*R_g^3*N_A)$, where ϕ^* is the overlap volume fraction, ρ is the density of polymer, and N_A is the Avogadro number. We determined the overlap volume fraction ϕ^*= 0.0024. The entanglement concentration of PEO is given as: $\phi_e=M_e/M_w$, which is ≈0.0033 for the polymer used (M_e = 2 kg/mol for PEO). Our experiments were performed slightly above the semidilute solution and in the entanglement regime[63,164]. The correlation length (ξ) is the most important length-scale in semidilute solution, which scales with polymer concentration according to: $\xi(\phi)\approx R_g\,(\phi/\phi^*)^{-0.76}$. We determined, ξ ≈ 20 nm and 9 nm for polymer volume fractions, ϕ=0.0069 and 0.02, respectively. So, for our experiments, polymer size > particle size > correlation length. The tube

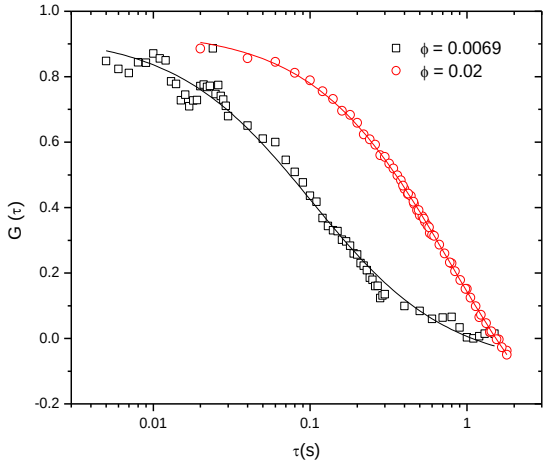

FIGURE 4.1.3.5: Diffusion coefficients D as obtained through DDM and FCS are plotted as a function of PEO concentrations. We obtained good agreement of D within uncertainties in both the concentrations using DDM and FCS demonstrating normal diffusion.

diameter in the concentrated entangled polymer solution is given as: $a(\phi)=a(1)\phi^{-0.76}$, where a(1) is the tube diameter in the melt and a(1)= 4 nm for PEO. The tube diameter is 78 nm for polymer volume fraction, ϕ=0.02. The scaling theory of particle mobility in polymer solution[57] had identified several regimes of diffusion depending upon particle size. Two cross-over volume

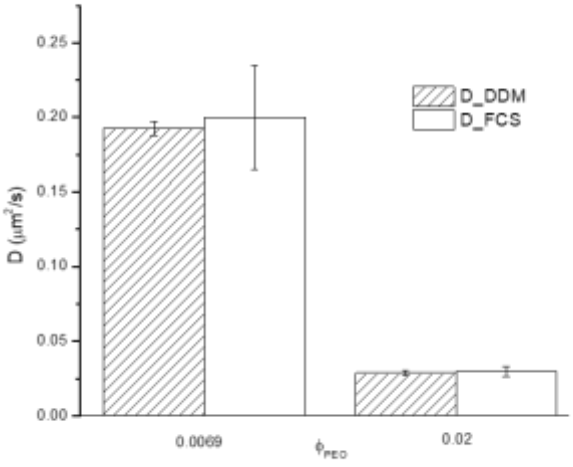

FIGURE 4.1.3.4: FCS autocorrelation functions for 25 nm radius green fluorescent nanoparticles diffusing within entangled PEO solutions for two different polymer volume fractions. The fitting of the curves is according to Eq. 4.1 as given in the text. The diffusion coefficients obtained from fittings are 0.19 ± 0.007 $\mu m^2/s$ for ϕ=0.0069 and 0.030± 0.001 $\mu m^2/s$ for ϕ=0.02, respectively.

fractions are of significance for our experiments, $\phi^{\xi} \approx \phi^*(R_g/d)^{1.32}$ and $\phi^a \approx \phi^*(d/a(1))^{-1.32}$, determined ≈0.0021 and ≈0.035, respectively. Therefore, our experiments were performed in the range of volume fraction, where $\phi^{\xi} < \phi < \phi^a$. In this intermediate size regime, the particle motion is affected by the segmental dynamics of chains[63]. They do not feel the bulk viscosity as measured by a rheometer, but a much smaller nanoviscosity. The effective viscosity scales as, $\eta_{eff} \sim \eta_s(d/\xi)^2$, where η_s is the solvent viscosity. As $\xi \sim \phi^{-0.76}$, the particle diffusion coefficient is expected to scale as, $D \sim \phi^{-1.52}$. As shown in figure 4.1.3.6, our measurements are in good agreement with this prediction.

In conclusion, we compare results of two different experimental methods, fluctuation

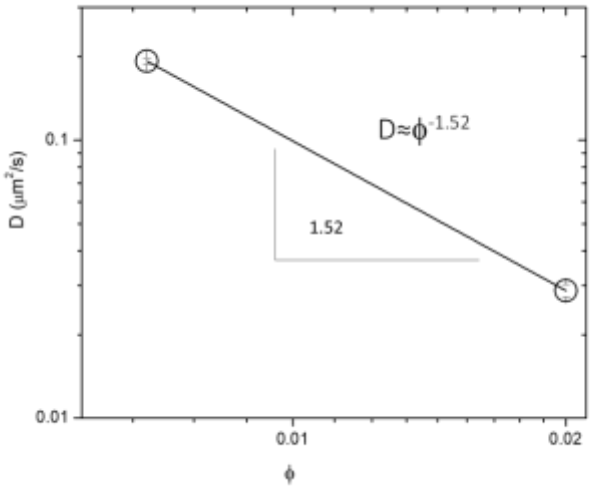

FIGURE 4.1.3.6: Diffusion coefficient (in μm²/s) is plotted as a function of PEO volume fraction in log-log plot. The straight line has a slope of -1.52 as expected from theory for particles with size greater than the correlation length but smaller compared to tube diameter.

correlation spectroscopy and differential dynamic microscopy to study nanoparticle diffusion within concentrated polymer solution. The measured diffusion coefficients are in good agreement with each other and both showed normal diffusion. The volume fraction dependence of diffusion coefficients can be explained with scaling theory. The results demonstrated that DDM can be

extended at sub 100 nm size range of the particles to measure length-scale dependent rheology of complex fluids.

TABLE 4.1.3.1: Important Parameters for PEO

Molecular weight, M_w	600 kg/mol
Radius of Gyration, $R_g = 0.02\ M_w^{0.58}$ (nm)	44.91
Volume fraction, ϕ range	0.0069 - 0.02
Overlap volume fraction $\phi^* = M_w/(4/3 * \rho * \pi * R^3 * N)$ ($\rho_{PEO} = 1.126$ g/ml);	0.0023
Entanglement concentration $\phi_e = M_e/M_w$ ($M_e = 2$ kg/mol for PEO)	0.0033
Correlation Length, $\xi(\phi) \approx R_g\ (\phi/\phi^*)^{-0.76}$ (nm)	3.75 – 8.8
Tube diameter $a(\phi) \approx a(1)\ \phi^{-0.76}$ (nm) $a(1) = 4$ nm, $\phi = 0.02$	78.21

CHAPTER 5

DYNAMICS AND MELTING OF COLLOIDAL STRUCTURES FORMED ON TOP OF CURVED SURFACES

5.1 INTRODUCTION

Study of the dynamical and structural properties of 2D crystals formed on curved surfaces is very important in the fields of drug delivery[165], engineering[166,167] and biophysics[168,169]. There has been a lot of interest in studying the structure and dynamics of particle configurations on curved surfaces[12,16,17,170,171] since Thomson's problem[171] of charged particles interacting through Coulomb potential in spherical shell. Most of the work in this field focused on how the packing of particles on curved surfaces differs from self-assembly on the flat surfaces[172]. Bausch *et. al.* presented the experimental realization of two dimensional self-assembly of colloids on spherical water droplets using optical microscopy[165]. They marked the presence of stable defects called as grain boundary scars induced by disclinations due to the curvature.

The most well-known Kosterlitz Thouless Halperin Nelson Young (KTHNY) theory[173] of phase transitions in 2D was developed in the 1970s. This theory states that two-dimensional systems exhibit an intermediate phase i.e. hexatic between an ordered crystal and a disordered liquid state. These three states can be distinguished by the arrangement of atoms in the system at the macroscopic scale. For a crystalline state, two kinds of orders are present i.e. translational and orientational. The hexatic phase is an ordered phase too but without translational order. It is generally characterized by six-fold orientational order while liquids do not have any sort of periodic ordering. According to KTHNY theory[174], 2D melting takes place in two stages and there

is a continuous phase transition from solid to hexatic and hexatic to liquid state. In 1979, the phase transition from liquid to crystalline state of electrons on a liquid-He surface was first studied[175].

Inside a crowded environment of particles, de Gennes narrowing (DGN) is marked by the slowing down of system dynamics as a result of strong spatial correlations between the nearest neighboring particles[9]. DGN is characterized by peaks in structural and dynamical curves. Hong *et. al.* used neutron scattering to describe the relative motion of proteins and found that wave vector dependence of the interdomain diffusion is inversely proportional to the probability distribution of spatial configurations, given by the structure factor[10]. This means that a highly populated configuration fluctuates slower than a less populated configuration.

Optical microscopic methods help in experimental observation and validation of this phenomenon. We used a recently developed microscopy based scattering technique i.e. differential dynamic microscopy (DDM) which was first used to quantify the motion of colloidal particles in the reciprocal space[138]. It gained lot of interest[138,153-156,158,160,163] among many fields because it is very cost effective and easy to use experimental technique. DDM gives wave dependent relaxation times from acquired real space image stacks. This method is faster and easier than other available light scattering and particle tracking techniques. It provides dynamical information of the system without the need of individual particles being tracked and resolved as it performs an automatic ensemble averaging during the analysis. Other light scattering methods require a coherent source of light but DDM works well even with an ordinary white light microscope. DDM analysis is based on analyzing differential image signals making it uniquely

advantageous over other scattering techniques as it cancels out any background noise. DDM has been used in many variations such as brightfield, dark-field, fluorescence and confocal microscopy to study bulk motility of E. coli[155], wave vector dependence of highly concentrated systems[176], non- equilibrium system fluctuations[177-179] and diffusion of spherical[138] and asymmetric[155] nano and microparticles.

5.2 EXPERIMENTAL SECTION

Colloidal discs were prepared starting from 1 μm diameter fluorescently labelled polystyrene (PS) spheres. The method was similar to the preparation method of ellipsoidal

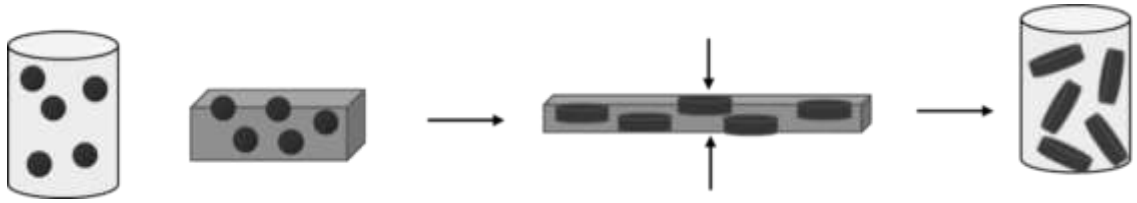

FIGURE 5.2.1: Schematic of discoids' preparation method from PS spheres with two-step batch processing method.

polystyrene particles given by Ho and co-authors[180] (figure 5.2.1). The spheres were embedded in an elastomeric film of poly(dimethyl siloxane) (PDMS). This material is clamped, heated above the glass transition temperature of the matrix (≈150 ^{0}C), and then a uniaxial compression is used between two flat plates. The aspect ratio, κ=b/a, where a is the diameter and b is the thickness of the disc depends on the amount of strain. We determined by using analysis of confocal microscopy images that that a≈1.3 μm and by using conservation of volume we determined, b≈0.6 μm, which gives the aspect ratio ≈0.77. The discoids were then suspended in deionized water, centrifuged several times to recover the particles, and rinsed with deionized water several times. To obtain dry particles, the sample was kept inside a heated oven for at least 24 hours. For solvent, we used a critical mixture of 2, 6 lutidine + H_2O + D_2O (LDW) at a volume fraction ratio of 0.3:

0.14: 0.56. The critical temperature of lutidine + water (LW) mixture at the critical volume fraction of 30% lutidine is ≈34 ^{0}C. The addition of heavy water lowers the critical temperature, which at our composition was determined to be 30 ^{0}C. Both LW and LDW samples have a lower critical solution temperature (LCST). The sample is a homogeneous mixture at the room temperature (23 ^{0}C), which phase separates upon heating. The liquid composition used in our experiments has a density very close to the density of PS (1.05 g/cm^3). This reduces the sedimentation rate of the particles significantly. The volume fraction of the particles (φ) in the sample was kept at less than 0.01, which causes minimal shift in the phase transition temperature.

About 10 μl volume of the critical mixture containing the particles was placed at the center of a microscope cover slip. We used an imaging spacer (Grace Biolabs) of thickness ~100 μm to confine the specimen between two coverslips. A precision thermistor (YSI 44034) is placed on the top of the sample cell by using a conductive adhesive to measure the temperature. The set-up is placed inside a custom-made thermostat, whose temperature is regulated by a proportional-integral-derivative (PID) controller (Lakeshore, Inc.). A separate but closely matched thermistor was used for the controller. We have shown previously that with this design we can achieve temperature stability of a few mK for few hours. We placed the whole assembly on the top of a confocal microscope, which is integrated with an incubator. The incubator acts as a heat sink, whose temperature can be controlled by 0.2 ^{0}C. All confocal images were captured by using an

inverted Nikon A1Rsi equipped with a resonant scanner head operating at 12 kHz. Sample videos were acquired using an air objective (N. A.=1.4, 100x) and a fast ccd camera at a frame rate of ~30.

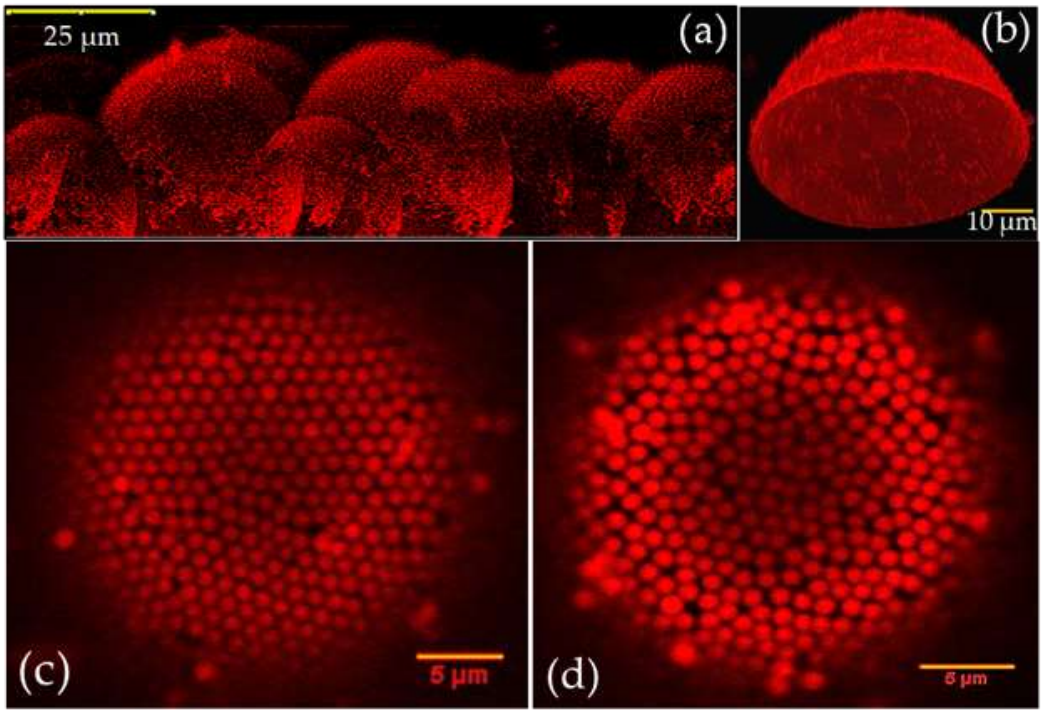

FIGURE 5.2.2: At critical temperature, many dome-like droplets of different sizes (a) are formed inside the water-lutidine colloidal sample. A 3D view of one of the droplets is shown in (b). We focused on two dimensional structures formed on the top of these domes. Discoids are seen to have arranged themselves into ordered crystal-like structures at the interfaces as shown in (c). As the temperature is slightly increased, these crystals seem to have melt and form hexatic structures as predicted by KTHNY 2D melting theory. We observed crystal structures with lowering the temperature back indicating a reconfigurable melting and freezing of colloidal assembly.

We approached the phase transition temperature (T_x) in small steps of temperature increments starting from the room temperature. Initially, temperature was changed by a degree followed by waiting of 20 minutes. Once the sample temperature reaches within 1 ^{0}C of T_x, increment of temperature was reduced to 0.1 ^{0}C, and then even slower as the phase transition temperature was approached. We observed formation of colloidal domes as we cross the binodal curve and enter the two-phase region of the liquid. The domes of different sizes, from 10 μm to

250 μm appears (figure 5.2.1). These domes are lutidine droplets in water, where the particles spontaneously accumulate at the interface. At present, it is not clear what drives the particles at the interface. It is possible that particles are neutrally wetted due to the preparation method involved. The formation and melting of the domes are completely reversible, which can be controlled by a change of temperature.

We started with a dense liquid of micron sized polystyrene latex microspheres (Polysciences, Inc.) (figure 5.2.2) for validating our experimental and analysis method using DDM. 2D self-assembled structures were formed on top of droplets of microdiscoids dispersed in 2,6 lutidine water solutions in the concentrated regime.

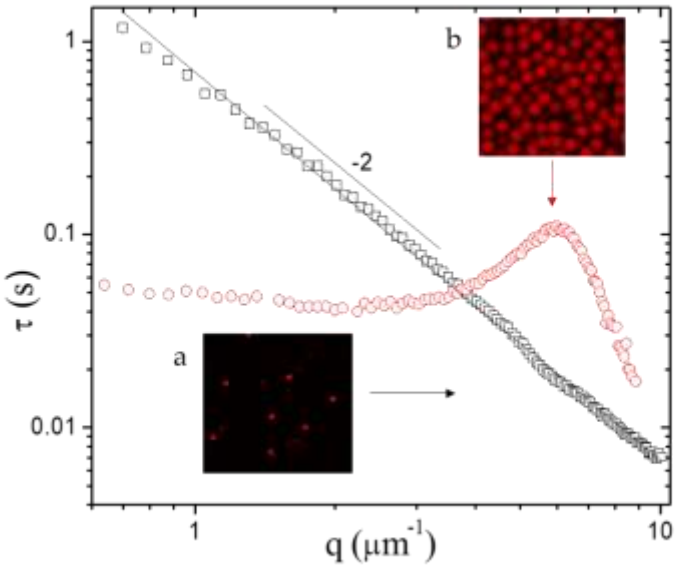

FIGURE 5.2.3: The decay times (τ) as obtained from fittings of image structure functions are plotted against the wave-vectors (q) for dilute (a) and crowded (b) concentration regimes of microspheres. As a contrary to the straight-line behavior in dilute conc., we observed a characteristic peak in decay time at q= 6.17 μm^{-1} in the concentrated regime (vol. fraction, ϕ=0.4) of particles. We calculated $r = \frac{2\pi}{q}$ = 1.02 μm and pair correlation function g(r) also has a peak at a matching r. This is an indication of de-Gennes narrowing i.e. slowing down of dynamics at characteristic length scales due to confined motion in crowded surroundings.

5.3 RESULTS AND DISCUSSION:

de Gennes narrowing has been studied during melting of dense crystal-like structures using differential dynamic microscopy (DDM). Using a home-built Matlab DDM analysis code, first we calculated the differential intensity image signals ΔI (x,y,Δt) by subtracting spatial intensity signals I (x,y,t) at a time t from I (x,y,t+Δt) at another time t+Δt for all image pairs at every possible value of delay times in the acquired video. Then a radial averaging was performed

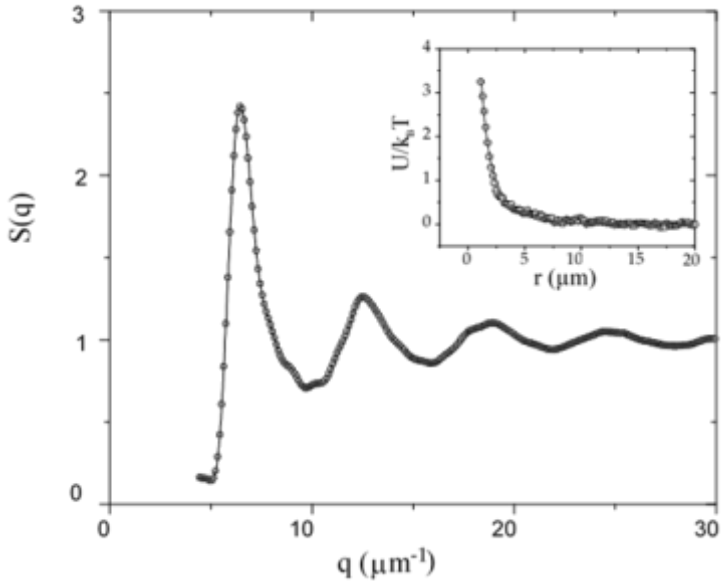

FIGURE 5.3.1: Main: Structure factor curve for the concentrated samples of microspheres. We observe characteristic peaks in the structure factor at distinct wave vectors. The first peak in S(q) vs. q curve has a maximum value at $q = q_{max} \approx 6.5\ \mu m^{-1}$. Such characteristic peaks in the structure factors are an indication of existence of long-lived and low free energy states. S(q) fits very well with Percus-Yevick analytical solution of Ornstein-Zernike equation for hard spheres. **Inset**: Particles experience hard sphere potential.

on difference image stacks to calculate the so-called image structure function, $D(q, \Delta t) = < |\Delta I(q, \Delta t)|^2 >$, where $|\Delta I(q, \Delta t)|$ is the Fourier transform of the difference signal. The image structure function was fitted to the equation:

$$D(q,\Delta t) = A(q)[1 - g(q,\Delta t)] + B(q) \qquad 5.1$$

where, $g(q,\Delta t) = exp\left(\frac{-\Delta t}{\tau(q)}\right)$ for processes involving single relaxation, $A(q)$ is the convolution of the particles scattering properties with the optical transfer function of the imaging optics, $B(q)$ is related to the imaging noise and incoherent scattering, and τ(q) is the wave-vector dependent relaxation time. Firstly, using DDM, we found that for the dense concentration (volume fraction,

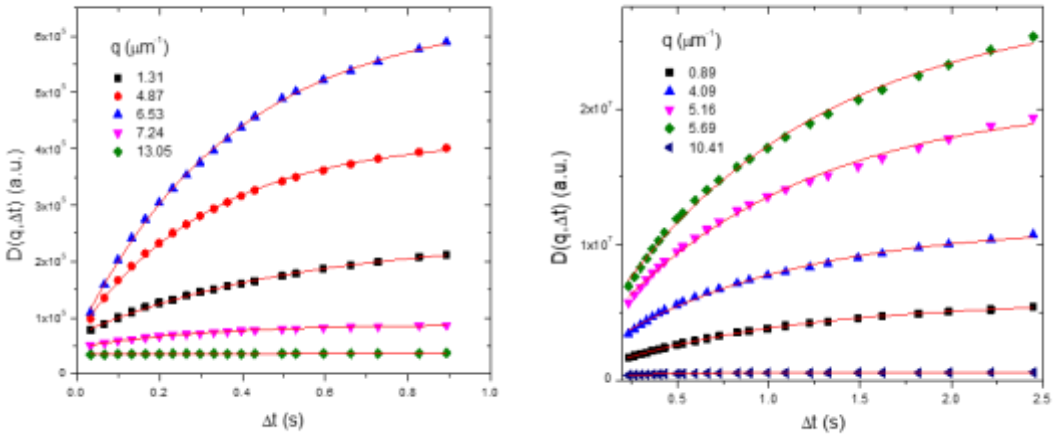

FIGURE 5.3.2: Image structure functions vs. time interval as obtained through DDM at five different values of wave-vectors for the discoids in water-lutidine samples. The solid lines correspond to the fittings of image structure function with Eq. 5.1 assuming a single exponential relaxation. The corresponding q-values were shown. Left graph is for crystalline state and right graph is for melted state of discoids and the images were collected by a confocal microscope.

ϕ=0.4) of microspheres decay time τ has a characteristic peak at a q value of 6.17 μm^{-1} that matches with the first peak in structure factor $q_{max} \approx 6.5$ μm^{-1} (figure 5.3.1: main) These matching peaks relates the structure and dynamics of these dense solutions. After validating our experimental system and data analysis in characterizing the dynamics of dense aqueous solutions of microspheres, we studied the dynamics of anisotropic particles i.e. microdiscoids inside a complex medium i.e. a critical mixture of water-lutidine as described in the experimental section above. We observed two-dimensional melting of the ordered structures formed by microdiscoids

on top of the curved surfaces. The dynamics of both phases, i.e. crystal-like and phase after melting called as hexatic was further analyzed in reciprocal space using DDM. Image structure functions are shown in figure 5.3.2 for both phases.

From microscopy data, we calculated important structural and dynamical correlation functions for both crystal and hexatic phases in the real and reciprocal space. We observed six-fold patterns like in a honeycomb in the crystal phase with a few five-fold and seven-fold defects.

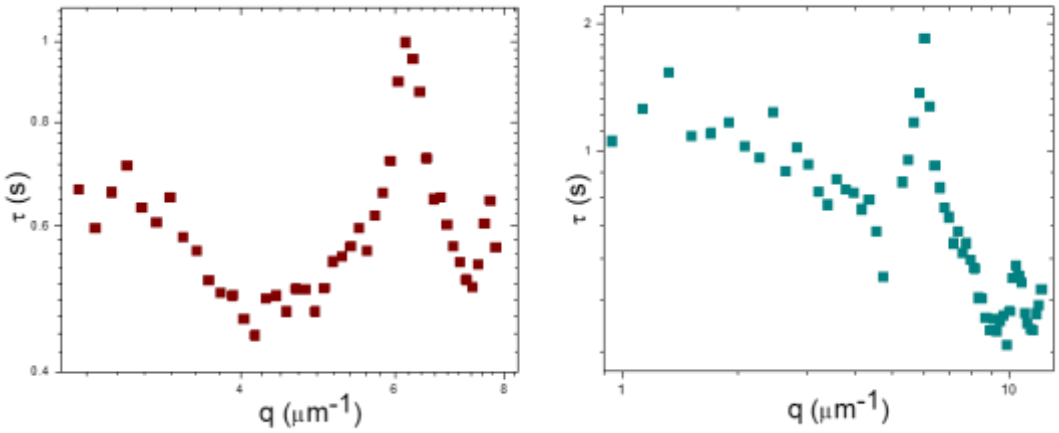

FIGURE 5.3.3: The decay times (τ) as obtained from fittings in Figure 5.3.2 are plotted against the wave-vectors (q) for crystal-like state of the discoids observed in water lutidine samples. We observed a characteristic peak in decay time at q= 6.17 μm^{-1}. We calculated $r = \frac{2\pi}{q}$= 1.02 μm and the radial distribution function g(r) also has a peak at a matching r . This is an observation of de-Gennes narrowing.

During the phase transition to a melting phase, we observed the appearance of many-fold defects and loss of long-range order. Using DDM, we got the dynamical information of this system in a high range of wave vector values as shown in figure 5.3.3, decay time, τ has a peak at q= 6.17 μm^{-1} and q= 5.54 μm^{-1} in the crystal-like and the melted hexatic phase with corresponding distances in the real space calculated as $r = \frac{2\pi}{q}$ = 1.02 μm and 1.13 μm (figure 5.3.3). We have also computed

the nearest neighbor particle distance distributions from direct microscopy data and the values came out to be 1.17 ± 0.14 μm and 1.23 ± 0.21 μm for crystal-like and melted phase respectively.

To determine pair interactions, we computed the pair correlation function $g(r)$ of the particles in both phases i.e. crystal and hexatic as shown in figure 5.3.4. We observe characteristic peaks in radial distribution functions. Such peaks in $g(r)$ curves correspond to first, second and

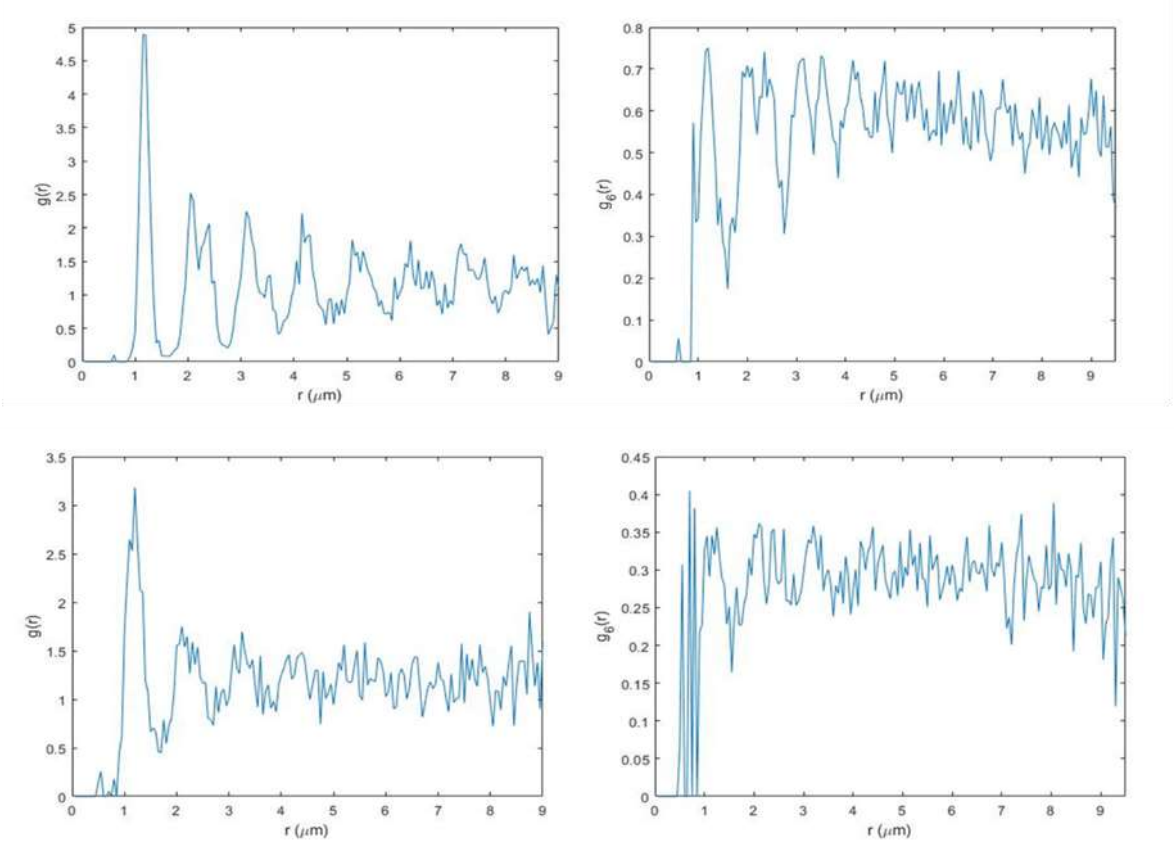

FIGURE 5.3.4: Pair correlation functions and orientational correlation functions for crystal (top left and right) and hexatic phase (bottom left and right) respectively.

third neighbor distances, etc. In crystal, we see a characteristic splitting of peaks after the first one. At large distances, the peaks disappear and $g(r) \to 1$. The pair correlation function $g(r)$ has their first peaks with maximum values at r = 1.13 μm and 1.15 μm for crystal-like and hexatic phase respectively that matches very well with the peaks obtained from DDM. Such characteristic

peaks indicate the presence of DGN. To take account of orientational correlations and local crystallinity, we calculated the bond orientational correlation functions $g_6(r)$ and sixfold bond-orientational order parameter ψ_6 defined by:

$$g_6(r) = < \psi_6^*(0)\, \psi_6(\vec{r}) > \qquad 5.2$$

$$\psi_6(r_i) = \frac{1}{n}\sum_{j=1}^{n} \exp[i6\Theta(r_{ij})] \qquad 5.3$$

where, n= number of nearest neighbors and $\Theta(r_{ij})$: angle betweeen the vector connecting the central particle, i, with neighboring particles, j, and a fixed reference axis.

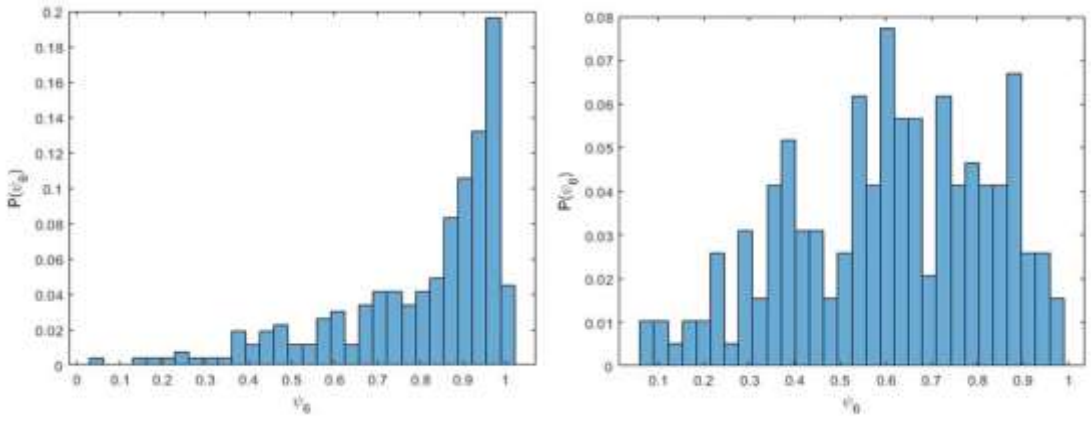

FIGURE 5.3.5: Probability distribution for local bond orientational order parameters. For a perfect crystal with all lattice sites having exactly six neighboring particles, it peaks at 1. For hexatic and liquid phases, the peak shifts to lower values of local bond orientational order parameter.

The bond-orientational order parameter ψ_6 is calculated by finding the average of the absolute value of $\psi_6(r_i)$ and it should be 1 for a perfect hexagonally packed crystal and any value less than 1 is considered as a phase with lost local hexagonal order. The values close to zero indicates a highly disordered liquid state. ψ_6 has values of ~0.8021 and ~0.6046 for the solid and melted phase in our experiments. The probability distributions of $\psi_6(r_i)$ are plotted for both phases (figure 5.3.5). It can be seen that the probability of many-fold defects is increasing as the

phase takes a transition from the crystal to hexatic but it still has a small range orientational ordering of six-fold. The bond orientational correlation function $g_6(r)$ for crystal-like phase approaches towards a constant value whereas it should decay algebraically for hexatic phase at longer times. Using Voronoi construction and Delaunay triangulation methods, we have constructed and combined different many-fold lattice sites inside the two phases as shown in figure 5.3.6.

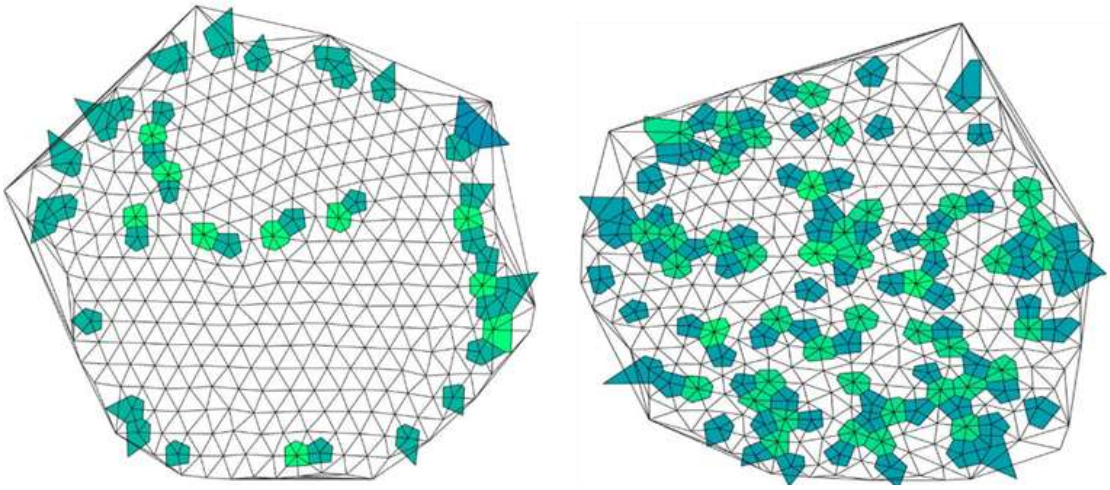

FIGURE 5.3.6: Structural rearrangements of colloids from crystal phase (left) to hexatic phase (right) during 2D melting can be characterized by Voronoi construction and Delaunay triangulation method. Both Delaunay triangulation and Voronoi construction is shown in above figure for both the phases. Delaunay triangulation was performed on the digitized positions of discoids for both the crystal and hexatic phase. Voronoi construction is only shown for lattice sites with nearest neighbors less or more than six in different highlighted colors. They also represent lattice defect within the ordered phases. As the transition occurs from crystal-like to hexatic phase, there is a visible loss of long-range ordering and the number of lattice defects are also increasing. This is a clear indication of melting.

In this study, we understand the dynamics and 2D melting of microdiscoids on a curved surface using differential dynamic microscopy (DDM). In reciprocal space, the self-assembled ordered structures made of discoids on the top of dome like surfaces show characteristic peaks in relaxation time vs. wave vector curves indicating slow dynamics. Peaks in the pair correlation

curves at matching length scales demonstrate de Gennes narrowing phenomena. We observe an intermediate hexatic phase during the melting of these structures as predicted by KTHNY theory of 2D melting.

CHAPTER 6

TRANSLATIONAL AND ROTATIONAL DIFFUSION OF ANISOTROPIC COLLOIDS

6.1 A QUICK METHOD TO DETERMINE ROTO-TRANSLATIONAL DIFFUSION OF MICROELLIPSOIDS IN AQUEOUS MEDIA

6.1.1 INTRODUCTION

Study of translational and rotational dynamics of anisotropic colloids is very important as it has many applications in the field of energy field materials[181] and medicine[182]. In contrast to the isotropic spherical particles, experimental methods available for characterizing dynamics of anisotropic colloids is limited. Experimental methods such as dynamic light scattering, confocal laser scanning microscopy, fluorescence correlation spectroscopy and fluorescence recovery after photobleaching have contributed to understanding of motion of rods[126,150,183-185]. Most of these techniques require a sophisticated source of light and the associated data analysis can be time-consuming and tedious such as in particle tracking.

We report a quick method i.e. differential dynamic microscopy (DDM) to determine ensemble averaged translational and rotational diffusion coefficients of anisotropic particles in aqueous media. DDM provides the dynamical information of particles in the reciprocal space using a broad range of video microscopic techniques[138,153-156,158,160,163,186]. In reciprocal space, we have the advantage of extracting dynamical information in the form of characteristic time scales for a huge range of wave vectors. Initially, we implemented DDM in our research for quantifying the diffusion of spherical nanoparticles[142]. Here, we extend DDM for studying the combined effect

of roto-translational diffusion on micron sized rods/ellipsoids (microellipsoids) within aqueous media. We studied the rotational and translational diffusion of microellipsoids both on a 2D surface and in bulk. We used confocal microscopy as a microscopy platform to study the diffusion of fluorescent poly(dimethyl methacrylate) microellipsoids (aspect ratio ≈ 2.67 μm /0.95 μm ≈2.81) in aqueous media. The microellipsoids are dispersed in deionized water at a dilute concentration so that they can move freely in a Brownian diffusion. Translational and rotational diffusion coefficients are determined from the wave vector q dependence of ensemble averaged dynamics at different time scales. Through this research, we assess the scope to apply a modern and unique combination of video based light microscopy and scattering principles for characterizing the translational and rotational dynamics of anisotropic colloids.

6.1.2 EXPERIMENTAL SECTION:

Microellipsoids were synthesized from 1 μm diameter fluorescently labelled polystyrene (PS) spheres[180] (figure 6.1.2.1). The spheres were embedded in an elastomeric film of poly(dimethyl siloxane) (PDMS). This material is clamped, heated above the glass transition temperature of the matrix (≈150 ^{0}C), and then a uniaxial deformation was carried out with by

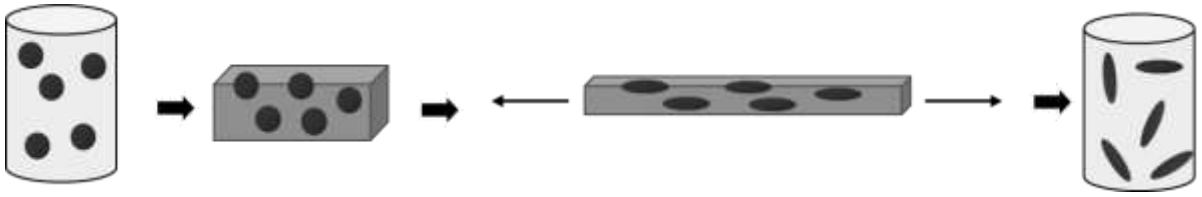

FIGURE 6.1.2.1: Schematic of microellipsoids' preparation from PS spheres using two-batch processing method

continuous stretching. The aspect ratio, $r = \frac{a}{b}$, where $2a$ is the length and $2b$ is the thickness of the disc depends on the amount of strain.

Using analysis of confocal microscopy images, we determined that a≈0.95 μm and b≈2.67 μm, which gives the aspect ratio ≈2.81. The microellipsoids were then suspended in deionized water at a volume fraction of less than 0.01. About 10 μl of the sample volumes were loaded on 3″ × 1″ × 1.0 mm sized plain beveled edge microscope slides, which were covered with a thin cover glass on top with a double-sided scotch tape that acts as a spacer. The assembly was sealed

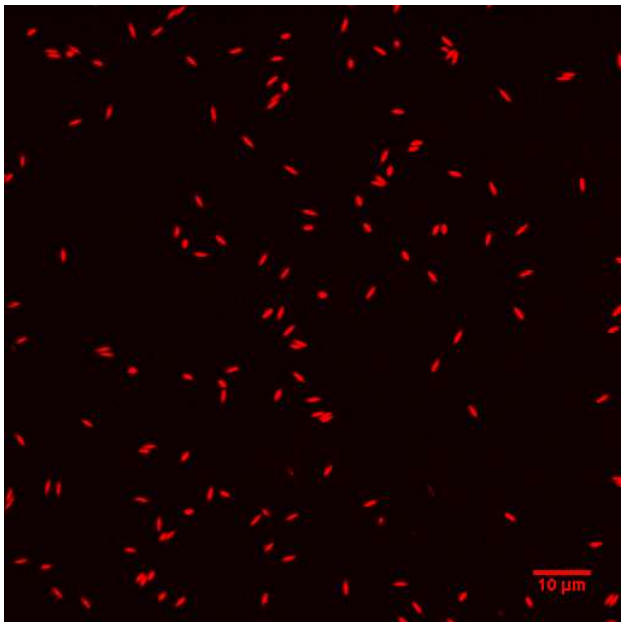

FIGURE 6.1.2.2: Microellipsoids in de-ionized water imaged using confocal microscopy

at the edges to prevent evaporation. All confocal images (figure 6.1.2.2) were captured by using an inverted Nikon A1Rsi equipped with a resonant scanner head operating at 12 kHz. Sample videos were acquired using an air objective (N. A.=1.4, 100x) and a fast ccd camera at a frame rate of ~30.

Video analysis was carried out using home-built Matlab scripts based on differential dynamic algorithm (DDA). The steps involved is DDA are briefly described further. As each sample image in the video represents a spatial light intensity distribution I (x,y,t) at some time t.

A difference image signal ΔI (x,y,Δt) can be calculated by subtracting one image from another for each image pair present in the video. This step gets rid of all intensity signals that are unnecessary for our purpose i.e. static noise contributions and non motile signals coming from particles stuck on microscope slides or dust on optics. In order to get dynamical information in reciprocal space, a fast Fourier transform ΔI (q_x,q_y,Δt) of each difference signal ΔI (x, y,Δt) can be calculated which gives us a Fourier distribution of intensity fluctuations for each difference signal. A statistical averaging of ΔI (q_x,q_y,Δt) over all image pairs provides us a 2D ensemble averaged distribution given by <ΔI (q_x,q_y,Δt) >. Finally, the image structure function D (q_x,q_y,Δt) can be calculated by calculating the 2D power spectra in Fourier space in the form of <|ΔI(q_x,q_y,Δt)|^2>. Therefore, the radially averaged image structure $D(q, \Delta t)$ function[141] is given by:

$$D(q, \Delta t) = < |\Delta I(q, \Delta t)|^2 > \quad 6.1$$

And the wave vector q is calculated by:

$$q = \sqrt{q_x^2 + q_y^2} \quad 6.2$$

This can be used for isotropic images. But it breaks down if there is directionality, such as flow. This whole process is repeated for all possible time steps in the image stack. Finally, the image structure function for processes involving single relaxation with characteristic time τ is fitted to the below equation as:

$$D(q, \Delta t) = A(q)\left[1 - exp\left(\frac{-\Delta t}{\tau(q)}\right)\right] + B(q) \quad 6.3$$

where, $A(q)$ is the convolution of the particles' scattering properties with the optical transfer function of the imaging optics, $B(q)$ is related to the imaging noise and incoherent scattering[138].

For Brownian objects[138], the translational diffusion coefficient D_t and rotational diffusion coefficient D_r of microellipsoids rotating on the surface can be determined by fitting τ vs. q curve obtained through image structure function fits with the following equation:

$$\tau(q) = \frac{1}{D_t q^2 + 2D_r} \tag{6.4}$$

And for a free rod in bulk:

$$\tau(q) = \frac{1}{D_t q^2 + 6D_r} \tag{6.5}$$

We expect such large diffusing rods to have a net translational diffusion coefficient D_t and rotational diffusion coefficient D_R for a free prolate spheroid/rod of aspect ratio r diffusing in an

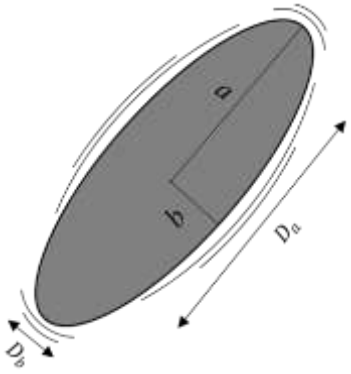

FIGURE 6.1.2.3: For a free prolate spheroid/rod of aspect ratio $r = \frac{a}{b}$ diffusing in an aqueous media of viscosity η, the net translational diffusion coefficient D_t is a combination of translational diffusion coefficient D_a and D_b along major axis a and minor axis b.

aqueous media[187] of viscosity η: (figure 6.1.2.3)

$$D_t = \frac{1}{3}(D_a + 2D_b) \tag{6.6}$$

$$D_a = \frac{k_B T[\ln(2r) - 0.5]}{4\pi\eta a} \tag{6.7}$$

$$D_b = \frac{k_B T[\ln(2r) + 0.5]}{8\pi\eta a} \tag{6.8}$$

$$D_R = \frac{3k_BT[\ln(2r) - 0.5]}{8\pi\eta a^3} \qquad 6.9$$

where, k_B is Boltzmann's constant, $\eta = 0.93$ mPa.s is water's viscosity at temperature T= 23 ^{0}C.

6.1.3 RESULTS AND DISCUSSION:

From the fittings of τ vs. q graphs we determined net translational diffusion coefficient D_t and rotational diffusion coefficient D_R of microellipsoids diffusing freely in bulk (figure 6.1.3.1)

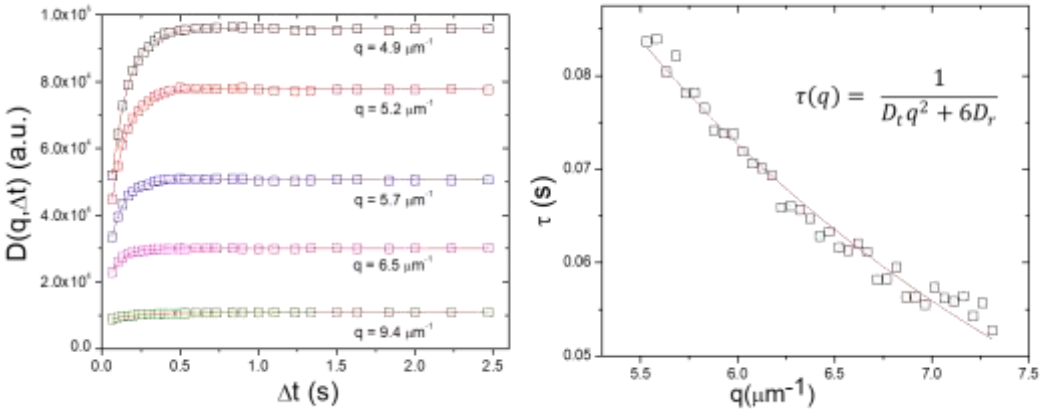

FIGURE 6.1.3.1 Left: Image structure functions vs. time interval at five different values of wave-vectors for the microellipsoids in water solutions diffusing freely in bulk. The solid lines correspond to the fittings of image structure function with Eq. 6.3 assuming a single exponential relaxation. **Right**: Characteristic time scales vs. corresponding q-values are plotted and the fittings with Eq. 6.5 are shown in solid lines.

to be ≈0.341 μm²/s and ≈0.377 μm²/s, respectively. For prolate spheroids diffusing in bulk, microellipsoids in our case, D_t and D_R are expected to be 0.375 μm²/s and 0.408 μm²/s, respectively. These are in accordance with the theoretical predictions for a free rod in bulk. On the other hand, for microellipsoids diffusing in water on the surface (figure 6.1.3.2), the net translational diffusion coefficient and rotational diffusion coefficient are found to be ≈0.022 μm²/s and ≈0.037 μm²/s, respectively. The diffusion values on the surface are significantly lower than in the bulk as expected due to the obstruction in motion from friction on surface.

In conclusion, we report a quick ensemble averaged method DDM that is capable of determining coupled translational and rotational diffusion. For microellipsoids diffusing in deionized water in bulk, there is a good agreement in the measured and expected diffusion

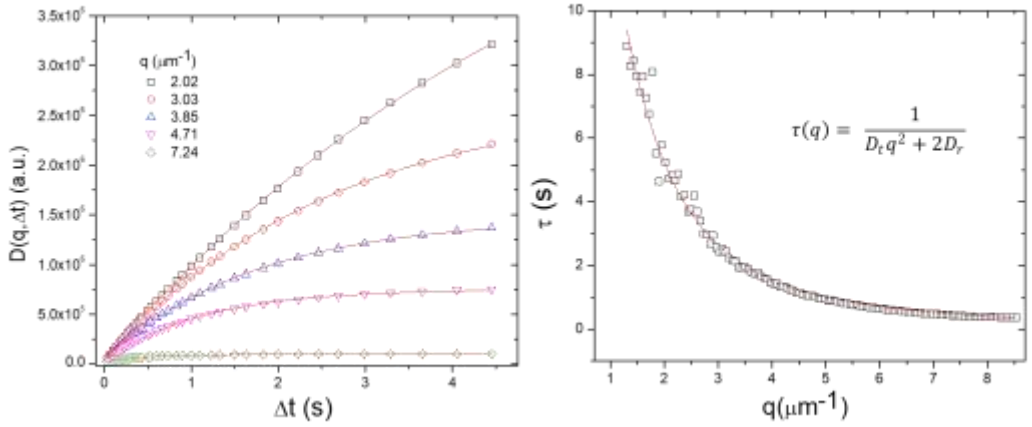

FIGURE 6.1.3.2: Left: Image structure functions vs. time interval at five different values of wave-vectors for the microellipsoids solutions diffusing in deionized water on a 2D surface. The solid lines correspond to the fittings of image structure function with Eq. 6.3 assuming a single exponential relaxation. **Right**: Characteristic time scales vs. corresponding q-values are plotted and the fittings with Eq. 6.4 are shown in solid lines.

coefficients. This makes DDM a promising technique for particles' diffusion characterization in case of anisotropic colloids. This method can be utilized as an efficient way to extract the viscous frictional coefficients experienced by particles due to the 2D confinement as evident from the reduced translation and rotation diffusion values on surface. The results demonstrated that DDM can be extended as a useful method to measure length-scale dependent diffusion of anisotropic particles in aqueous media.

CHAPTER 7

OVERALL CONCLUSION AND FUTURE RESEARCH

This dissertation's main research included nanoparticle diffusion in concentrated solutions of high molecular weight polyethylene glycol, melting in colloidal assembly of discoids on water lutidine droplets and anisotropic diffusion of microellipsoids in aqueous media. After providing a brief introduction and necessary background required for the scope of this study in chapters 1 and 2, main experimental methods i.e. DDM and FCS are briefly explained in chapter 3 followed by important observations and results reported in the chapters 4-6. As mentioned earlier in the thesis, these studies are very important in understanding the transport properties of colloids in complex fluids. Understanding colloidal dynamics within different media is useful in many interdisciplinary fields such as biophysics, chemical engineering as well as in medicine.

In chapter 4, we presented our studies in determining the diffusion of nanoparticles (NPs) within aqueous entangled solutions of polyethylene oxide (PEO). The results are finally compared using two different optical techniques i.e. FCS and DDM. Using FCS, we investigated the dynamics of nanoparticles within polymer solutions by measuring the long-time diffusion coefficient of 25 nm radius particles dispersed in aqueous solutions of high molecular weight, M_w=600 kg/mol PEO. DDM was also used to quantify the wave-vector dependent dynamics of nanoparticles inside the same concentrations of PEO. Our results demonstrate normal diffusion of nanoparticles with good agreement in the diffusion coefficients resulted from both methods. We conclude that DDM can be used to study the dynamics and rheological properties of soft matter at nanoscale. The measured diffusion coefficients are comparable to a scaling theory

indicating the coupling between nanoparticle and polymer dynamics. In future, the focus can be given on situations, where active transport will dominate over the Brownian motion. This situation is important in many situations, including bacterial motion, motor protein transport within crowded cell, delivery of superparamagnetic particles in desired location guided by magnetic field for treatment of diseases, etc. In the case of active transport, $\tau(q) \sim q^{-1}$ instead of $\tau(q) \sim q^{-2}$ as in Brownian motion. As in many cases, Brownian motion will superimpose on pure directional motion, the exponent of $\tau(q)$ will range from 1 to 2. Many nanoparticles, including gold and silica are stabilized through their charge. This gives the opportunity to modulate their motion using electric field. A set up can be designed and built in the future to control the electric field so that we will be able to tune the values of field and observe the changes in particle motion accordingly. The set up will involve an AC/DC power supply, function generator, electrodes, and optical microscope for imaging. The objective will be to track the motion of the particles and thus evaluate the effects of voltage and frequency changes onto their motion. It would be interesting to investigate if any reasonable electric field can control the motion of the particles without electrical breakdown or change of the medium. This strategy then can be used to create ordered structures, which are one of the main requirements for many electronic and medical devices.

We studied reciprocal space dynamics of self-assembled ordered structures made of discoids on the top of dome like surfaces formed by water-lutidine using optical microscopy. We observed characteristic peaks in relaxation time vs. wave vector curves that demonstrate slow dynamics at specific length scales. We get similar peaks in pair correlation curves at matching distances. This is an experimental realization of the de Gennes narrowing phenomenon. We also observed melting of those crystal structures and compared with KTHNY theory of 2D melting.

The results so far are very interesting and indicate that we have observed an intermediate hexatic phase in between crystal and liquid phase. We are currently doing more experiments for observing and studying the phase transitions more closely. In future, we are looking forward to study and understand hexatic to liquid as well as freezing transitions.

Finally, we demonstrated the power of using DDM to be used as a quick and promising technique to calculate ensemble avergared coupled translational and rotational diffusion coefficients of anisotropic particles. In bulk, the calculated diffusion coefficients of microellipsoids are in a good agreement with theoretical prediction of rods. This makes DDM a unique method for studying the dynamical properties of anistropic colloids in aqueous media. We are further interested to look at anisotropic particle diffusion in complex fluids and to study the effect of aspect ratio of anisotropic particles on their translational and rotational diffusion.

We have a few more interesting ongoing research projects that are briefly introduced in the appendixes.

APPENDIX A

CHEMICAL COLLOIDAL SYNTHESIS OF GOLD NANOSPHERES (AuNSs)

Nanoparticle synthesis can be carried out in a number of different ways i.e. colloidal chemical reduction, thermal decomposition, attrition and pulsed laser methods, etc. We have synthesized gold colloidal particles of of size 12 nm and 18 nm using a chemical reduction method. These methods are one of the cheapest and useful way of creating colloidal gold of different sizes. Typically, the gold salt is reduced to metallic gold on adding a reducing agent leaving colloidal gold nanoparticles dispersed in the solution (figure A1). Different sizes of nanoparticles are controlled by initial concentrations of reactants. This method requires further addition of a stabilizing reagent to prevent aggregation. The underlying half reactions of the chemical process are as follows:

$$Au^{3+}(aq) + 3e^- \rightarrow Au$$

$$C_6H_5O_7^{3-} + H_2O(l) \rightarrow C_5H_4O_4^{2-}(aq) + CO_2(g) + H_3O(aq) + 2e^-$$

SYNTHESIS OF GOLD NANOSPHERES (AuNSs) of size 12 nm: (adapted from colloidal chemical method of Frens[188])

Before preparing the solutions, two Erlenmeyer flasks of size 500 ml and 125 ml were washed properly with Aqua regia and finally cleaned with deionized water. First of all, we prepared a solution I by mixing 0.006g of HAuCl4 in 200 ml of de-ionized water in an Erlenmeyer flask of 500 ml size. Another solution II was prepared by mixing 0.014g of sodium citrate in 7 ml of de-ionized water in an Erlenmeyer flask of 125 ml size. The solution I was heated until it started boiling. It took approximately 15 minutes for it to boil. The stirrer was switched on for constant

stirring with the boiling and the solution II was added to the boiling solution I and the solution started changing color to wine-red within 10 minutes. We kept on boiling the solution with constant stirring for next 10 minutes. We controlled the temperature while boiling in a such a way

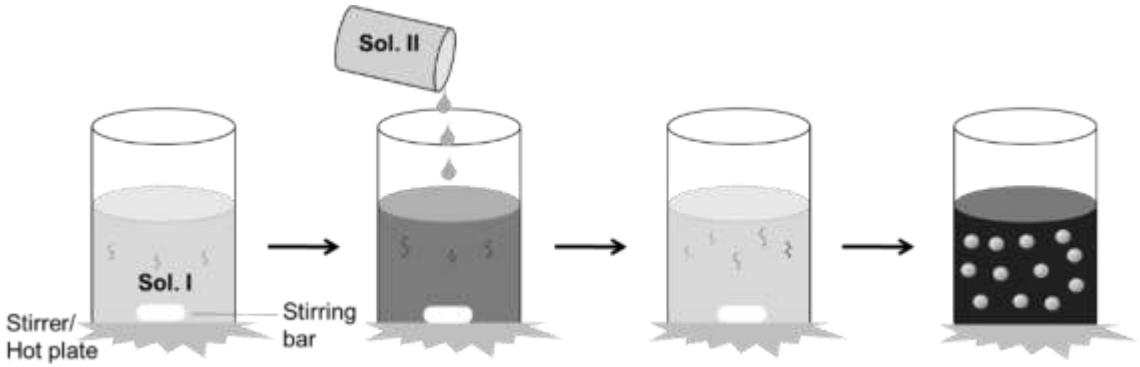

FIGURE A1: Illustration of gold nanoparticle chemical colloidal synthesis process.

that the solution didn't get vaporized. We noticed that the solution changed color from clear to purple first and then it finally changed into wine red. The final solution was kept for cooling for about one and a half hour and when it got cooled, we added 2 mg of sodium citrate (to stabilize the particles) and shook to mix it properly in the solution. After half an hour, one small amount of the final solution was used to find the Diffusion constant using FCS at neutral density filter (NDF) value of 1.04 & 1.2.

SYNTHESIS OF GOLD NANOSPHERES (AuNSs) of size 18 nm: (adapted from colloidal chemical method of Frens[188])

Before preparing the solutions, two Erlenmeyer flasks of size 500 ml and 125 ml were washed properly with NaOH solution and finally cleaned with deionized water. First, we prepared a solution I by mixing 0.008g of HAuCl4 in 250 ml of de-ionized water in an Erlenmeyer flask of 500 ml size. Another solution II was prepared by mixing 0.038g of sodium citrate in 25 ml

of de-ionized water in an Erlenmeyer flask of 125 ml size. The solution I was heated until it started boiling. It took approximately 20-25 minutes for it to boil. The stirrer was switched on for constant stirring with the boiling and the solution II was added to the boiling solution I and the final solution became colorless. We kept on boiling the solution until the color changed from clear to wine red. We controlled the temperature while boiling in such a way that the solution didn't get vaporized. We noticed that the solution changed color from clear to purple first and then it finally changed into wine red. It took about 20 minutes of boiling with vigorous stirring for the solution

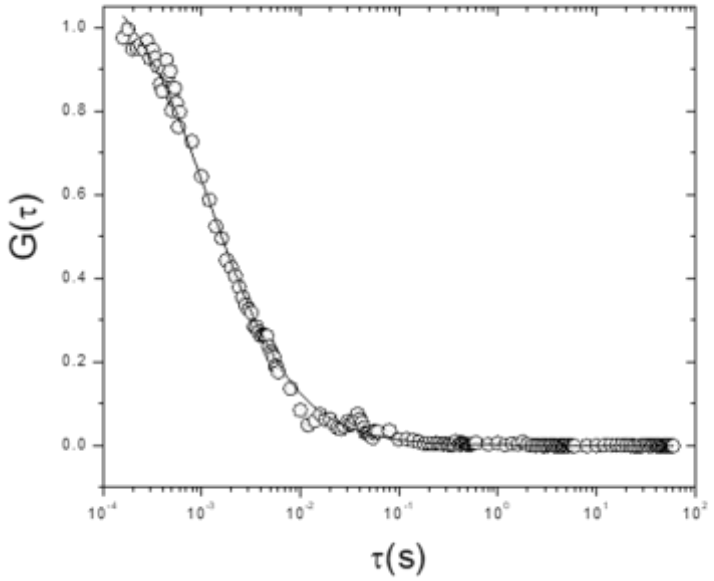

FIGURE A2: Autocorrelation curve for 18nm AuNPs using FCS.

to change color from colorless to wine red. The final solution was kept for cooling for about one and a half hour and when it got cooled, we added 2 mg of sodium citrate (to stabilize the particles) and shook to mix it properly in the solution. After half an hour, one small amount of the final solution was centrifuged for 5 minutes at a medium speed (60). The solution gave some precipitate at the bottom which was thrown away and supernatant was taken out carefully and used to find the diffusion coefficient using FCS at NDF value of 1.04.

One of the intensity correlation graphs that we obtained from FCS is shown in figure A2, with the non- linear fitting that gave a diffusion coefficient D with a value of 24.16 μm²/s. The mean value of D was found to be 24.235 μm²/s with a standard deviation of 1.09 μm²/s. This is in good agreement with Stokes-Einstein equation that D_{SE} = 23.80 μm²/s.

APPENDIX B

EFFECT OF EXTERNAL FLOW ON ROTATIONAL DIFFUSION OF GOLD NANORODS (AuNRs) USING FLUORESCENCE CORRELATION SPECTROSCOPY

Our research group has been working on quantifying the dynamics of nanoparticles inside various soft matter systems by using different optical techniques, most notably, fluorescence correlation spectroscopy (FCS) technique, for quite a long time now. We have been

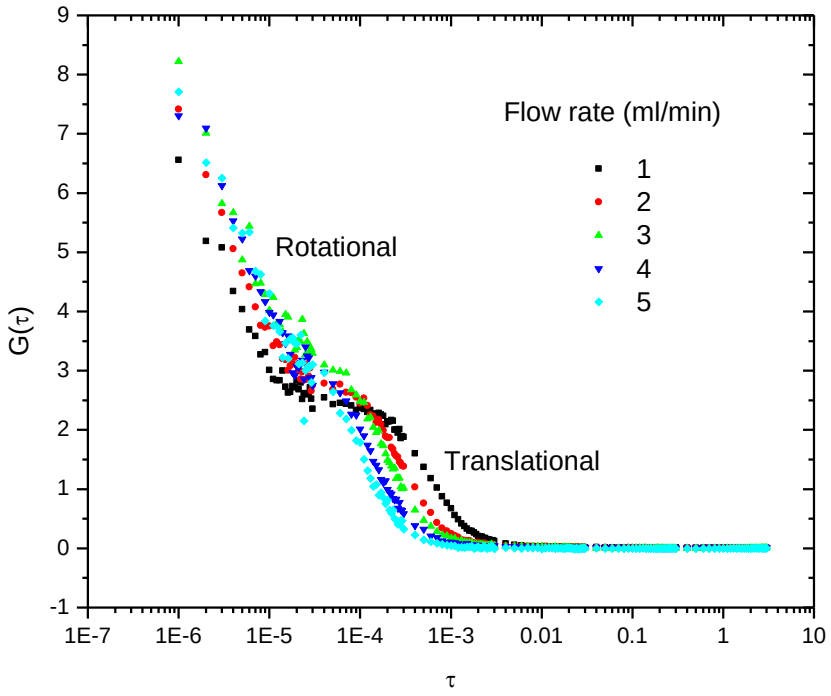

FIGURE B1: Autocorrelation curves illustrating faster rotational diffusion signal and slow translational diffusion signal vs. five flow rates using FCS.

successful in finding how different sized gold nanoparticles (AuNPs) move within synthetic polymer solutions and proteins[71]. We have also studied how shape anisotropy modifies the diffusive behavior by using nanorods[189]. In parallel, new theories have been discovered[190] in this area like statistical dynamical theory, scaling theory, etc. and there are many processes and

mechanism of motions that are still unknown such as hopping motion[191]. These all involves passive motion driven by random thermal energy. The active transport of anisotropic nanoparticles within aqueous media is relatively unexplored.

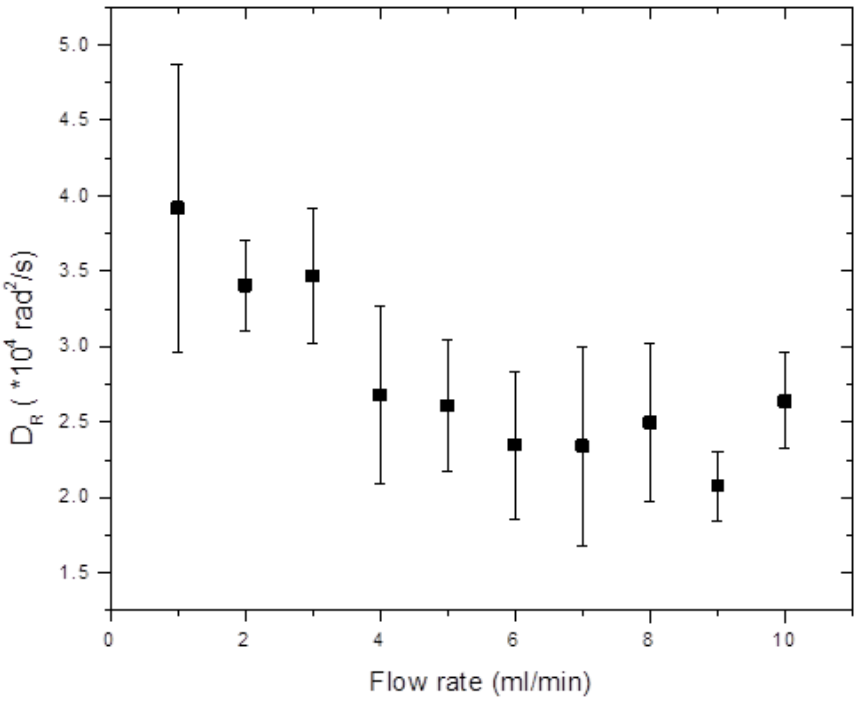

FIGURE B2: Rotational diffusion coefficients calculated from the fittings of autocorrelation curves vs. flow rates using FCS.

The gold nanorods were used as purchased from Sigma-Aldrich, Inc with 17 nm diameter and 60 nm length giving an expect ration of ≈3.5. The aqueous dispersions of gold nanorods in nanomolar concentration were used for rotational diffusion characterization. The rotational dynamics takes place at much smaller time (~ few μs) than translational (~few ms) so both dynamical signals can be separated with little ambiguity in FCS measurements.

For studying the flow effect on rotational diffusion of nanorods, we used a two-photon FCS set up consisting of a Mai Tai, Spectra-Physics Ti:sapphire laser at 800 nm wavelength that pulses at 100 fs at a repetition rate of 80 MHz. In FCS, fluctuations in photon counts are measured

in a very small focal volume ($10^{-15}l$) created by diffraction limit with an air objective (N. A.=0.75, 60X). The emitted photon when the nanorods come across the laser focus are then collected by the same objective and detected by two Hamamatsu single photon sensitive modules i.e. photo multiplier tubes (PMTs). We get the intensity fluctuation autocorrelation curves G(τ) vs. time for different flow rates. The temperature was ≈23^0C and the laser power was kept below 1 mW to prevent heating of the samples during the experiments. A unidirectional flow was introduced in the sample under microscope kept inside a flow cell connected with two syringes, tubes and a Harvard 2000 Phd syringe pump up for refill/infusion. We investiaged the rotational diffusion in the flow range of 1 to 10 ml/min. We extracted the rotational diffusion intensity autocorrelation $G(\tau)$ vs. characteristic time scale τ curves and fitted with the following function:

$$G(\tau) = R * exp(-6D_R\tau)$$

The rotational diffusion coefficients D_R of AuNRs in aqueous media are extracted from the autocorrelation curve fits and plotted vs. flow rate (figure B2). From the investigated flow rates, the results indicate a decrease in the roational diffusion of golf nanorods with increase in the induced flow rates. We have to still do further analysis to validate our results.

APPENDIX C

COLLOIDAL DIFFUSION WITHIN POLYVINYL ALCOHOL(PVA) AND XANTHAN SOLUTIONS USING DIFFERENTIAL DYNAMIC MICROSCOPY

We have also studied the diffusion of nanoparticles in polyvinyl alcohol (PVA) entanged solutions and microparticle diffusion within dilute, semi-dilute and entangled solutions of Xanthan Gum using differential dynamic microscopy (DDM).

We determined that the fluorescent carboxylate spheres of 50 nm size follow normal diffusion within an aqueous PVA (M_W= 89,000 g/mol) solutions with 15 % volume fraction. And

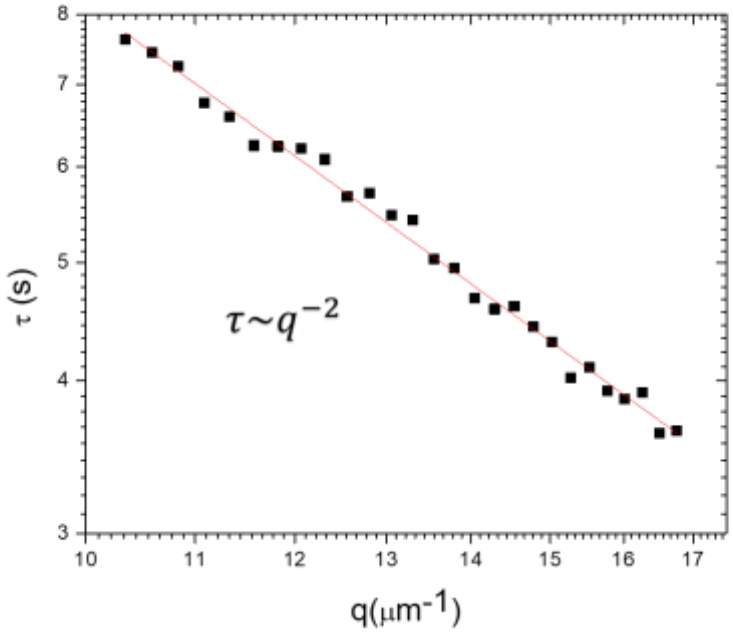

FIGURE C1: Characteristic time vs. wave vector graphs resulted from the fittings of Image Structure Functions demonstrating normal diffusion in 15 % concentration of PVA using DDM.

the q dependence of relaxation time is found as shown in the figure C1 .The measured translational diffusion coefficent D_T has a value of 0.0031 ± 0.008 μm²/s.

DDM was also used to measure the translational diffusion coefficient of micrometer sized silica particles in dilute (10 ppm), semi-dilute (70 ppm) and entangled concentrated regime (600 ppm) of Xanthan (M_W= 200,000 g/mol) solutions. We found that the translational diffusion decreased with increase in xanthan concentration (figure C2). These results are interseting but we still have to validate them with the theories present.

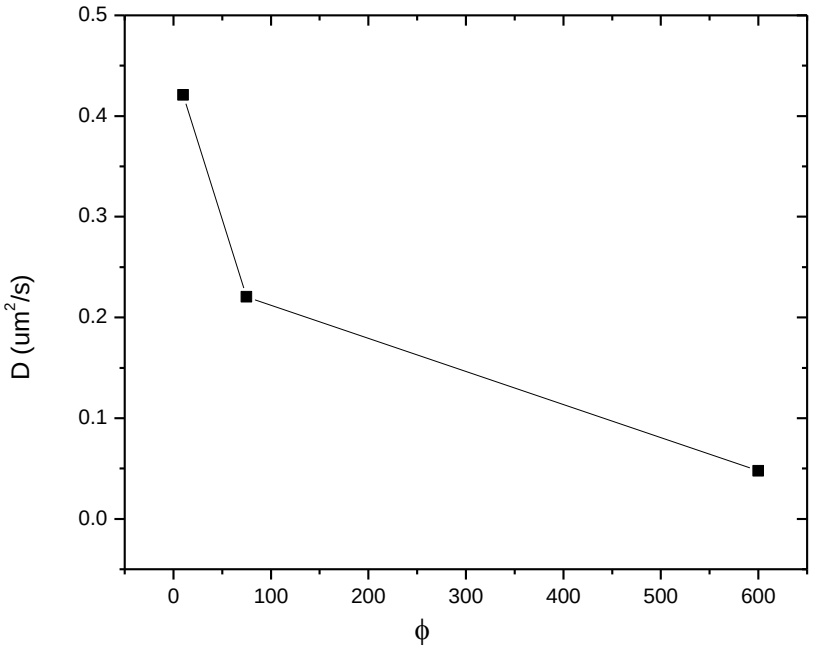

FIGURE C2: Translational diffusion coefficients obtained from the fittings of characteristic time curves vs. wave vector graphs at three xanthan concentrations using DDM.

REFERENCES

1 R. A. Jones, *Soft condensed matter*, Vol. 6 (Oxford University Press, 2002).

2 V. J. Anderson and H. N. Lekkerkerker, Nature **416,** 811 (2002).

3 M. Rubinstein and R. H. Colby, *Polymer Physics* (OUP Oxford, 2003).

4 K. Koynov and H.-J. Butt, Current Opinion in Colloid & Interface Science **17,** 377 (2012).

5 G. D. J. Phillies, Soft matter **11,** 580 (2015).

6 M. Sharma and S. Yashonath, The Journal of Physical Chemistry B **110,** 17207 (2006).

7 J. M. Dealy and R. G. Larson, Hanser, Munich (2006).

8 H. Goldsmith and S. Mason, in *Rheology* (Elsevier, 1967), p. 85.

9 B. Ackerson, P. Pusey, and R. Tough, The Journal of Chemical Physics **76,** 1279 (1982).

10 L. Hong, N. Smolin, and J. C. Smith, Physical review letters **112,** 158102 (2014).

11 A. Dinsmore, M. F. Hsu, M. Nikolaides, M. Marquez, A. Bausch, and D. Weitz, Science **298,** 1006 (2002).

12 D. R. Nelson, *Defects and geometry in condensed matter physics* (Cambridge University Press, 2002).

13 W. T. Irvine, V. Vitelli, and P. M. Chaikin, Nature **468,** 947 (2010).

14 M. Dodgson and M. Moore, Physical Review B **55,** 3816 (1997).

15 M. J. Bowick, A. Cacciuto, D. R. Nelson, and A. Travesset, Physical Review B **73,** 024115 (2006).

16 M. J. Bowick and L. Giomi, Advances in Physics **58,** 449 (2009).

17 M. J. Bowick, D. R. Nelson, and A. Travesset, Physical Review B **62,** 8738 (2000).

[18] F. Ebert, P. Dillmann, G. Maret, and P. Keim, Review of Scientific Instruments **80,** 083902 (2009).

[19] A. Kuijk, D. V. Byelov, A. V. Petukhov, A. van Blaaderen, and A. Imhof, Faraday discussions **159,** 181 (2012).

[20] P. Keim, G. Maret, and H. H. von Grünberg, Physical Review E **75,** 031402 (2007).

[21] R. Bhardwaj, X. Fang, and D. Attinger, New Journal of Physics **11,** 075020 (2009).

[22] D. H. Van Winkle and C. Murray, Physical Review A **34,** 562 (1986).

[23] A. Yethiraj, A. Wouterse, B. Groh, and A. van Blaaderen, Physical review letters **92,** 058301 (2004).

[24] G. N. Sethumadhavan, A. D. Nikolov, and D. T. Wasan, Journal of colloid and interface science **240,** 105 (2001).

[25] Y. Monovoukas and A. P. Gast, Journal of colloid and interface science **128,** 533 (1989).

[26] A. van Blaaderen and P. Wiltzius, Science **270,** 1177 (1995).

[27] R. E. Guerra, C. P. Kelleher, A. D. Hollingsworth, and P. M. Chaikin, Nature **554,** 346 (2018).

[28] B. Li, D. Zhou, and Y. Han, Nature Reviews Materials **1,** 15011 (2016).

[29] Y. Hou, Y. Cheng, T. Hobson, and J. Liu, Nano letters **10,** 2727 (2010).

[30] R. C. Coffin, J. Peet, J. Rogers, and G. C. Bazan, Nature Chemistry **1,** 657 (2009).

[31] V. Chikan and D. Kelley, Nano letters **2,** 141 (2002).

[32] S. Gupta, Q. Zhang, T. Emrick, A. C. Balazs, and T. P. Russell, Nature Materials **5,** 229 (2006).

[33] T. Brunet, J. Leng, and O. Mondain-Monval, Science **342,** 323 (2013).

[34] O. D. Velev and E. W. Kaler, Advanced Materials **12,** 531 (2000).

[35] H. Zhang, X. Yu, and P. V. Braun, Nature nanotechnology **6,** 277 (2011).

[36] O. Velev and E. Kaler, Langmuir **15,** 3693 (1999).

[37] H. Im, K. C. Bantz, S. H. Lee, T. W. Johnson, C. L. Haynes, and S. H. Oh, Advanced Materials **25,** 2678 (2013).

[38] B. Bharti and O. D. Velev, Langmuir **31,** 7897 (2015).

[39] M. J. Solomon, Nature **464,** 496 (2010).

[40] O. Gang and Y. Zhang, Acs Nano **5,** 8459 (2011).

[41] S. Sacanna, L. Rossi, and D. J. Pine, Journal of the American Chemical Society **134,** 6112 (2012).

[42] Y. Kim, A. A. Shah, and M. J. Solomon, Nature communications **5,** 3676 (2014).

[43] U. Tkalec, M. Ravnik, S. Čopar, S. Žumer, and I. Muševič, Science **333,** 62 (2011).

[44] S. K. Smoukov, S. Gangwal, M. Marquez, and O. D. Velev, Soft Matter **5,** 1285 (2009).

[45] T. D. Nguyen, E. Jankowski, and S. C. Glotzer, ACS nano **5,** 8892 (2011).

[46] M. J. Solomon and P. T. Spicer, Soft Matter **6,** 1391 (2010).

[47] R. Picu, Soft Matter **7,** 6768 (2011).

[48] M. J. Solomon and Q. Lu, Current opinion in colloid & interface science **6,** 430 (2001).

[49] J. Liu, Y. Gao, D. Cao, L. Zhang, and Z. Guo, Langmuir **27,** 7926 (2011).

[50] B. Amsden, Macromolecules **32,** 874 (1999).

[51] R. Holyst, A. Bielejewska, J. Szymański, A. Wilk, A. Patkowski, J. Gapiński, A. Żywociński, T. Kalwarczyk, E. Kalwarczyk, and M. Tabaka, Physical Chemistry Chemical Physics **11,** 9025 (2009).

[52] G. D. Phillies, Macromolecules **20,** 558 (1987).

[53] R. Furukawa, J. L. Arauz-Lara, and B. R. Ware, Macromolecules **24,** 599 (1991).

[54] E. D. Von Meerwall, E. J. Amis, and J. D. Ferry, Macromolecules **18,** 260 (1985).

[55] B. Amsden, Polymer **43,** 1623 (2002).

[56] W. Hess, Macromolecules **19,** 1395 (1986).

[57] L.-H. Cai, S. Panyukov, and M. Rubinstein, Macromolecules **44,** 7853 (2011).

[58] R. Cukier, Macromolecules **17,** 252 (1984).

[59] A. R. Altenberger and M. Tirrell, The Journal of chemical physics **80,** 2208 (1984).

[60] A. G. Ogston, B. Preston, and J. Wells, Proceedings of the Royal Society of London. A. Mathematical and Physical Sciences **333,** 297 (1973).

[61] F. B. Wyart and P.-G. de Gennes, The European Physical Journal E **1,** 93 (2000).

[62] G. D. Phillies and D. Clomenil, Macromolecules **26,** 167 (1993).

[63] M. Rubinstein and R. H. Colby, *Polymer physics*, Vol. 23 (Oxford University Press New York, 2003).

[64] J. Liu, D. Cao, and L. Zhang, The journal of physical chemistry C **112,** 6653 (2008).

[65] V. Ganesan, V. Pryamitsyn, M. Surve, and B. Narayanan, (AIP, 2006).

[66] S. W. Hell and J. Wichmann, Optics letters **19,** 780 (1994).

[67] E. Betzig, G. H. Patterson, R. Sougrat, O. W. Lindwasser, S. Olenych, J. S. Bonifacino, M. W. Davidson, J. Lippincott-Schwartz, and H. F. Hess, Science **313,** 1642 (2006).

[68] M. Bierbaum, B. D. Leahy, A. A. Alemi, I. Cohen, and J. P. Sethna, Physical Review X **7,** 041007 (2017).

[69] X. Ye, P. Tong, and L. Fetters, Macromolecules **31,** 5785 (1998).

[70] X. Ye, P. Tong, and L. Fetters, Macromolecules **31,** 6534 (1998).

[71] I. Kohli and A. Mukhopadhyay, Macromolecules **45,** 6143 (2012).

[72] B. J. Alder and T. E. Wainwright, The Journal of chemical physics **27,** 1208 (1957).

[73] P. N. Pusey and W. Van Megen, Nature **320,** 340 (1986).

[74] M. Rutgers, J. Dunsmuir, J.-Z. Xue, W. Russel, and P. Chaikin, Physical Review B **53,** 5043 (1996).

[75] J. Zhu, M. Li, R. Rogers, W. Meyer, R. Ottewill, W. Russel, and P. Chaikin, Nature **387,** 883 (1997).

[76] E. R. Weeks, J. C. Crocker, A. C. Levitt, A. Schofield, and D. A. Weitz, Science **287,** 627 (2000).

[77] E. Zaccarelli, C. Valeriani, E. Sanz, W. Poon, M. Cates, and P. Pusey, Physical review letters **103,** 135704 (2009).

[78] G. L. Hunter and E. R. Weeks, Reports on progress in physics **75,** 066501 (2012).

[79] V. N. Manoharan, Science **349,** 1253751 (2015).

[80] P.-G. De Gennes and J. Prost, *The physics of liquid crystals*, Vol. 83 (Oxford university press, 1995).

[81] K. Zhao and T. G. Mason, Reports on Progress in Physics **81,** 126601 (2018).

[82] P. A. Hiltner and I. M. Krieger, The Journal of Physical Chemistry **73,** 2386 (1969).

[83] H. Lindsay and P. Chaikin, The Journal of Chemical Physics **76,** 3774 (1982).

[84] W. B. Russel, W. Russel, D. A. Saville, and W. R. Schowalter, *Colloidal dispersions* (Cambridge university press, 1991).

[85] L. Blum and A. Torruella, The Journal of Chemical Physics **56,** 303 (1972).

[86] P. V. Konarev, V. V. Volkov, A. V. Sokolova, M. H. Koch, and D. I. Svergun, Journal of applied crystallography **36,** 1277 (2003).

[87] J. Lebowitz, Physical Review **133,** A895 (1964).

[88] J. M. Kosterlitz and D. J. Thouless, Journal of Physics C: Solid State Physics **6,** 1181 (1973).

[89] J. M. Kosterlitz and D. Thouless, Journal of Physics C: Solid State Physics **5,** L124 (1972).

[90] S. Chui, Physical Review B **28,** 178 (1983).

[91] H. Kleinert, Physics Letters A **95,** 381 (1983).

[92] M. A. Glaser and N. A. Clark, Advances in chemical physics **83,** 543 (1992).

[93] Y. Lansac, M. A. Glaser, and N. A. Clark, Physical Review E **73,** 041501 (2006).

[94] K. Chen, T. Kaplan, and M. Mostoller, Physical review letters **74,** 4019 (1995).

[95] F. L. Somer Jr, G. Canright, T. Kaplan, K. Chen, and M. Mostoller, Physical review letters **79,** 3431 (1997).

[96] A. Jaster, Physical Review E **59,** 2594 (1999).

[97] C. Mak, Physical Review E **73,** 065104 (2006).

[98] M. Engel, J. A. Anderson, S. C. Glotzer, M. Isobe, E. P. Bernard, and W. Krauth, Physical Review E **87,** 042134 (2013).

[99] W. Qi, A. P. Gantapara, and M. Dijkstra, Soft Matter **10,** 5449 (2014).

[100] J. Boon and P. Fleury, Adv. Chem Phys. XXIV, Academic Press, New York (1973).

[101] G. L. Squires, *Introduction to the theory of thermal neutron scattering* (Cambridge university press, 2012).

[102] A. Guinier, *X-ray diffraction in crystals, imperfect crystals, and amorphous bodies* (Courier Corporation, 1994).

[103] S. Deutschländer, P. Dillmann, G. Maret, and P. Keim, Proceedings of the National Academy of Sciences **112,** 6925 (2015).

[104] M. W. Kim, A. J. Schwartz, and W. I. Goldburg, Physical Review Letters **41,** 657 (1978).

[105] A. Pal, M. A. Kamal, and V. Raghunathan, Scientific reports **6,** 32313 (2016).

[106] R. Higler, J. Krausser, J. Van Der Gucht, A. Zaccone, and J. Sprakel, Soft matter **14,** 780 (2018).

[107] A. Brodin, A. Nych, U. Ognysta, B. Lev, V. Nazarenko, M. Škarabot, and I. Muševič, Condensed Matter Physics (2010).

[108] Y. Lin, H. Skaff, T. Emrick, A. Dinsmore, and T. P. Russell, Science **299,** 226 (2003).

[109] Y. Lin, A. Böker, H. Skaff, D. Cookson, A. Dinsmore, T. Emrick, and T. P. Russell, Langmuir **21,** 191 (2005).

[110] S. Lin, B. Zheng, and S. Trimper, Physical Review E **73,** 066106 (2006).

[111] L. Ortlieb, S. Rafaï, P. Peyla, C. Wagner, and T. John, Physical review letters **122,** 148101 (2019).

[112] X.-L. Wu and A. Libchaber, Physical review letters **84,** 3017 (2000).

[113] K. C. Leptos, J. S. Guasto, J. P. Gollub, A. I. Pesci, and R. E. Goldstein, Physical Review Letters **103,** 198103 (2009).

[114] Y.-C. Chou and W. I. Goldburg, Physical Review A **20,** 2105 (1979).

[115] Y. Jayalakshmi and E. W. Kaler, Physical review letters **78,** 1379 (1997).

[116] R. Vasanthi, S. Bhattacharyya, and B. Bagchi, The Journal of Chemical Physics **116,** 1092 (2002).

[117] M. M. Tirado and J. G. de la Torre, The Journal of chemical physics **71,** 2581 (1979).

[118] M. M. Tirado, C. L. Martínez, and J. G. de la Torre, The Journal of chemical physics **81,** 2047 (1984).

[119] J. G. De La Torre and M. C. L. Martinez, Biopolymers **23,** 611 (1984).

[120] S. Broersma, The Journal of Chemical Physics **32,** 1632 (1960).

[121] S. Broersma, The Journal of Chemical Physics **32,** 1626 (1960).

[122] Y. Han, A. Alsayed, M. Nobili, and A. G. Yodh, Physical Review E **80,** 011403 (2009).

[123] R. Cush, P. S. Russo, Z. Kucukyavuz, Z. Bu, D. Neau, D. Shih, S. Kucukyavuz, and H. Ricks, Macromolecules **30,** 4920 (1997).

[124] R. Cush, D. Dorman, and P. S. Russo, Macromolecules **37,** 9577 (2004).

[125] S. Alam and A. Mukhopadhyay, Macromolecules **47,** 6919 (2014).

[126] J. M. Tsay, S. Doose, and S. Weiss, Journal of the American Chemical Society **128,** 1639 (2006).

[127] F. Croccolo, D. Brogioli, A. Vailati, M. Giglio, and D. S. Cannell, Applied Optics **45,** 2166 (2006).

[128] D. Magde, E. Elson, and W. W. Webb, Physical Review Letters **29,** 705 (1972).

[129] R. Poling-Skutvik, R. Krishnamoorti, and J. C. Conrad, ACS Macro Letters **4,** 1169 (2015).

[130] R. Rigler, Ü. Mets, J. Widengren, and P. Kask, European Biophysics Journal **22,** 169 (1993).

[131] P. S. Dittrich and P. Schwille, Analytical chemistry **74,** 4472 (2002).

[132] U. Kettling, A. Koltermann, P. Schwille, and M. Eigen, Proceedings of the National Academy of Sciences **95,** 1416 (1998).

[133] O. Krichevsky and G. Bonnet, Reports on Progress in Physics **65,** 251 (2002).

[134] K. M. Berland, P. So, and E. Gratton, Biophysical Journal **68,** 694 (1995).

[135] E. Haustein and P. Schwille, Annu. Rev. Biophys. Biomol. Struct. **36,** 151 (2007).

[136] W. Denk, J. H. Strickler, and W. W. Webb, Science **248,** 73 (1990).

[137] J. Ries and P. Schwille, BioEssays **34,** 361 (2012).

[138] R. Cerbino and V. Trappe, Phys. Rev. Lett. **100,** 188102 (2008).

[139] F. Croccolo and D. Brogioli, Applied optics **50,** 3419 (2011).

[140] M. Pluta, *Advanced light microscopy. Vol. 1. Principles and basic properties* (Amsterdam.: Elsevier, 1988).

[141] R. Cerbino and V. Trappe, Physical Review Letters **100,** 188102 (2008).

[142] N. Shokeen, C. Issa, and A. Mukhopadhyay, Appl. Phys. Lett. **111,** 263703 (2017).

[143] D. Schaeffel, S. Yordanov, R. H. Staff, A. Kreyes, Y. Zhao, M. Schmidt, K. Landfester, J. Hofkens, H.-J. r. Butt, and D. Crespy, ACS Macro Letter **4,** 171 (2015).

[144] J. Zhao and S. Granick, J. Am. Chem. Soc. **126,** 6242 (2004).

[145] I. Kohli, S. Alam, B. Patel, and A. Mukhopadhyay, Appl. Phys. Lett. **102,** 203705 (2013).

[146] R. F. Heuff, D. T. Cramb, and M. Marrocco, Chem. Phys. Lett **454,** 257 (2008).

[147] C. A. Grabowski, B. Adhikary, and A. Mukhopadhyay, Appl. Phys. Lett. **94,** 021903 (2009).

[148] P. S. Dittrich and P. Schwille, Anal. Chem. **74,** 4472 (2002).

[149] S. Alam and A. Mukhopadhyay, J. Phys. Chem. C **118,** 27459 (2014).

[150] J. Yamamoto, M. Oura, T. Yamashita, S. Miki, T. Jin, T. Haraguchi, Y. Hiraoka, H. Terai, and M. Kinjo, Opt. Express **23,** 32633 (2015).

[151] D. Lumma, S. Keller, T. Vilgis, and J. O. Rädler, Phys. Rev. Lett. **90,** 218301 (2003).

[152] F. Giavazzi and R. Cerbino, J. Opt. **16,** 083001 (2014).

[153] F. Giavazzi, D. Brogioli, V. Trappe, T. Bellini, and R. Cerbino, Phys Rev E **80,** 031403 (2009).

[154] F. Ferri, A. D'Angelo, M. Lee, A. Lotti, M. Pigazzini, K. Singh, and R. Cerbino, Eur. Phys. J. **199,** 139 (2011).

[155] L. G. Wilson, V. A. Martinez, J. Schwarz-Linek, J. Tailleur, G. Bryant, P. Pusey, and W. C. Poon, Phys. Rev. Lett. **106,** 018101 (2011).

[156] V. A. Martinez, R. Besseling, O. A. Croze, J. Tailleur, M. Reufer, J. Schwarz-Linek, L. G. Wilson, M. A. Bees, and W. C. Poon, Biophys. J. **103,** 1637 (2012).

[157] R. Cerbino and A. Vailati, Curr. Opin. Colloid Interface Sci. **14,** 416 (2009).

[158] A. V. Bayles, T. M. Squires, and M. E. Helgeson, Soft matter **12,** 2440 (2016).

[159] R. Wang, L. Lei, Y. Wang, A. J. Levine, and G. Popescu, Phys. Rev. Lett. **109,** 188104 (2012).

[160] M. Reufer, V. A. Martinez, P. Schurtenberger, and W. C. Poon, Langmuir **28,** 4618 (2012).

[161] K. He, F. Babaye Khorasani, S. T. Retterer, D. K. Thomas, J. C. Conrad, and R. Krishnamoorti, ACS Nano **7,** 5122 (2013).

[162] J. D. C. Jacob, K. He, S. T. Retterer, R. Krishnamoorti, and J. C. Conrad, Soft Matter **11,** 7515 (2015).

[163] P. J. Lu, F. Giavazzi, T. E. Angelini, E. Zaccarelli, F. Jargstorff, A. B. Schofield, J. N. Wilking, M. B. Romanowsky, D. A. Weitz, and R. Cerbino, Phys. Rev. Lett. **108,** 218103 (2012).

[164] R. A. Omari, A. M. Aneese, C. A. Grabowski, and A. Mukhopadhyay, J. Phys. Chem. B **113,** 8449 (2009).

[165] A. Bausch, M. J. Bowick, A. Cacciuto, A. Dinsmore, M. Hsu, D. Nelson, M. Nikolaides, A. Travesset, and D. Weitz, Science **299,** 1716 (2003).

[166] E. J. Kramer, Nature **437,** 824 (2005).

[167] M. Park, C. Harrison, P. M. Chaikin, R. A. Register, and D. H. Adamson, Science **276,** 1401 (1997).

[168] S. Schneider and G. Gompper, EPL (Europhysics Letters) **70,** 136 (2005).

[169] Y. Chushak and A. Travesset, EPL (Europhysics Letters) **72,** 767 (2005).

[170] A. Pérez-Garrido, M. Dodgson, and M. Moore, Physical Review B **56,** 3640 (1997).

[171] R. Ben, G. Ashman, C. Bernardini, L. Bonolis, D. Bernoulli, S. Brandt, T. Brown, T. Browne, F. Cornford, and S. S. Eddington, in *The Big Ideas in Physics and How to Teach Them: Teaching Physics 11–18*; *Vol. 3* (Taylor & Francis India, 2018), p. x.

[172] V. Vitelli, J. B. Lucks, and D. R. Nelson, Proceedings of the National Academy of Sciences **103,** 12323 (2006).

[173] B. Halperin and D. R. Nelson, Physical Review Letters **41,** 121 (1978).

[174] K. Zahn, R. Lenke, and G. Maret, Physical review letters **82,** 2721 (1999).

[175] C. Grimes and G. Adams, Physical Review Letters **42,** 795 (1979).

[176] P. J. Lu, F. Giavazzi, T. E. Angelini, E. Zaccarelli, F. Jargstorff, A. B. Schofield, J. N. Wilking, M. B. Romanowsky, D. A. Weitz, and R. Cerbino, Physical review letters **108,** 218103 (2012).

[177] I. Buttinoni, J. Bialké, F. Kümmel, H. Löwen, C. Bechinger, and T. Speck, Physical review letters **110,** 238301 (2013).

[178] F. Giavazzi, A. Fornasieri, A. Vailati, and R. Cerbino, The European Physical Journal E **39,** 103 (2016).

[179] F. Giavazzi, G. Savorana, A. Vailati, and R. Cerbino, Soft Matter **12,** 6588 (2016).

[180] C. Ho, A. Keller, J. Odell, and R. Ottewill, Colloid and Polymer Science **271,** 469 (1993).

[181] N. A. Frey, S. Peng, K. Cheng, and S. Sun, Chemical Society Reviews **38,** 2532 (2009).

[182] D. A. Giljohann, D. S. Seferos, W. L. Daniel, M. D. Massich, P. C. Patel, and C. A. Mirkin, Angewandte Chemie International Edition **49,** 3280 (2010).

[183] L. Xiao, Y. Qiao, Y. He, and E. S. Yeung, Journal of the American Chemical Society **133,** 10638 (2011).

[184] F. C. Cheong and D. G. Grier, Optics express **18,** 6555 (2010).

[185] A. Loman, I. Gregor, C. Stutz, M. Mund, and J. Enderlein, Photochemical & photobiological sciences **9,** 627 (2010).

[186] N. Shokeen, C. Issa, and A. Mukhopadhyay, Applied Physics Letters **111,** 263703 (2017).

[187] M. Doi and S. Edwards, The Theory of Polymer Dynamics**,** 218.

[188] G. Frens, Nature physical science **241,** 20 (1973).

[189] S. Alam and A. Mukhopadhyay, The Journal of Physical Chemistry C **118,** 27459 (2014).

[190] A. V. Dobrynin and M. Rubinstein, Progress in Polymer Science **30,** 1049 (2005).

[191] L.-H. Cai, S. Panyukov, and M. Rubinstein, Macromolecules **48,** 847 (2015).

ABSTRACT

COLLOIDAL DYNAMICS WITHIN POLYMER SOLUTIONS AND COMPLEX FLUIDS

by

NAMITA SHOKEEN

August 2019

Advisor: Dr. Ashis Mukhopadhyay

Major: Physics

Degree: Doctor of Philosophy

Soft matter is a subfield of condensed matter physics that includes the study of colloidal dynamics. This is important in multidisciplinary fields for technological and medical advancements. My research focused on quantifying the dynamics of nano and micron-sized particles within various media using two-photon fluorescence correlation spectroscopy (FCS) and differential dynamic microscopy (DDM). FCS is a single photon sensitive technique that detects spontaneous fluctuations in fluorescence during dynamical processes over time while DDM used optical microscopy to analyze the colloidal motion in Fourier space. The diffusion coefficient (D) of 25 nm radii particles within aqueous entangled solutions of polyethylene oxide (PEO; M_w=600 kg/mol) demonstrated normal diffusion with almost identical values using DDM and FCS and followed a scaling theory. We observed characteristic peaks in relaxation time $\tau(q)$ of microdiscoids dispersed in aqueous water lutidine solutions that indicate slow relaxations in certain structural rearrangements explained with de Gennes narrowing phenomenon. Melting of the crystal structures formed by microdiscoids on top of droplets is comparable to a 2D melting

theory. In case of microellipsoids (aspect ratio ≈2.8), DDM is proven to be a quick and powerful method to determine the translational and rotational diffusion coefficients.

AUTOBIOGRAPHICAL STATEMENT

NAMITA SHOKEEN

EDUCATION:

- 2014-2019, Wayne State University, Detroit, MI: Ph.D. Physics
- 2014-2017, Wayne State University, Detroit, MI: M.S. Physics
- 2011-2013, Indian Institute of Technology Guwahati, Assam, India: M.Sc. Physics
- 2008-2011, University of Delhi, Miranda House, Delhi, India: B. Sc. Physics

PUBLICATIONS AND PRESENTATIONS:

1. Namita Shokeen, Christopher Issa and Ashis Mukhopadhyay "Comparison of Nanoparticle Diffusion using Fluorescence Correlation Spectroscopy and Differential Dynamic Microscopy within Concentrated Polymer Solutions", Applied Physics Letters, 111 (26), 263703 (2017).
2. Kavindya Senanayake, Namita Shokeen, Ehsan Fakhrabadi, Matthew Liberatore and Ashis Mukhopadhyay "Diffusion of Nanoparticle within a Semidilute Polyelectrolyte Solution", submitted to Soft Matter, ID: SM-ART-07-2019-001313 (2019).
3. Namita Shokeen and Ashis Mukhopadhyay " A quick method to determine ensemble avergaed Translational and Rotational Diffusion coefficients" 2019 American Physical Society (APS) Annual Meeting, Boston, New York (USA).
4. Namita Shokeen and Ashis Mukhopadhyay " Dynamics of nano and microparticles in aqueous media", 2018 Condensed Matter and Biophysics Seminar, Wayne State University, Detroit, Michigan (USA).